ABSTRACT

Title of Dissertation:	EVALUATION AND IMPROVEMENT OF MECHANICAL AND CHEMICAL RESILIENCE OF INTERMEDIATE-TEMPERATURE SOLID OXIDE FUEL CELL ANODES
	Thomas Harrison Hays, Doctor of Philosophy, Materials Science and Engineering, 2017
Dissertation directed by:	Professor Eric D. Wachsman, Materials Science and Engineering

Solid oxide fuel cells are in the process of reaching maturity as an energy generation technology, but a number of technical challenges exist, namely mechanical and chemical resilience, that hinder the realization of their full potential and widespread deployment. As more research and development work has been performed on intermediate temperature SOFCs based on gadolinium doped ceria, there persists a number of gaps in the understanding of the behavior of these devices. The mechanical properties of component material and SOFC structures in non-ambient conditions, the nature and degree of damage caused by sulfurized hydrocarbon fuels, and the potential for leveraging produced thermal energy are not satisfactorily characterized for GDC-based SOFCs. Mechanical testing of porous GDC and anode supported SOFC coupons from room temperature to 650°C was performed in air and reducing conditions using a test system designed and built for this application. Spherical

porosity was determined to result in the higher strength compared to other pore geometries and a positive linear dependence between temperature and strength was determined for SOFC coupons. Additionally, placing the electrolyte layer in compressive stress resulted in higher strengths. Standard SOFCs were operated while exposed to hydrogen and methane containing ppm level hydrogen sulfide concentration. An infiltration technique was used to deposit a fine layer of GDC on the inner surfaces of some cell anodes, and the results of sulfur expose was compared between infiltrated and unmodified cells. GDC infiltration allowed cells to operate stably for hundreds of hours on sulfurized fuel while unmodified cells were fatally damaged in less than two days. A primary and a resulting secondary degradation mechanism were identified and associated with sulfur and carbon respectively through surface analysis. A novel technique for measuring thermal power output of small-scale SOFCs operating on a variety of fuels was developed and used to evaluate electrical and thermal outputs while operating on simulated anaerobic digester biogas. These findings were used to propose a multi-utility generation system centered on a nominal 10 kW SOFC unit fed by anaerobic digesters and capable of producing clean water and electricity for 50 individuals through direct contact membrane distillation driven by captured waste heat from the SOFC.

EVALUATION AND IMPROVEMENT OF MECHANICAL AND CHEMICAL RESILIENCE OF INTERMEDIATE-TEMPERATURE SOLID OXIDE FUEL CELL ANODES

by

Thomas Harrison Hays

Dissertation submitted to the Faculty of the Graduate School of the
University of Maryland, College Park, in partial fulfillment
of the requirements for the degree of
Doctor of Philosophy
2017

Advisory Committee:
Professor Eric D. Wachsman, Chair
Professor Sreeramamurthy Ankem
Associate Professor Liangbing Hu
Associate Professor Dongxia Liu
Professor Chunsheng Wang

Preface

This dissertation, “Evaluation and Improvement of Mechanical and Chemical Resilience of Intermediate-Temperature Solid Oxide Fuel Cell Anodes”, is based upon three avenues of inquiry to better understand and/or improve the function of ceria-based solid oxide fuel cell anodes. It has been written to fulfill the graduation requirement of the Ph.D. Program in the Materials Science and Engineering Department of the A. James Clark School of Engineering at the University of Maryland. The research and writing of this dissertation began in November, 2012 and lasted through October, 2017.

The various research projects reported on in this work were undertaken using grants from a number of funding sources. These include the National Energy Transportation Laboratory, ARPA-E, The Electrochemical Society, and the Maryland Industrial Partnerships Program with Redox Power Systems as a partner.

I hope this work will serve as a step toward further research and development of solid oxide fuel cell technology and that it is a useful addition to field.

Thomas Hays

College Park, Maryland, September 25, 2017

Dedication

For my mother and father, Susan and Bruce, from whom I learned the value of education and the drive to pursue it.

Acknowledgements

I would like to first thank my advisor Dr. Eric D. Wachsman for his mentorship and the opportunity to pursue my doctoral work in his research group. His guidance and support was key to my completion of this degree.

I would also like to thank the members of the Wachsman research group, past and present, for all of the samples, tests, measurements, paper revisions, presentation practice sessions, late nights, and early mornings that were part of my experience these past five years. In particular, Patrick Stanley, A. Mohammed Hussain, Ian Robinson, Yi-Lin Huang, Greg Hitz, Dennis McOwen, Adam Jolley, Chris Pelligrinelli, Ashley Ruth, and Colin Gore. Each of you helped to make some part of this work possible.

Finally, I would like to express my deep gratitude to my fiancée Veronica for her incredible support and patience during my graduate studies and especially during the writing of this dissertation. I could not have reached this point without her. Thank you.

Thomas Hays

Table of Contents

List of Tables

List of Figures

List of Abbreviations

SOFC: Solid oxide fuel cell

TPB: Triple phase boundary

YSZ: Yttrium stabilized zirconia

LSM: Lanthanum-strontium manganese oxide

GDC: Gadolinium doped ceria

LSCF: Lanthanum strontium cobalt ferrite oxide

EIS: Electrochemical impedance spectroscopy

ASL: Anode support layer

AFL: Anode functional layer

OCV: Open circuit voltage

ASR: Area specific resistance

I-V: current-voltage

PMMA: Polymethyl methacrylate

SEM: Scanning electron microscopy

EDS: Energy-dispersive X-ray spectroscopy

TEM: Transmission electron microscopy

XPS: X-ray photoelectron spectroscopy

UTM: Universal testing machine

ADG: Anaerobic digestion

DCMD: Direct contact membrane distillation

Chapter 1: Introduction

The invention of the first widely practical steam engines by James Watt in 1781 marked the beginning of the industrial revolution and the transition from human and animal power to mechanical and eventually electrical power as the predominant method of operating technology. Incredible engineering and scientific advances have been made in the two hundred and thirty odd years since Watt received his patent, but in many respects we have yet to graduate from being a steam-driven civilization. Carnot cycle heat engines supplied by the burning of coal, oil, or natural gas still dominate the electricity generation sector, and even nuclear power is reliant on how efficiently we can design steam turbines to capture heat energy. This process is a legacy of the time before electricity became the dominant energy carrier. The electrical dynamo was developed to be compatible with existing mechanical technology, but it is a roundabout method of generating electricity from fuels.

Ultimately, a truly sustainable source of electricity generation must be developed to stave off serious changes to the climate and to prevent conflict over dwindling energy resources. Solar, wind, and wave energy are the likely candidates for this sustainable future. In the past decade, these “alternative” energy sources have begun to reach economic parity with traditional fossil fuels, and in some specific regions, surpassed them. This transition will likely happen, but given vested political interests and the highly developed industries of fossil fuel production and use, it may take a long time.

In the short term, efforts should be made to optimize electricity generation from fossil fuels as much as possible. By increasing efficiency of generation processes and developing new and improved techniques and devices, the transition to fully sustainable electricity production will be eased.

An examination of the major steps in the process of burning fossil fuels to generate electricity shows immediate potential for significant improvements in efficiency. First, the chemical energy stored in the atomic bonds of molecules is released through the combustion reaction. This is the conversion of chemical energy to heat energy. This heat is then transferred to water to generate steam through the liquid-vapor phase change. The expansion of the steam drives a turbine and thus heat energy becomes mechanical motion. Finally, the spinning turbine drives a dynamo which uses a magnet spinning inside a nest of conductive wire. The rotating magnetic field induces an electrical current in the wire, completing the energy conversion path.

In total, there are four steps between the stored chemical energy in the fuel and the resulting electricity that is generated. In each of these steps, there are unrecoverable losses of energy that contribute to fairly poor overall process efficiency. A more succinct view of this issue is that the process of using heat energy to generate work is limited by Carnot efficiency in addition to some amount of lost heat and frictional losses in any moving parts. Due to these losses and limits, it is very attractive to move out of the heat engine paradigm, toward a more direct path of electricity generation.

All chemical reactions occur through the interaction of the electrons of atoms. Barring the noble gasses, every element will give, take, or share electrons with other elements and form molecules as long as conditions are right. One of the simplest reactions is the oxidation of hydrogen, where diatomic H_2 breaks apart and bonds with an oxygen ion (O^{2-}) to form water, or H_2O. In this reaction, two electrons are exchanged, and all the atoms reach a neutral charge. This reaction is exothermic, so heat is released to the surroundings when the reaction occurs. To generate electricity, the heat from the reaction could be used to drive a heat engine with all the efficiency losses inherent to the process. However, if the two electrons that are exchanged during the reaction could be harnessed, many of the limitations of the heat engine are bypassed.

Solid oxide fuel cells (SOFC) operate on this basic principle of capturing electrons exchanged during a chemical reaction. Fundamentally, an oxygen ion is transported across a solid, electronically insulating layer so that it may react with other atoms or molecules. To enable this action, fuel cells are often composed of layers of different and multifunctioning materials. Therefore, very in-depth materials development and engineering is involved in the creation of these devices.

Ionic conduction is the core phenomenon that allows these devices to function. Significant solid state ionic conductivity was well established scientifically by the 1930s but only in recent decades have materials been developed that allow practical use on ionic conductors for power generation[1]. Yttrium stabilized zirconia was the first practical oxygen ion conductor developed that was suitable for the creation of a

SOFC[1]. This material and variants have been the center of SOFC research and development for many years, but the high temperature necessary for good conductivity has limited its practical application[2], [3]. For this reason, other ion conducting materials have received research attention, resulting in a number of alternative SOFC chemistries[4]–[6]. In addition, variations in the physical design and construction of cells, particularly planar configurations, have improved device performance considerably[3]. By building on recent advancements in material properties and device design, there is great potential for SOFCs to be a key technology in the energy sector and as a gateway to a fully diversified renewable energy future.

The goal of this work is to accurately characterize and improve the resilience, both mechanical and chemical, of gadolinium doped ceria based SOFCs with an emphasis on moving the technology toward widespread use. In particular, challenges from sulfur contamination of cell anodes and cracking caused by sealing stress are addressed. Additionally, the suitability of SOFCs as a technology for providing basic utilities, electricity and clean water, on the local community level is explored.

Chapter 2: Solid Oxide Fuel Cells

2.1. Operating Principles

Solid oxide fuel cells are distinguished by the use of a ceramic electrolyte layer and the conduction of oxygen ions as the internal charge carrier of the device. SOFCs, like all fuel cells, consist of three primary components: a cathode, an electrolyte, and an anode. In the case of SOFCs, the cathode serves to promote oxygen reduction (Equation 1) and incorporation of oxygen ions into an oxygen conducting ceramic material.

$$\mathbf{O_2 + 2e^- \rightarrow 2O^{2-}} \qquad \mathbf{(1)}$$

This oxygen conducting material forms the electrolyte layer of the cell and facilitates transport of the oxygen ions to the anode side of the cell. Once oxygen ions reach the anode, they react with the fuel species and electrons are sent through external circuit (Figure 1).

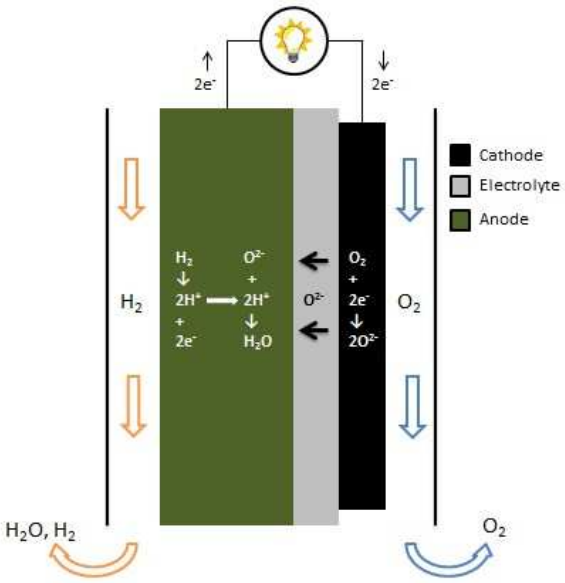

Figure 1: SOFC concept schematic with reaction

A key feature of the anode and cathode is the Triple Phase Boundary (TPB) (Figure 2). The TPB is the one dimensional interface between the ion conducting ceramic, the electronic conducting, typically metallic catalyst, and the gas present in the electrode pores. The electrochemical reaction cannot proceed without all three of these phases present. Because of the positive correlation between TPB length and activity in the electrodes, these layers are usually fine-grained composites of ceramic and catalyst

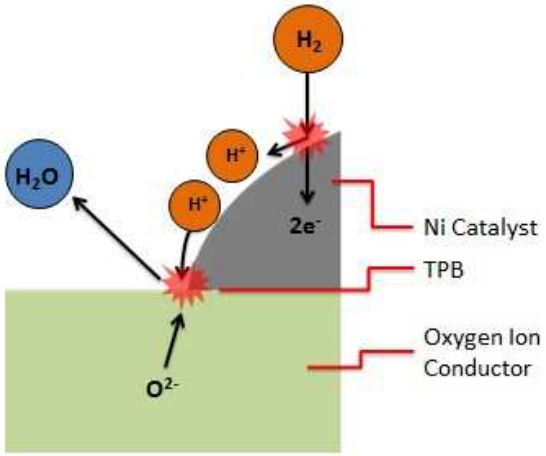

Figure 2: Anode triple phase boundary reactions

The work that can be performed by a SOFC is limited by the change in the Gibbs free energy of the electrochemical reaction that occurs at the cell. This is affected by both the cell temperature and the pressure of the gasses at the cell.

$$\boldsymbol{W = \Delta G = -nFE} \qquad \textbf{(2)}$$

Equation 1 relates the free energy to the ideal cell potential, E. n represents the number of electrons in the electrochemical reaction and F is Faraday's constant. The change in free energy can also be expressed as:

$$\boldsymbol{\Delta G = \Delta G^0 + RT\ ln\frac{f_C^c f_D^\delta}{f_A^\alpha f_B^\beta}} \qquad \textbf{(3)}$$

Where f_A is the fugacity of reactant A. Using Equation 2 and Equation 3 leads to the general form of the Nernst equation[7]–[9].

$$\boldsymbol{E = E^0 + \frac{RT}{nF}\ ln\frac{f_C^c f_D^\delta}{f_A^\alpha f_B^\beta}} \qquad \textbf{(4)}$$

This equation yields the Nernst potential which is the maximum open circuit potential the cell can have. This maximum potential is used in calculating the cell efficiency. Efficiency is the ratio of useful energy to total energy. It has been calculated that an ideal fuel cell operating under ideal condition can have a maximum thermal efficiency of 0.83[7]. The standard method for expressing cell efficiency is:

$$\eta = \frac{(0.83)\times V_{actual}}{E_{ideal}} \quad (5)$$

This definition assumes complete utilization of fuel which will not occur in reality. Therefore, this efficiency must be multiplied by the fuel utilization fraction[7].

The Nernst potential of a SOFC is driven by the difference in oxygen partial pressure (p_{O2}) between the two sides of the electrolyte. For the cell to function, preserving this chemical gradient is essential and any pathway for oxygen that is not ionic conduction through the electrolyte is in effect a chemical short circuit that will harm the device's function.

2.2. Device Chemistries

2.2.1. Yttrium Stabilized Zirconia

The inclusion of elements with a different valence state to zirconium oxide was found to increase the oxygen vacancy concentration in the zirconia crystal[Wagner, 1943]. As oxygen vacancies are the pathway for ionic transport in oxides, doping with an appropriate element can greatly improve the ionic conductivity in zirconia. In

addition to conductivity improvement, the addition of elements that form cubic structure oxides helps to stabilize the zirconia crystal structure at high temperatures. This is key for device applications due to the significant volume change that accompanies the monoclinic-tetragonal phase change of pure zirconia in the 1000°C regime[8]. Sufficient addition of yttrium cations causes and preserves a stable cubic phase at these temperatures and prevents strain related mechanical failure.

Yttrium stabilized zirconia (YSZ) based SOFCs are conventionally electrolyte supported with relatively thin electrode layers. Nickel is the most commonly used anode catalyst, in the form of nickel-YSZ cermet. Perovskite lanthanum manganese oxide doped with strontium (LSM) serves as the cathode material due to its good ability to catalyze the oxygen reduction reaction[7]. YSZ must be above 800°C for sufficiently high ionic conductivity to be useful in a fuel cell[10], [11]. The high temperatures required for these devices to operate can make system design difficult as few engineering materials have desirable properties under these conditions. A large amount of insulation is also needed to maintain operating temperature. YSZ is quite mechanically strong however, and is easy to synthesize and process[10].

2.2.2. Gadolinium Doped Ceria

Cerium oxide possesses a fluorite structure similar to that of zirconia. Trivalent dopants, when added to the ceria lattice will increase the oxygen vacancies in the crystal and therefore improve the oxygen ion conductivity[12]. Doped ceria possesses some advantages over zirconia for use in oxygen transport applications. The ionic conductivity of doped ceria is present at intermediate temperatures (600°C - 800°C) is

sufficiently high for SOFC application. Gadolinium is the preferred trivalent dopant for this application of ceria as its ionic radius results in a minimum binding energy for defect clusters in the cerium lattice[5]. Gadolinium dope ceria (GDC) is the focus of much of the current research and development efforts for SOFCs operating in the intermediate temperature range. GDC based SOFCs typically use lanthanum strontium cobalt ferrite, $La_xSr_{1-x}Co_yFe_{1-y}O_{3-\delta}$, (LSCF) as a cathode material[13], [14]. By moving out of the temperature range of YSZ cells, GDC based SOFC systems can make use of low cost and reliable metal components for much of the surrounding system architecture. This makes their widespread deployment more likely and as such will be the focus of this work.

2.2.3. Bismuth Oxide

Bismuth oxide (Bi_2O_3) is a more recent focus of materials development for SOFC electrolytes. The bismuth oxide crystal contains two intrinsic oxygen vacancies per unit cell[15]. This makes it a very desirable candidate for SOFC electrolytes because no dopants are necessary to create vacancies for transport. However, to maximize the ion transport pathways, the crystal must be in the cubic phase. The maximized symmetry of this phase means that there are more potential oxygen lattice sites for ion movement. The oxygen lattice in the cubic phase is disordered at higher temperatures. This phenomenon is a key reason for the high ionic conductivity of this material. At the lower temperatures that are the current focus of SOFC research, bismuth oxide will not retain the cubic phase and the ordering of defects destroys the high ionic conductivity[15].

Doping of the bismuth oxide crystal with rare earth elements, primarily erbium, has shown promising results for stabilizing the lattice disorder down below the pure bismuth oxide phase change temperature. Continuing from this discovery, an expanded range of cation dopants and double doping schemes have been investigated to improve stability and performance of this material[16], [17].

To be used as an electrolyte material for SOFCs, bismuth oxide must be paired with another ionically conductive ceramic in a bilayer configuration. Bismuth oxide is not stable at the oxygen partial pressure range present at the cell anode and will decompose if exposed. By using a layer of GDC to shield from the fuel side, an overall lower electrolyte resistance can be achieved.

2.3. Stack Design

The most common configuration for SOFC systems comprised of multiple cells is the SOFC stack. The stack is a sandwich structure containing planar SOFCs and metallic interconnect layers that double as gas transport manifolds[18]. Figure 3 shows a cross-sectional diagram of a SOFC stack with the main components labeled.

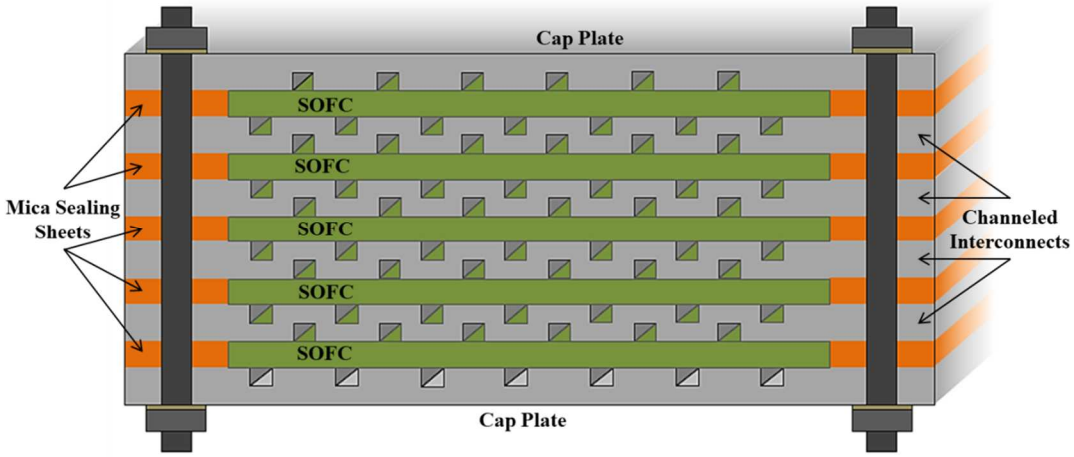

Figure 3: Cross-section diagram of 5-cell SOFC stack

The stack is compressed using electrically insulated bolts spanning the full height of the structure. The compression ensures good electrical contact between the metal interconnects and the SOFC electrodes. The gas environments at the anodes and cathodes of each cell are isolated by the compressed mica sealing sheets layered around each cell. When pressed between the interconnects, these layers form a gas-tight seal and prevent mixing of the fuel species and air. It is critical to isolate these two atmospheres to prevent both loss of performance caused by chemical short circuits, and uncontrolled combustion of fuel which could damage or destroy the stack and nearby components.

The conditions that will be experienced by the cell are largely determined by the design of the stack they are placed into. For this reason, research and development efforts for this technology must address the specific design and composition of SOFCs, as well as the impact of design decisions made for the components that will interact with the cells. One example of this is the balance between sealing pressure

and SOFC mechanical strength. Placing the stack under greater pressure will improve the gas seals, but also increase the chance of a SOFC fracturing. Only by fully understanding the safe limits of these variables can an informed and high quality system design be developed.

Chapter 3: Ionic Transport and Electrochemical Impedance Spectroscopy

3.1. Phenomenon of Impedance

Impedance is an electrical phenomenon comprised of the resistance, inductance and capacitance of a circuit. While typically applied to electrical circuits, the general concept of impedance applies to any system involving the movement of charge carriers. Resistance is the simplest of the components of impedance and is defined by Ohm's law as the ratio of voltage to current in a simple direct current circuit.

$$\boldsymbol{R = \frac{V}{I}} \qquad \textbf{(6)}$$

Inductance and capacitance are slightly more complex phenomenon that arise when alternating current is used. Inductance is caused by the magnetic field created by current flow in a conductor. This field then in turn induces a current in the opposite direction to the original. Inductance will be present whenever there is a change in the magnetic field associated with current flow[19]. Capacitance is the accumulation of opposite charges on two sides of a circuit element. In a DC circuit, this charge buildup will continue until the dielectric separating the charges is overcome by the localized potential. However, in an AC circuit the behavior will vary depending on the frequency. At very low frequencies, elements with capacitance will behave similar to the DC case. At higher frequencies, the current direction will switch before the dielectric is overcome and the accumulated charge will dissipate before accumulating again in the opposite configuration. This dependence on frequency

means that the impact of capacitance on the total impedance will decrease as frequency increases[19]. This has powerful implications for the characterization of electrochemical devices and will be addressed in Section 3.3[20], [21].

3.2. Charge Movement in Solids

A solid oxide fuel cell may be viewed as an electrical circuit involving both electrons and ions as the means of current. Half of the circuit is the external electrical conductor where whatever desired external load may be placed and electrons comprise the current. The other half is the cell itself where electrons combine with molecular oxygen to form oxygen ions in the cathode layer. These now become the vehicles for current until the anode where the fuel oxidizes and electrons are released into the electrical conductor.

The components of the fuel cell can therefore be treated similarly to conventional circuit elements and evaluated using the concepts defined in the preceding section[22]. In doing so, it is important to understand the differences in charge transport between electrical conduction and ionic conduction. Placing the mechanisms of ionic transport and formation within the framework of electrical theory, a detailed understanding of the activity within the solid state device may be achieved.

The primary difference in conduction between ions and electrons arises from their size difference. Electrons are able to travel through a material when they have

sufficient energy to enter the conduction band of that particular material. Metals generally have conduction bands that overlap their valence bands which makes them excellent electrical conductors[23]. Electrons are small enough so as to have very little spatial impact on the crystal lattice of the material they are moving through. This is not the case for ionic motion. Ion radii are of the same order of magnitude as the atoms that comprise the crystal lattice. This means that to move from one lattice site to the next, the surrounding lattice must actually deform to accommodate the passage. The energy required to stretch these interatomic bonds is referred to as the activation energy of the ionic conduction and is the reason that most solid ionic conductors require elevated temperature to function.

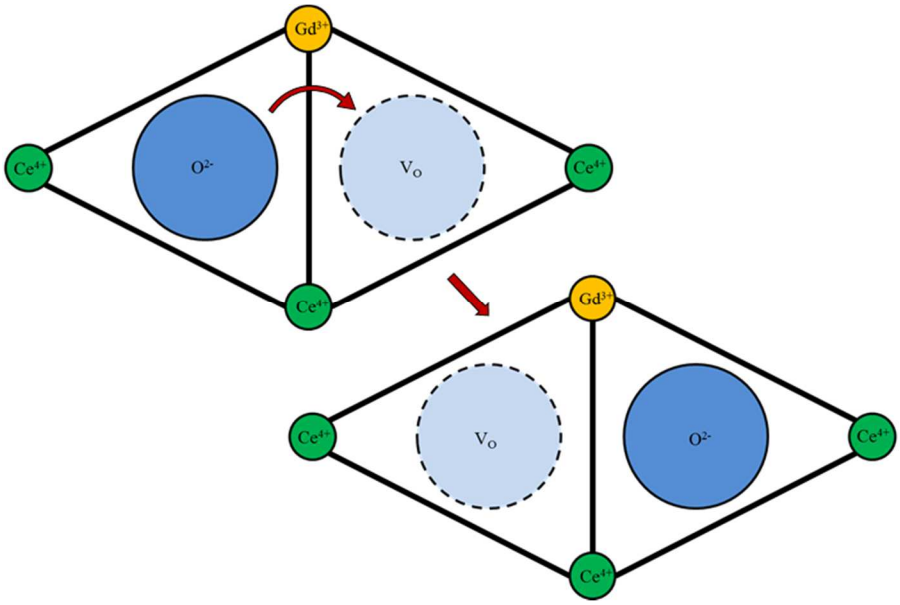

Figure 4: Concept diagram of oxygen ion transport mechanism in GDC

The concept illustrated in Figure 4 holds true for fluorite structure ceramics. It has been experimentally determined that in Bi_2O_3 there is an intermediate position,

known as the *32f* site, occupied by the oxygen on its way between the *8c* sites shown above[24]. This type detail is important for understanding the fundamental mechanisms at play and the ways in which the conductivity of a sample can change over time, but will not be addressed in depth in this work.

3.3. Application to SOFCs

3.3.1. Relevant Mechanisms

In both fuel cells and batteries, impedance measurements are one of the primary methods for evaluating device performance and diagnosing deficiencies in various device components. The term used to describe this measurement of impedance is electrochemical impedance spectroscopy, or EIS. In this technique, an AC signal with a pre-defined voltage amplitude is applied to the material or device over a frequency range typically including 10^{6} Hz to 10^{-2} Hz. The current response from the sample is recorded at each frequency and can be used to calculate each component of impedance discussed in Section 3.1. The most commonly used result of this technique is the Nyquist plot, in which the imaginary reactance is plotted against the real resistance of the sample from high to low frequency[7], [19], [22]. In SOFCs, Nyquist plots offer a very efficient method for determining the total cell impedance as well as the contribution of a number of different mechanisms to this total.

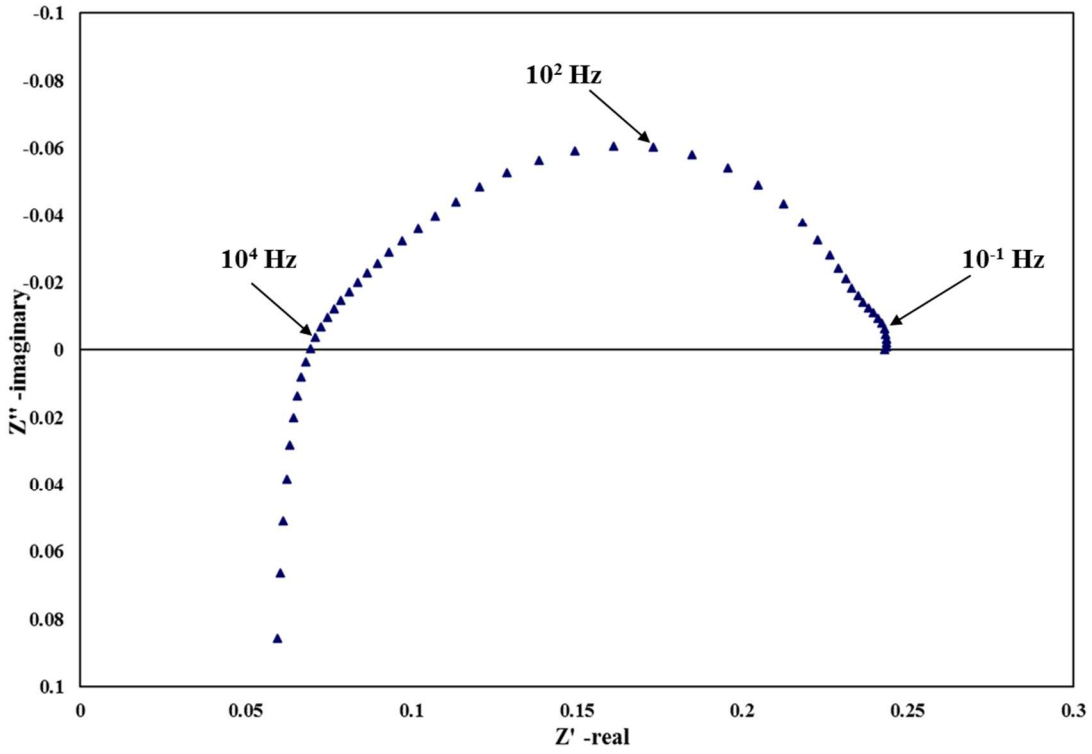

Figure 5: Impedance spectra obtained from GDC/Ni-GDC cell with LSCF-GDC cathode

Figure 5 shows an example of a Nyquist plot from an anode supported GDC SOFC with frequency labels. The very high frequency points that rise to meet the Z'-axis are an inductance tail and are not meaningful for the mechanisms of interest. As such, this data is usually omitted[7], [22], [25], [26]. The intersection with the Z'-axis represents the ohmic portion of the impedance and is associated with the ionic conductivity of the cell electrolyte. The frequency is sufficiently high to avoid capacitive effects and allows the isolation of the ionic resistivity. As the frequency decreases, the imaginary component of the impedance becomes relevant and a number of arcs form. Each of these arcs represent a mechanism involved in transport of the charge carrier species. For SOFCs, these are solid state ionic conduction,

electrode reaction kinetics, and mass transport in the electrodes[7], [19]. The frequency ranges where these phenomena appear often overlap and deconvolution can be difficult. The frequency range where the imaginary impedance component is present is known as the non-ohmic impedance and includes the kinetics of dissociation of reactant species on catalytic surfaces, the incorporation of oxygen ions in the cathode, and the mass transport process of reactant molecules to the TPB sites[19], [22], [27].

There can be other mechanisms present in a fuel cell besides those discussed, such as ionic conduction across grain boundaries in some electrolyte materials or charge build up between layers in the device. However, in the materials focused on in this work, these other phenomena are usually not major factors in cell performance and health.

3.3.2. Equivalent Circuits

A method for extracting more quantitative results about a specific component or reaction in a fuel cell is to perform a data fit using a theoretical equivalent circuit. There are an infinite number of theoretical equivalent circuits that could be built but for useful information to be obtained, each element used in the theoretical model should represent a real world mechanism within the material or device. The common approach to equivalent circuit construction in SOFC EIS measurement is shown in Figure 6. The in-series inductor and resistor represent in inductance tail and ohmic impedance while each parallel resistor-capacitor pair represents on o the non-ohmic arcs seen in Figure 5[22].

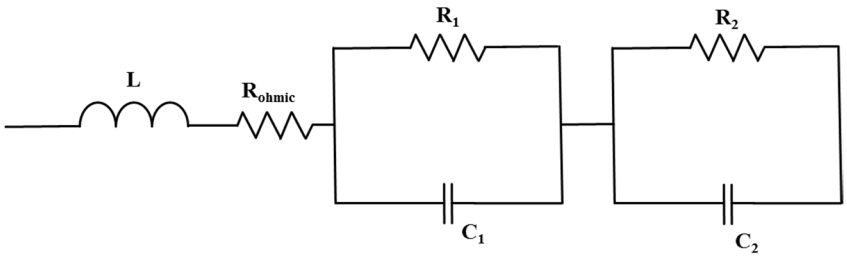

Figure 6: Common equivalent circuit used for fitting SOFC impedance spectra

Once a reasonable equivalent circuit is constructed, the characteristics of each element (resistor, inductor, etc.) should be adjusted to closely match the EIS data. This fit can then be used to supply specific quantitative values for the time constant, capacitance, and other characteristics of each individual mechanism.

Chapter 4: Fundamentals of Brittle Fracture

4.1. Stress in Materials

Stress is defined as force over an area in an object and uses the unit of pascals where 1 Pa = 1 N/m. In a simple uniaxial loading case such as Figure 7, the perpendicular cross section is the relevant area and the stress is uniform throughout the object.

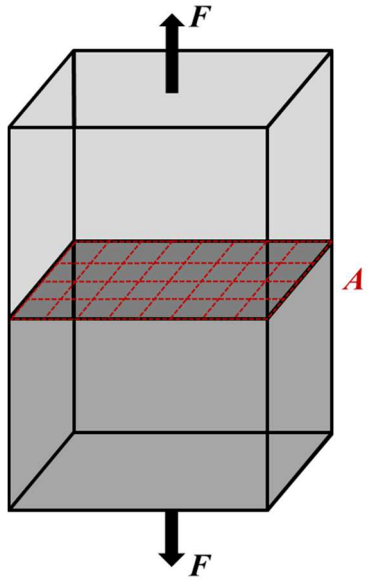

Figure 7: Pure uniaxial loading concept

Depending on how the force is applied and the geometry of the object, different locations in the object will experience different stress magnitudes. A good example of this can be seen in Figure 8, where the horizontal center of the symmetrically supported beam is pressed down. The lower edge of the beam experiences a tensile stress and the upper edge is in compression.

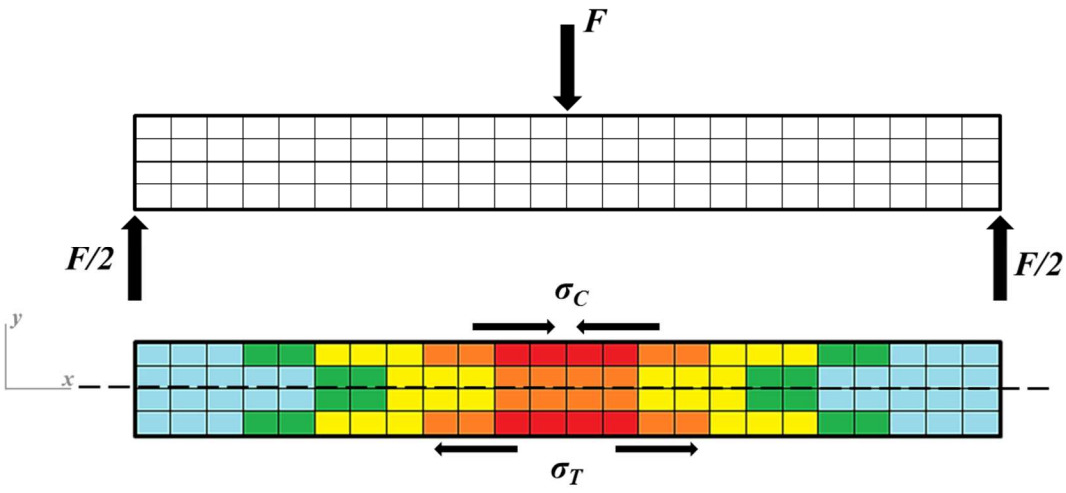

Figure 8: Bending stresses in a symmetrically supported beam

Additionally, the farther one moves from the centerline of the beam, the greater the stress magnitude experienced by the material. The plane in the material where the compressive and tensile stresses cancel out is known as the neutral plane[28].

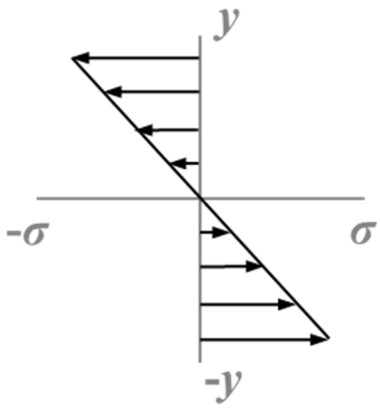

Figure 9: Stress variation by depth in symmetrical beam under bending conditions

Understanding and predicting stress distributions in an object is a key part of failure testing and engineering design. Through determining the stresses that a device or component will experience, design geometry and material selection can be made so as to lower the chance of mechanical failure.

4.2. Crack Behavior

Failure of a component, in a mechanical sense, occurs when the geometry of the component has changed sufficiently so as to be unable to fulfill the role the component was designed for. Depending on the role of the component, mechanical failure may mean everything from a deformation of millimeters to catastrophic rupture. Failure must therefore be understood through the lens of the design specifications of the components in question.

The geometry of a solid may only change through two fundamental pathways: rearranging of constituent atoms or a change in the number of constituent atoms. The rearranging of atoms is generally referred to as deformation. Cracking, wear, and corrosion are all phenomena that involve the loss of constituent atoms[28], [29]. Of these four mechanisms, deformation and cracking are the most directly related to mechanical stresses experienced by the object. Materials are considered “ductile” when their primary mechanical failure mechanism is deformation, while “brittle” materials will crack and fracture before any significant deformation takes place. At the root of these behaviors is the structure of the material at the atomic level.

At the core of fracture is the concept of crack propagation. For an object to fracture, a crack must propagate through the object until the object is no longer structurally sound. The movement of the crack tip requires some amount of energy which is provided by the localized stress at the crack tip. The energy threshold for the crack to move is related to the increase in surface energy related to the change of area related to the crack[30]. Griffith first described fracture in terms of free energy and developed the model of a crack growing as a means to reduce the potential energy near the tip. As this happens however, the overall surface energy of the object will increase due to increasing total area. This leads to the "critical crack length" concept, where once a crack reaches a certain length, the energy reduction from relieving the local stress outweighs the increase in surface energy and it becomes energetically favorable for the crack to grow and it proceeds through the object[30].

Solid oxide fuel cells and other solid state electrochemical devices are primarily composed of ceramic materials which are brittle. The theoretical strength of most ceramics, based on bond energy between atoms, is far higher than most metals. In practice, there are always defects present from manufacturing and/or wear during use. These defects allow cracks to form at loading conditions well below where the calculated elastic modulus of the material would predict failure[31]. Therefore, brittle fracture must be the focus of efforts to study the mechanical properties of these devices.

Various defects and subtle differences exist in engineering materials and play an enormously important role in how and when failure occurs. As addressed previously,

ceramic materials are especially affected by the defects present within them, which can vary considerably between seemingly identical components. In order to predict failure chance in this case, a statistical model must be employed. In simple terms, this entails testing some number of samples and extrapolating information about all samples from those findings. Because ceramics generally exhibit a wider range of failure loads compared to metals, a larger test set should be used if a high degree of confidence is desired. It is common practice to use Weibull statistics for this purpose[29].

4.3. Role of Defects

The role of defects in the mechanical performance of SOFCs is enormously important. Aside from common ceramic defects such as microcracks and internal voids, portions of the SOFC intentionally contain structures that can be viewed as defects from a fracture mechanics viewpoint. Specifically, the porosity of the electrode layers causes the effective strength of those layers to be significantly lower than the measured strength of their component materials. As described in Section 2.1, SOFC electrodes must contain open porosity for gaseous reactants to be able to move to the triple phase boundary reaction sites. Electrodes with higher porosity will have improved gas transport ability, but this advantage must be balanced with the losses to mechanical strength this entails. The mathematical model developed to describe the relationship between porosity and strength in ceramics is Equation 7.

$$\sigma_f = \sigma_f^0 e^{-n\rho} \quad (7)$$

Where σ_f^0 is the material's measured fracture strength when fully dense, ρ is the porosity fraction, and n is a fitting parameter[32]. The experimental verification of this relationship for the specific materials used in SOFC construction is needed to inform design decisions of electrode layers.

A second source of mechanical failure in SOFCs is the final device geometry. When a planar SOFC is fired, the constituent materials of the various layers possess differing shrinkage rates. This can either lead to delamination of the layers or to a significant deviance from the original planar shape. This camber can be mitigated using weighted setter plates during the sintering step, but achieving a perfectly flat cell is very difficult. When a stack of cells is compressively sealed, the variance in height of the cells will result in internal stresses and fracture if the stress is sufficiently great.

These two characteristics of anode supported planar SOFCs therefore require that both the component materials and the constructed cells be evaluated for mechanical strength under both standard and operating conditions. This information is necessary for informed design decisions to be made in the creation of a SOFC based power generation system.

Chapter 5: Experimental Techniques

5.1. SOFC Fabrication

5.1.1. Tape Casting

Tape casting is a common method for fabricating technical ceramic objects. Subtractive machining is not advisable for ceramic materials due to the high likelihood of fracture during the process. Because of this limitation, most engineering components composed of ceramic materials must be created in their final shape by densifying powder into the desired geometry. In most cases, the shaping of ceramic powder is a separate step from the thermal densification and the green component must be handled while not actually fused into a single object. Organic binder substances are often mixed in with the ceramic powder to improve the cohesion of the shaped powder. A plasticizer chemical can also be added to form a composite matrix of ceramic powder in an organic matrix. Via heat treatment, the organics and be burned out leaving only the ceramic behind in the original shape. Once the ceramic is sintered, the finished object retains the shape of the composite. Given the right constituent substances, it is possible to make this composite flexible so that much more complex shapes and structures can be created than if densified ceramics were the starting pieces[33].

Tape casting is a process for creating sheets of ceramic/polymer composite material with very consistent dimensions. The tapes created using this method are flexible and are suitable for use in constructing ceramic devices. The preparation of a tape casting

slurry is a multistep process. The initial slurry is created by mixing the ceramic powder or powders into a solvent liquid, typically ethanol, along with a dispersant to avoid clumping. Menhaden fish oil is a common and effective dispersant in ethanol slurries. Once this mixture has been thoroughly combined via mechanical mixing, the secondary ingredients are added. The organics added in this step act as either binders, such as polyvinyl buteral, or as plasticizers, such as benzyl butyl phthalate. These chemicals ensure that there is good adhesion between the ceramic particles and the surrounding mixture and that the final tape is pliable enough to not crack or tear easily. Following the addition of the final ingredients, further mechanical mixing is done to ensure even dispersion of the slurry components. Ceramic milling media of various sizes is often added to help with this mixing.

Once a slurry is completed, any air trapped in the now quite viscous mixture must be removed to avoid bubbles or voids in the final tape. This is accomplished by placing the slurry in a low pressure chamber and mixing with a low rpm impeller. Care must be taken to avoid excess solvent evaporation during this step to preserve the desired viscosity while still removing air.

To cast the tape, a sloped reservoir with an open bottom and side is placed on a long sheet of polymer film. A precision milled steel blade is placed in the open side of the reservoir such that a small gap exists between the polymer sheet and the blade. This gap is adjusted to the desired thickness of the tape. The polymer sheet is drawn between two rollers at a set velocity and the slurry is poured into the reservoir. As the sheet is drawn under the stationary reservoir, the slurry is pulled through the

measured gap under the blade. This results in a layer of slurry with the width of the reservoir and the thickness of the blade height[33]. After exiting the reservoir, the tape passes over a warm surface to help it set. After drying for 12-24 hours, the tape may be removed from the machine, rolled up, and stored.

There are a large number of variables involved in successfully creating a tape and the parameters used will vary widely depending on the materials used and the end use of the created tape. Figure 10 shows a conceptual schematic of the tape casting process.

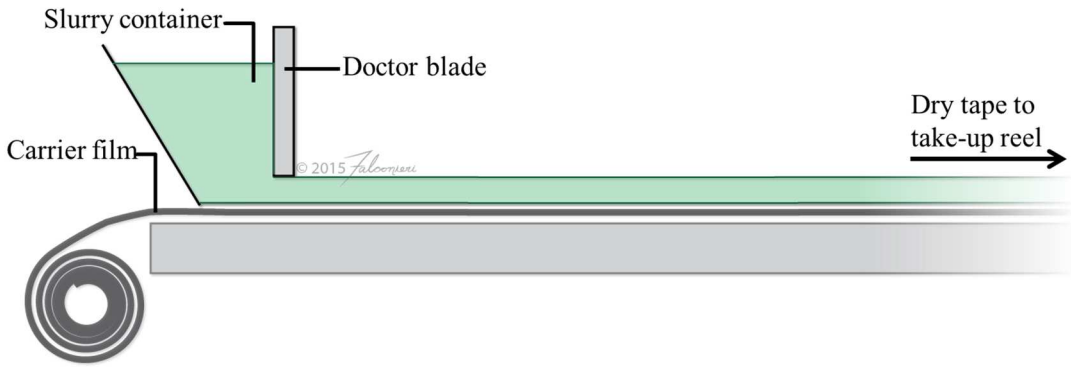

Figure 10: Tape casting concept schematic [Image credit: Falconieri Visuals]

5.1.2. SOFC Construction

The construction of a finished, lab-scale SOFC is a multistep process. Multiple layers of tape cast ceramic/polymer composites, referred to as "tapes" for the remained of this document, are layered to build the final structure. Anode support layer (ASL) tapes consisting of powdered nickel oxide mixed with GDC powder are used to create the foundation of the cell. These tapes are relatively thick compared to the other cell layers and three pieces of anode tape are layered together to construct the anode

support layer. These layers are joined using a Carver 4386 heated hydraulic press using a pressure of 2000psi for 30 minutes at 180°F. Once the ASL has been pressed together, the joining steps are repeated with the thin anode functional layer (AFL) tape and with the 20µm electrolyte tape. The layering of tapes is shown in Figure 11.

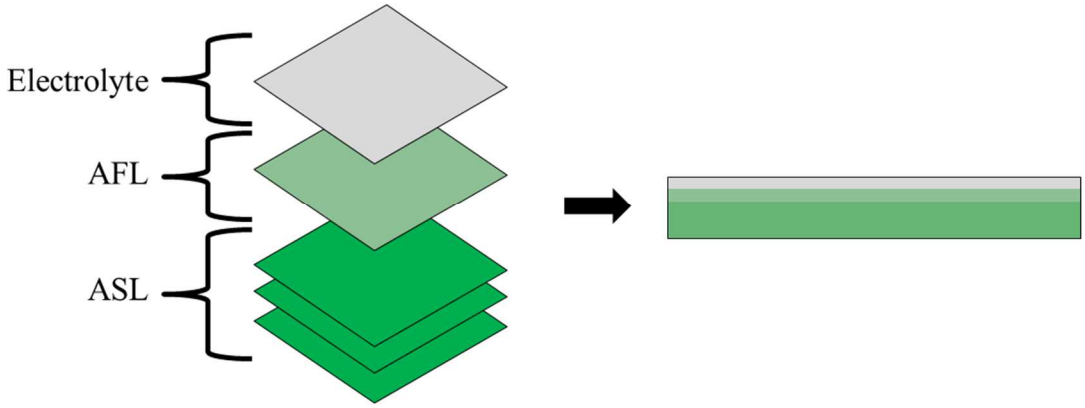

Figure 11: Layering of SOFC tapes and resulting structure

Following these steps, the ASL, AFL, and electrolyte layer are all present and the layered tape structure has cooled. A 1.25in steel die is then used to punch out discs from this layered tape structure. A pre-sintering process, shown in Figure 12, is used to remove the organic components (dispersant, binder, plasticizer, pore-former) from the punched discs.

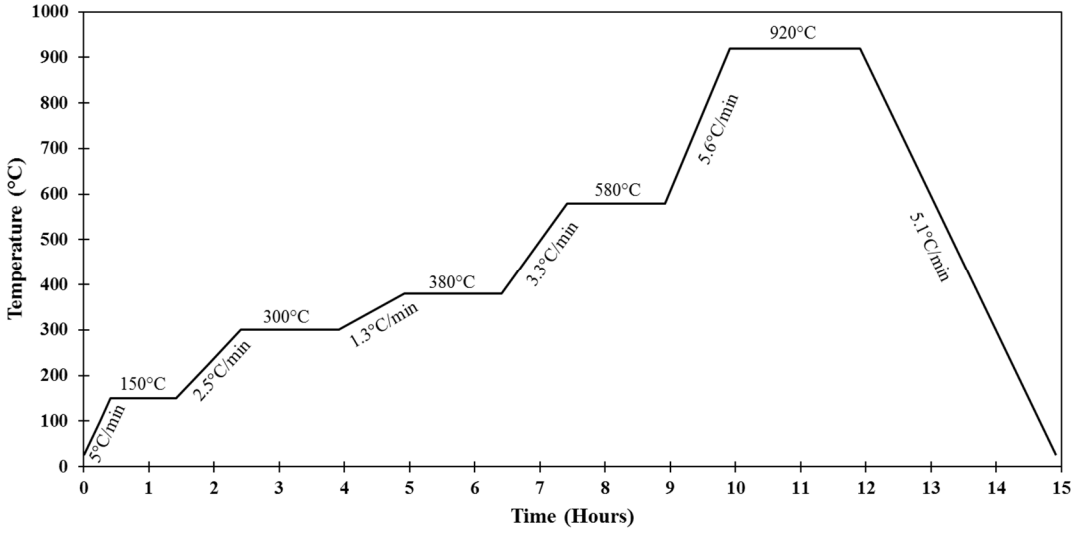

Figure 12: SOFC pre-sinter schedule

The product of the pre-sintering process is green-body half-cells. Lacking the organic compounds from the tapes, these green bodies are very fragile and brittle. To sinter the green bodies into finished half-cells, a sintering profile composed of ramping at 5°C/minute to 1450°C with a 4 hour hold at this temperature. Cooling was done at 5°C/minute. The sintered half-cells are much more mechanically durable and can be handled more easily.

To add the cathode layer, an ink composed of a 50:50 mixture by weight of LSCF and GDC10 powder suspended in commercial solution was screen printed to form a 0.31cm^2 circular cathode area centered on the electrolyte side of the disk. The ink was dried in a 100°*F* oven and then fired at 1100°C for 2 hours. The firing of the cathode layer results in the porous structure that allows gas transport discussed in Chapter 2.

5.1.3. Anode Infiltration

Attempts at improving performance stability of GDC SOFCs were made by modifying the interior surfaces of some cell anodes. The anode pores were infiltrated with a GDC precursor solution ($Ce_{0.9}Gd_{0.1}O_{2-\delta}$ in DI water, 1M) prepared from nitrates of gadolinium and cerium (Alfa Aesar) and fired at 400 °C for 1 hour. The infiltration was performed by depositing drops of the solution onto the anode surface and then placing the cell into a low pressure chamber to enhance penetration through the anode layer by capillary actions. This process was repeated a number of times to achieve the desired amount of cerium oxide loading in the cell. Cell weight was measured prior to infiltration and after each firing. The target loading was between 3 and 4 weight percent.

5.2. SOFC Electrochemical Testing

5.2.1. Reactor and System Schematics

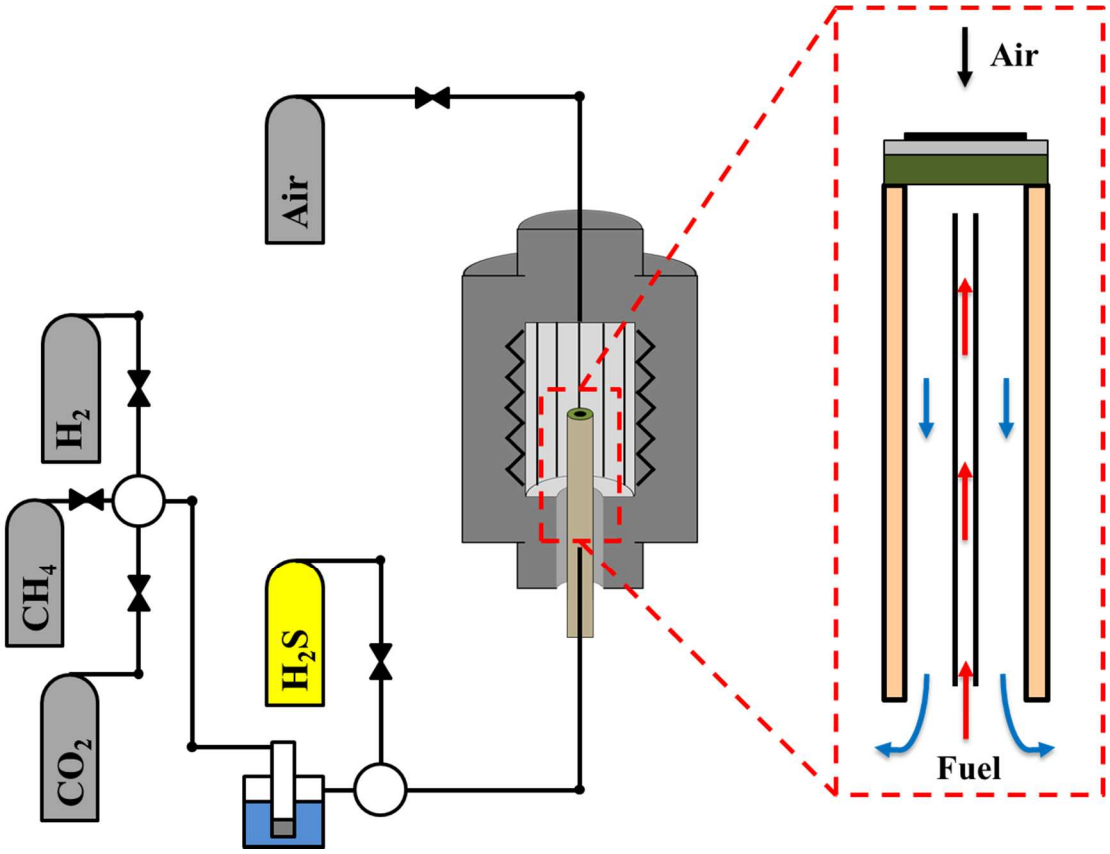

Figure 13: Diagram of SOFC button cell test system with reactor

5.2.2. Testing Procedures

A Solartron CellTest System composed of a 1470E potentiostat and a 1400 frequency response analyzer was used for electrochemical measurements. All direct electrochemical testing of SOFCs was based on a procedure designed to provide all the relevant data on cell performance and health over time. Following the initial heating of cell to the chosen operating temperature and sufficient hydrogen exposure

of the anode to reduce nickel oxide, initial benchmark measurements were taken of each cell. Measuring open circuit voltage (OCV), EIS, and a galvanodynamic scan provide information on the quality of anode sealing, the area specific resistance (ASR), and the current-voltage (I-V) relationship of the cell from which electrical power can be calculated.

To determine the effects of long term operation of SOFCs on various fuel compositions, the electrochemical measurement schedule chosen was periodic in nature. For the majority of time during this testing scheme, the cell was held a galvonostatic condition meant to approximate real world operating conditions. Every hour during the long term galvanostatic testing, EIS and I-V scans were taken to provide the periodic snapshots of cell health (EIS) and performance (I-V).

Measurement of the thermal energy produced by the operation of SOFCs involved uninterrupted operation at a fixed current. This ensures consistent heat production over a long window which in turn allows higher resolution of temperature vs. time measurement. Due to this requirement, EIS and I-V measurements were taken at the beginning of testing and the galvanostatic voltage response was used as the sole measure of performance trends in these experiments.

5.3. Mechanical Testing Sample Preparation

Two types of samples were created for mechanical testing experiments. To investigate basic material properties and the effects of porosity on strength, rectangular bar samples were fabricated using GDC10 powder (fuelcellmaterials, #111101). Polymethyl methacrylate (PMMA) spheres or flake graphite were used as a sacrificial pore former in some samples to create controlled levels of porosity in some of these bars. For investigating the effect of the laminated structure of anode supported SOFCs, rectangular sample coupons were cut from tape cast laminates identical to those described in Section 5.1.

The pressed bars were created by placing GDC powder and either PMMA spheres or graphite flake into a rectangular steel die press with inner dimensions of 30.3mm by 10.2mm. The die was placed into a Carver hydraulic press and pressed at 2 metric tons for 5 minutes. After removing the pressed bar from the die, the die was cleaned of any residual powder and the next bar was pressed. The green-body bars were heated to 400°C to remove organics and then fired at 1500°C for 4 hours to sinter the GDC. Due to shrinkage from sintering, the final bar dimensions were 22mm x 8mm with some small variation through the batch. Any bars with significant warping, surface defects, visible cracking, or discoloration were discarded after sintering. The porosity targets used in this work were 10%, 30%, 50%, and 70%. The final porosities of the bars were measured via the Archimedes method and were typically slightly below the target due to densification from sintering. Prior to testing, each bar or coupon was measured using precision calipers and the exact dimensions were recorded for mechanical stress calculation.

The ASL and half-cell coupons used in the flexural testing were made using tape casting at a 700 micron blade height. The tapes were left to dry overnight before being cut into 12cm by 12cm squares. Three squares were stacked and hot pressed as described in Sub-Section 5.1.2. Following this lamination, the tape was cut into rectangular coupons measuring 25mm by 10mm. The coupons were fired at 1400°C for 4 hours. For half-cell coupons, a GDC slurry was tape cast with a 40 micron blade height. After the lamination of the three ASL layers, a single layer of electrolyte tape was laminated to the ASL. The sintering procedure for half-cell coupons was identical to the ASL coupons.

5.4. Three-Point Flexural Testing

Traditional tensile tests, where a sample is secured with clamps and pulled axially until failure, are not suitable for testing ceramic materials. Samples are likely to crack at the clamping points which make the collection of useful data very difficult. Additionally, the fact that fracture in ceramics is strongly influenced by preexisting defects means that in a uniaxial tension test, predicting the location of failure is very difficult due to the nearly homogenous stress field in the sample.

The three point bend test is a suitable alternative for obtaining mechanical strength data in the case of ceramics. A rectangular bar sample of the material is placed on two supports with a fixed span. A load is applied downward in the center of the span at a constant rate until the sample experiences fractures. The maximum load (the load at

failure) is recorded and used to calculate the flexural stress which caused failure using Equation 8, where *L*, *b*, and *d* are sample dimensions *length*, *width*, and *height*.

$$\boldsymbol{\sigma = \frac{3FL}{2bd^2}} \qquad \textbf{(8)}$$

5.5. Microscopy

5.5.1. Scanning Electron Microscopy

Scanning electron microscopy (SEM) was used in this work to analyze multiple sample types for a variety of reasons. Energy-dispersive X-ray spectroscopy (EDS) was used in conjunction with SEM imaging when investigating chemical compositions of surfaces. All SEM images were taken using a Hitachi SU-70 SEM with a Bruker XFlash silicon drift EDS detector.

Samples were not polished or modified using other surface treatments commonly used for SEM samples. This decision was made given the importance of viewing the surface of samples with as little changed as possible from the testing conditions, mechanical or chemical, that they had experienced. However, the lack of surface preparation did result in lower quality SEM micrographs in some cases. This did not have a significant impact on the findings from the images.

5.5.2. Transmission Electron Microscopy

Transmission electron microscopy (TEM) is an applicable technique when specific information on the micro- or nanostructure of a given sample is needed. TEM

requires the sample being examined to be very thin (20nm - 200nm) so that electrons are able to transmit through the material[34]. TEM fills a particular role given its ability to resolve features on the same order as atomic lattice distances. This can be used to probe features that are glossed over in SEM.

In this work, TEM was used to more closely examine contaminant build-up on the surfaces of sub-micron sized particles of SOFC anode material. The images taken were tangential to the curvature of the particles, so as to look through the cross section of any present contaminant species. The instrument used in this work was a JEM 2100 FE-TEM.

5.6. Surface Analysis

5.6.1. Raman Spectroscopy

Raman spectroscopy was employed as a supplementary characterization technique to provide additional information about the chemical state of SOFC anodes following long term exposure to sulfur containing hydrocarbon fuel. Raman spectroscopy makes use of the Raman Effect, wherein a very small fraction of the photons incident on a material will inelastically scatter. The energy transferred from or to the light by the atoms or molecules is measured by the difference in the wavelength of the scattered light from the original source wavelength. The characteristics of this energy transfer from a known laser light source allows for both qualitative and quantitative analysis of material samples[35]. For most solids, Raman spectroscopy can only sample the surface, as the incident light usually does not penetrate any meaningful

distance into the bulk of the material. However, this can be preferable if the surface chemistry of a sample is the region of interest for measurement.

A cell which was operated on only wet hydrogen and air served as a reference. Measurements were performed using a Horiba Jobin Yvon LabRam ARAMIS Raman microscope with a 532nm laser. The instrument was calibrated with a Si wafer at 520.7cm^{-1}. All spectra were normalized to the 1030-1280cm^{-1} region, corresponding to the Ni-O band.

5.6.2. X-Ray Photoelectron Spectroscopy

Identification of the chemical changes that occur in the anode of SOFCs when exposed to and operated on fuels containing damaging chemical species is critical to developing methods for preventing or mitigating harmful effects. X-ray photoelectron spectroscopy (XPS) is a surface analysis technique where the surface of a sample is bombarded by x-rays while the number and kinetic energy of the emitted electrons is measured. The kinetic energy of the electrons gives the binding energy, and different chemical species have unique spectra of emission peaks at various binding energies. The fact that the measured spectra correspond to the electronic state of an atom means that a large amount of information including concentration and charge state of the surface (~10nm depth) can be gathered[36].

XPS measurements were performed in a Kratos Axis 165 X-ray photoelectron spectrometer, with a monochromatic aluminum X-ray source operating at 1400 keV. The spectra of interest for post-operation SOFC anodes were Ce, Ni, O, C, and S. The

anode of a cell which was operated on only wet hydrogen and air served as a reference. Data analysis was performed using CASAXPS software.

Chapter 6: Multi-Environment Mechanical Behavior of Porous Ceria and Ceria-Based SOFCs

6.1. Study Rationale

Commercial deployment of solid oxide fuel cells requires the development of effective manufacturing methods and the design of an electrical power system to make use of them. These challenges involve solving a number of problems that are not present in the scientific research environment. The most immediate challenge is how to provide adequate sealing for full size SOFCs in a multi-cell stack. For planar SOFCs, a standard stack design consists of a number of square cells separated by metal interconnects, as described in Section 2.3. Sealing of these stacks is accomplished by compressing the layered structure which includes sealing material. As more compressive force is applied to the stack, the quality of the seals improves. However, any cell which is not perfectly flat will experience flexural stress as a result and this can lead to cells fracturing. Due to the brittle nature of the ceramic materials that constitute solid oxide fuel cells, a very thorough understanding of the mechanical limits of these devices is critical to their successful deployment.

The vulnerability of SOFCs to mechanical failure is a well-known issue. However, much of the research into this phenomenon has been focused on yttrium stabilized zirconia (YSZ) based devices[37]–[39]. This material has been the standard for the field and has desirable mechanical properties but requires high temperatures to function well. As efforts are made to lower SOFC operating temperatures, a shift to

ceria-based electrolytes has occurred. Much less attention has been given to the mechanical behavior of doped ceria materials across SOFC operating conditions.

Much of the study of fracture in ceramic materials has been done on technical ceramics for medical applications and for coating metal components[40]–[47]. These materials are optimized for fracture toughness and durability and very rarely experience temperatures above a few hundred degrees Celsius. The fracture surface analysis and correlations between microstructure and strength described for these materials are a valuable starting point for investigating fuel cell materials. However, there is a lack of extensive investigation into the properties of intermediate temperature SOFC materials at their expected operating temperatures and environments.

Efforts have been made to comprehensively examine the mechanical properties of SOFC materials and the effect of non-standard conditions on those properties. Nakajo et al. conducted a wide ranging study of materials used in anode supported SOFCs which included some attention to temperature and atmosphere effects[39]. While providing a solid base of material knowledge, this work did not fully cover materials beyond YSZ and there remains a need for further testing, especially for doped ceria. Flexural strength and Young's modulus measurements for gadolinium doped ceria (GDC) have been carried out in ambient conditions by Yasuda et al. They characterized the effects of sintering temperature on density and the resulting mechanical properties[48]. Further testing of this material system at elevated

temperatures and reducing environments must be done to fully understand the mechanical behavior of GDC.

This study presents the results of a range of flexural tests involving the materials using in ceria-based anode supported SOFCs along with the assembled half-cells. Using a purpose-built temperature controlled environmental chamber installed in a universal testing machine (UTM), porous doped ceria bars, anode support layers composed of nickel and doped ceria cermet, and half-cells composed of an ASL and a doped ceria electrolyte were tested. The various test conditions used included expected operating temperatures (450°C - 650°C), and both reducing and oxygenated atmospheres. These variations in test conditions are important because these cells must maintain their integrity from when they are first placed in a sealed stack to when they reach operating conditions. In particular, this study was intended to determine at what point in their life SOFCs are most vulnerable to mechanical failure and the mechanisms involved. Additionally, the effect of the anode-electrolyte interface on flexural strength was explored.

6.2. Mechanical Test Fixture Design and Construction

6.2.1. Mechanical Fixture Materials Selection

To develop a testing apparatus capable of simulating the various conditions experienced by operating SOFCs, appropriate materials were chosen based on thermal and chemical stability criteria. Alumina (Al_2O_3) is one of the most common

technical ceramics available and is relatively inexpensive. Additionally, it is very chemically stable and has a high hardness value. This makes it well suited for bend tests as measured deflection can be attributed to the sample and not the fixture. Diamond-tipped end mills were used to machine out the desired hollows and cuts were performed using a diamond grinding saw. The construction of the three-point bend fixture out of a single material mitigates any structural damage that could arise from different thermal expansion behavior when the system is raised to SOFC operating temperatures.

6.2.2. Three Point Mechanical Fixture Construction

The lower half of the fixture is immobile and is where the sample rests during testing. The sample rests crossways on two 6.35 mm diameter rods which are placed in troughs separated by 20 mm. The troughs are cut into a rectangular block with dimensions of 40 mm x 25 mm. This block is secured on top of another equally dimensioned bock which has a cylindrical hole bored into underside with a depth of 5mm and diameter of 12.7 mm. The support rod is secured in this hole and extends 300mm down to the anchor point of the UTM. All secured joints between alumina components are joined using silica-based high temperature cement.

The upper half of the fixture consists of a 12.7 mm diameter rod which has a 6.35 mm wide half-cylinder trough cut into one end. In this trough, a 6.35 mm diameter rod is secured perpendicular to the main rod using silica cement. The main rod extends up to the crosshead anchor point on the UTM. Assembly and alignment is assisted with

the use of a 3D printed bar-jig to ensure repeatability. Figure 14 shows the 3D concept model of the fixture baseplate along with the assembled final product.

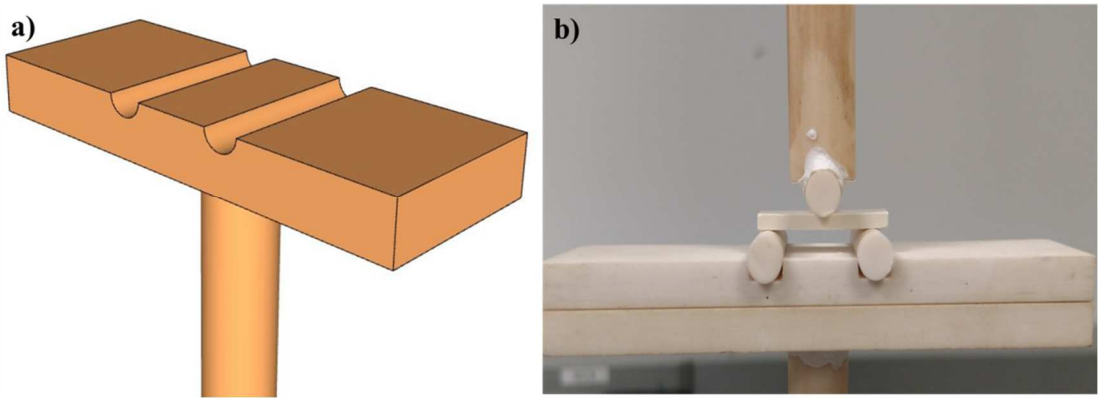

Figure 14: a) 3D concept model for alumina three-point bend fixture baseplate; b) Assembled alumina three-point bend fixture with loaded sample

6.2.3. Temperature Control System

Following the creation of the alumina fixture, a heating system capable of reaching SOFC operating temperatures was developed. 12 in x 12 in steel plates were assembled into a cube with cutouts in the top, bottom, and front faces. Steel wire mesh was used to create a 6 x 6 x 6 in compartment in the center of the case. Silica-based wool insulation was packed between the center cavity and the case walls. Nickel-chromium alloy heating elements were installed in the cavity and connected to an external PID temperature controller. A K-type thermocouple was inserted through the insulation to the center cavity to measure temperature. The two pieces of the alumina bend fixture were then inserted into the top and bottom of the furnace and

secured to the anchor points of the UTM. The furnace was placed on a supporting scaffold to hold it in position during tests.

6.2.4. Atmosphere Control System

To create the atmosphere control system, a combination of standard and custom vacuum system parts were used. For the main body of the chamber, a 3 inch inner diameter, stainless steel tee was made with QF80 Flanges on the top and middle sections on the tee. The bottom tapered down to a QF50 sized flange with two NPT ports welded in. On top of the tee, at the QF80 port, a custom-made reducer was added to reduce it to QF50 while adding two additional NPT ports. Figure 15 shows the engineering drawings and rendered image of the custom pieces fabricated by A&N Corp.

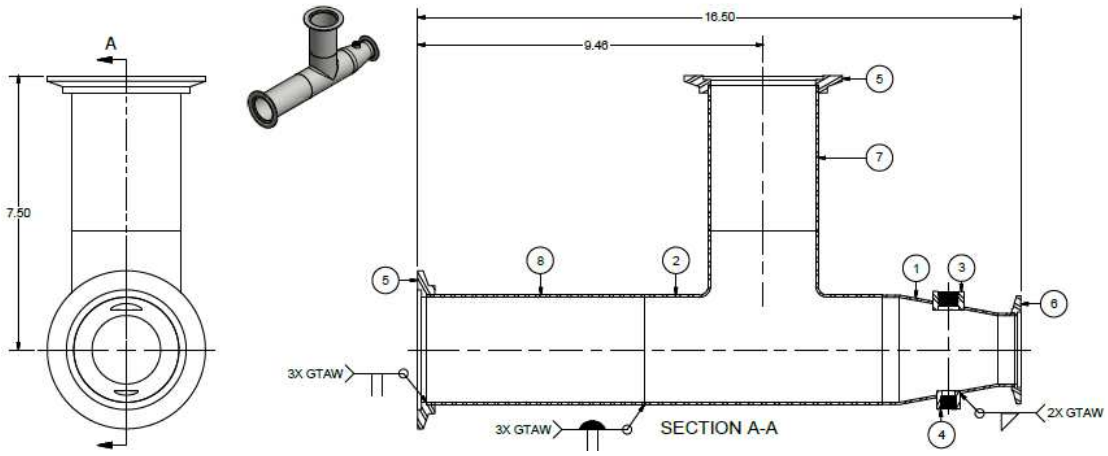

Figure 15: Engineering drawings of mechanical testing atmospheric chamber (provided by A&N Corp.)

The NPT ports on top and bottom allow for gas inlet and outlet and the placement of a thermocouple through a Swagelok ultratorr fitting. Gas flows were controlled via

manual rotameters. Flexible bellows on top of the chamber allows the motion of the cross-bar to be translated into the fixture, requiring the subtraction of the spring force to be removed during analysis. The alumina fixture pieces were then inserted through each end and into the chamber within the furnace. An additional layer of silica wool insulation was placed around the testing system to prevent temperature fluctuations.

6.2.5. System Verification

In order for valuable data to be gathered on the mechanical properties of SOFC materials, the three-point bend fixture required verification to ensure that there were no large sources of error being introduced into measurements by some feature of its construction. To accomplish this, a set consisting of ten pressed GDC bars containing 50% porosity was fabricated via the process described in Section 5.3. The samples were randomly divided into two groups, one being assigned to the newly constructed alumina fixture while the other was assigned to a steel three-point bend fixture with identical dimensions. The sets were tested at room temperature in air, and the results compared to verify the validity of the newly constructed fixture.

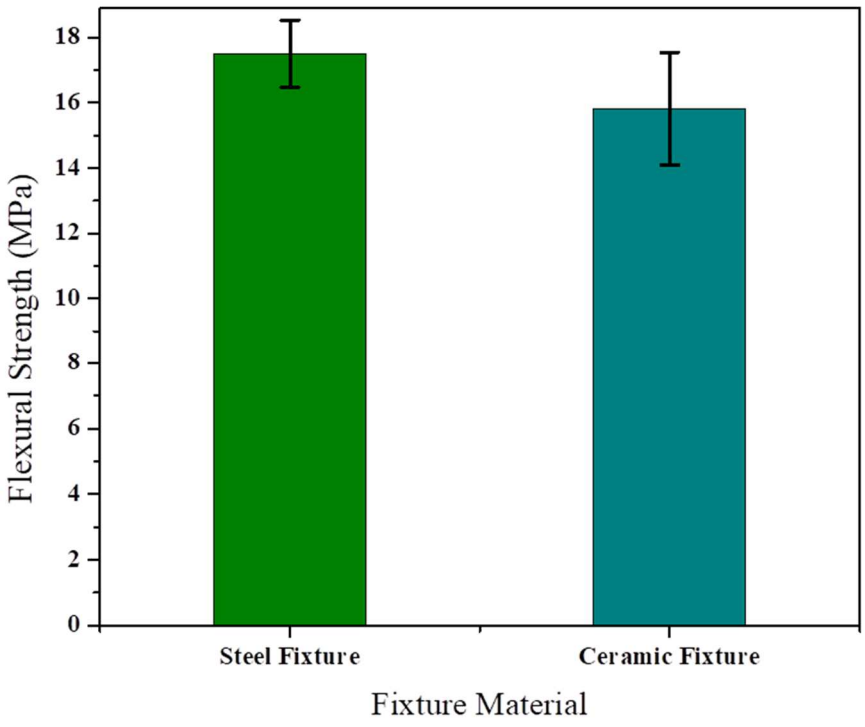

Figure 16: Comparison of steel and alumina three-point bend fixtures for ~50% porous GDC pressed bars (Air, 25°C)

Figure 16 shows the results of the validation test. The mean strength recorded on the steel fixture was slightly higher by comparison to the alumina fixture, but within the standard error of the sample sets. Given this similarity of measurement results, the alumina fixture was considered to be capable of providing valid strength data.

6.3. Experimental Design

6.3.1. Sample Creation

Pressed GDC bars containing porosity ranging from 10-70% were created using uniaxial pressing as described in Section 5.3. The porosity was created using either spherical PMMA or flake graphite. Bar dimensions were measured after sintering for stress calculation purposes.

The nickel oxide-GDC ASL and half-cell coupons were created via tape casting and hot lamination as described in Section 5.1 and Section 5.2. The coupons were cut from the laminate prior to sintering and then separated randomly in to test condition groups. Each test condition was assigned five of each coupon type (ASL only, half-cell electrolyte up, half-cell electrolyte down). Each sample was marked with an identifying alphanumeric code so fracture surface analysis could be performed, and dimensional measurements were taken. The average coupon dimension was 8.16 mm x 24.15 mm x 2.98 mm.

6.3.2. Flexural Testing

All tests conducted in the Tinius Olsen 10ST UTM were done at a crosshead rate of 0.2 mm/min with a 20 mm lower span. During loading on the 3-point system, the lower region of the sample experienced tensile stress while the upper region experienced compressive stress. The “electrolyte-up” and “electrolyte-down” denominations indicate whether the electrolyte layer experienced compressive or tensile stress during the test. At room temperature, the coupons were loaded into the

fixture and tested. For sample sets at elevated temperatures in ambient atmosphere, the samples were loaded into the front of the chamber, acting as a staging area, prior to heating the fixture. Upon transferring the next coupon from the staging area to the fixture, a 20 minute waiting period was used to ensure that the coupon had reached thermal equilibrium prior to testing. Following the completion of the set, all coupon pieces were cooled at a rate of 10°C/min. For testing in reducing atmosphere, each coupon was reduced and tested individually. Using thermogravimetric analysis (TGA) results, a reduction time of 18 hours at 650°C was chosen so as to achieve sufficient reduction of the nickel oxide in the coupon using humidified (3% H_2O) Argon containing 3% H_2. Figure 17 shows the mass loss of Ni-GDC anode material in this atmosphere.

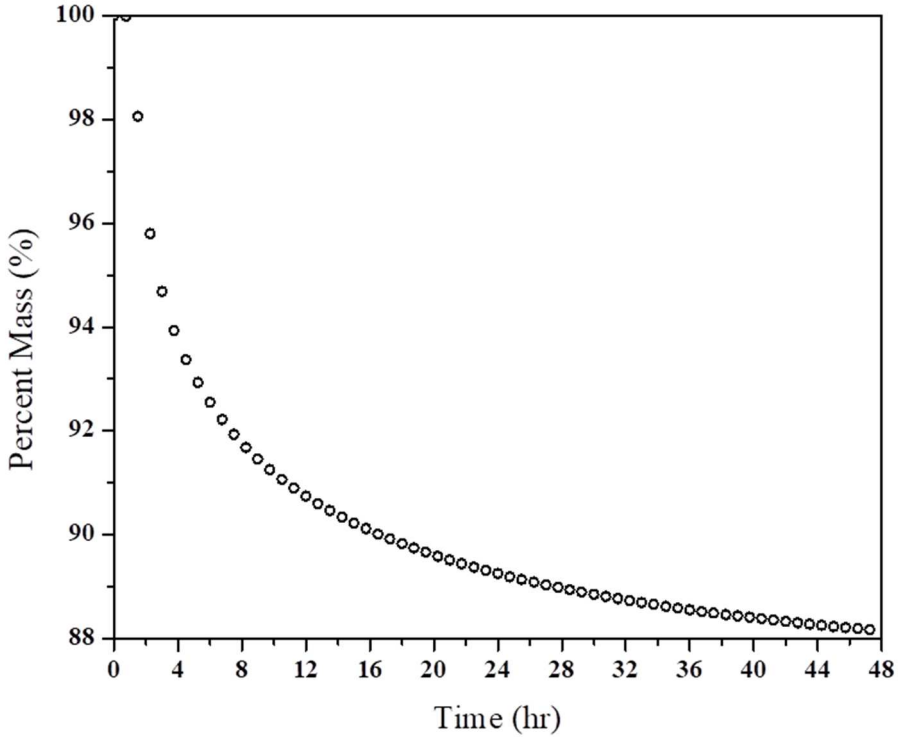

Figure 17: Thermogravimetric Analysis results for Ni-GDC SOFC anode reduction in 3% H_2O 3% H_2 balance Ar

At the conclusion of this 18 hour window, the sample was tested and the next sample was loaded for reduction.

6.3.3. Fracture Surface Microscopy

Following the destructive test, SEM analysis of the fracture surfaces were performed. The purpose of this post-test examination was to observe the trans-granular, inter-granular, or mixed nature of crack propagation, and to find any anomalous features on the fracture surface. Magnifications of x2.00k – x10.0k were found to be appropriate for viewing fracture surface details.

6.4. Mechanical Strength of Porous Ceria

In agreement with literature data, GDC bars with greater porosity displayed lower flexural strength values as compared to less porous samples. The relationship between porosity and strength followed an exponential trend. This behavior is well established for porous ceramics and is described by Equation 9[49].

$$\boldsymbol{\sigma = \sigma_0 e^{-\eta P}} \qquad \textbf{(9)}$$

σ_0 is the material flexural strength when fully dense, P is the porosity volume fraction, and η is a constant dependent on the material and microstructure of the sample.

The flexural strength measurements of pressed GDC bars containing various levels of porosity at room temperature and 650°C are shown in Figure 18.

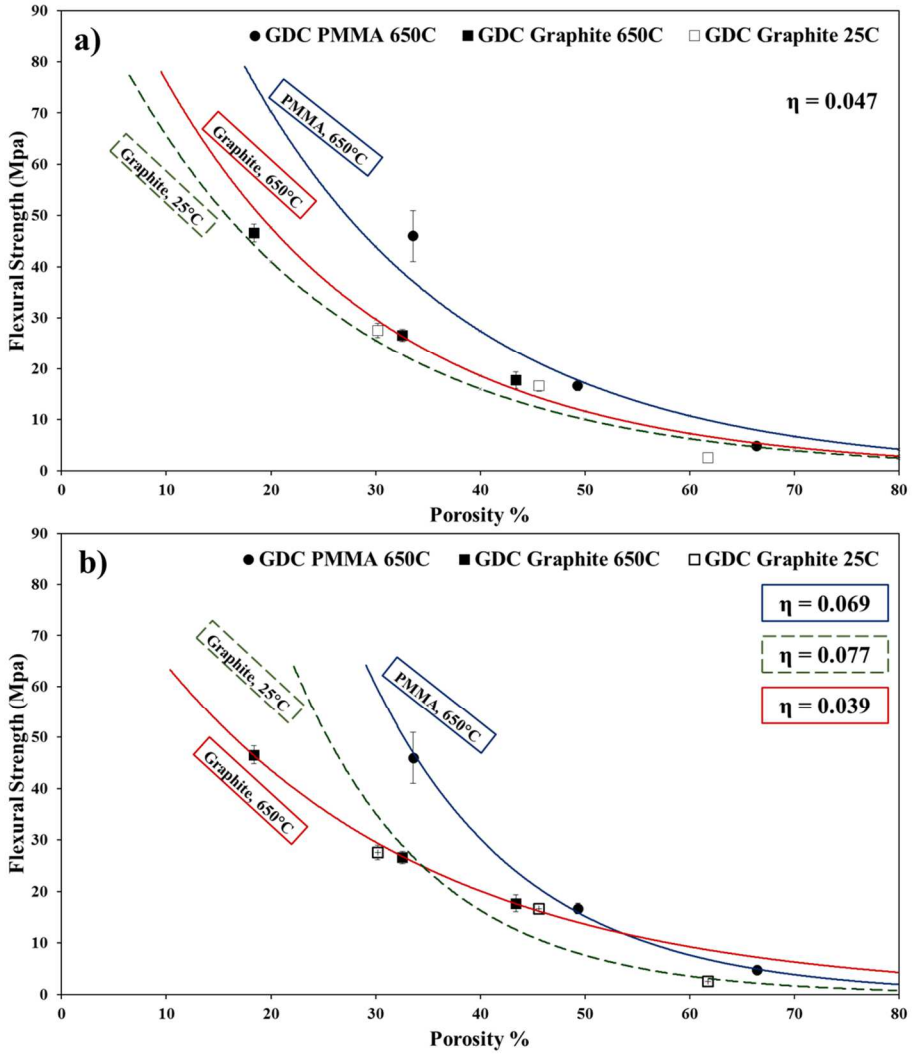

Figure 18: Flexural strength-porosity dependence for porous GDC10 at 650C and 25C using spherical PMMA or graphite flake pore former: a) Measured strengths fitted using fixed geometric constant; b) Measured strengths fitted using different geometric constants

The trends shown in Figure 18 (a) are constrained by a fixed value of η that has been previously reported for GDC, while Figure 18 (b) uses variable η. The variable η fitting approach matches the measured data at 650°C much more closely than when η is a fixed value. This is unsurprising given the radically different pore geometry between the data sets.

SEM micrographs of the fracture surfaces of various sample sets (Figure 19) illustrates the very different microstructural states created by the use of the different pore formers.

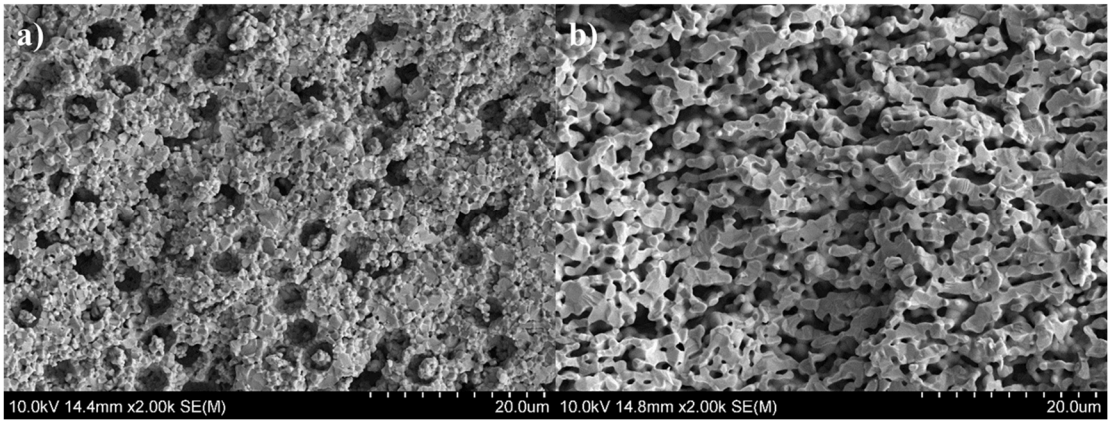

Figure 19: SEM micrographs of porous GDC10 bars made using: a) PMMA pore former; b) graphite flake pore former

The spherical pores created by PMMA burn-out largely retained their shape during the sintering process and did not strongly affect the surrounding dense material. In contrast the graphite flake created thinner and more interconnected pore structures which appears to have lowered the size of the fully dense areas of ceramic. This "stretched out" microstructure caused by the graphite flake pore-former is much less resistant to fracture.

Samples with porosity formed using PMMA spheres showed significantly greater strength as compared to samples with graphite-formed porosity. This can be explained by the effect of pore geometry on crack initiation and propagation in the ceramic. If a crack enters a pore, the pore can now be considered the new crack tip. The energy required to advance the crack is highly dependent on the geometry of the

tip. For a spherical pore, this geometric factor is maximized and results in higher resilience for fracture.

Based on the mechanical behavior of these samples, porous ceramics should be designed and constructed such that the pore geometry is as low aspect ratio as possible to maximize strength.

6.5. Mechanical Strength of SOFC Anodes and Half-Cells

The capability to vary atmosphere as well as temperature for three-point bend tests of the system developed in this work allowed a multi-variable study of the effect of environment of GDC-based SOFC structures. The anode support layer was evaluated first, due to its role as the mechanical "backbone" of this cell design. Figure 20 shows the effect of temperature on the flexural strength of tape-cast ASL coupons.

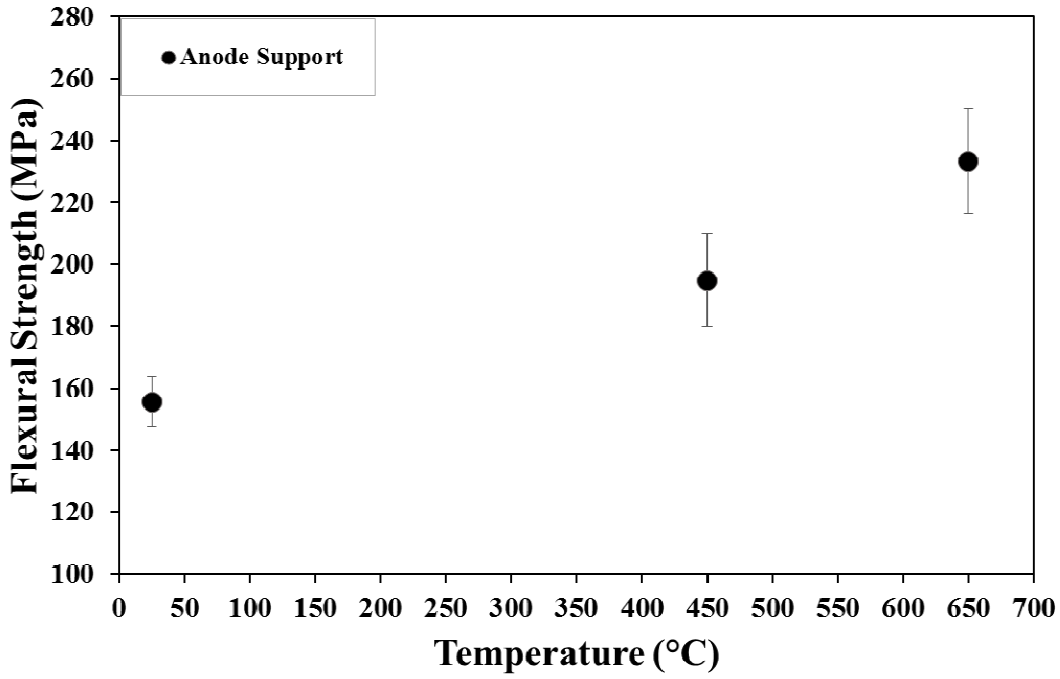

Figure 20: Temperature dependent strength of tape-cast nickel oxide-GDC10 cermet anode support coupons in air at 25°C, 450°C, and 650°C

The strength of the ASL layer in air increased linearly with temperature. This is expected behavior for ceramic materials, as thermal expansion causes micro-cracks and other small defects to close up and raises the energy required to initiate crack growth. In cermet samples such as these, large differences in thermal expansion behavior of the constituent materials could degrade strength at elevated temperatures but this is not the case for this formulation.

The electrolyte layer in an anode supported SOFC is very thin relative to the ASL by design, but unlike the ASL it is fully dense and homogeneous. Depending on the cell orientation and direction of bending stress, it is possible that the electrolyte layer could have a significant effect on the strength of the cell. Half-cells (ASL + electrolyte) were tested under the same conditions as the ASL samples. The

electrolyte side of the laminated structure was placed in either tension or compression. Figure 21 show the half-cell results overlaid with ASL strength.

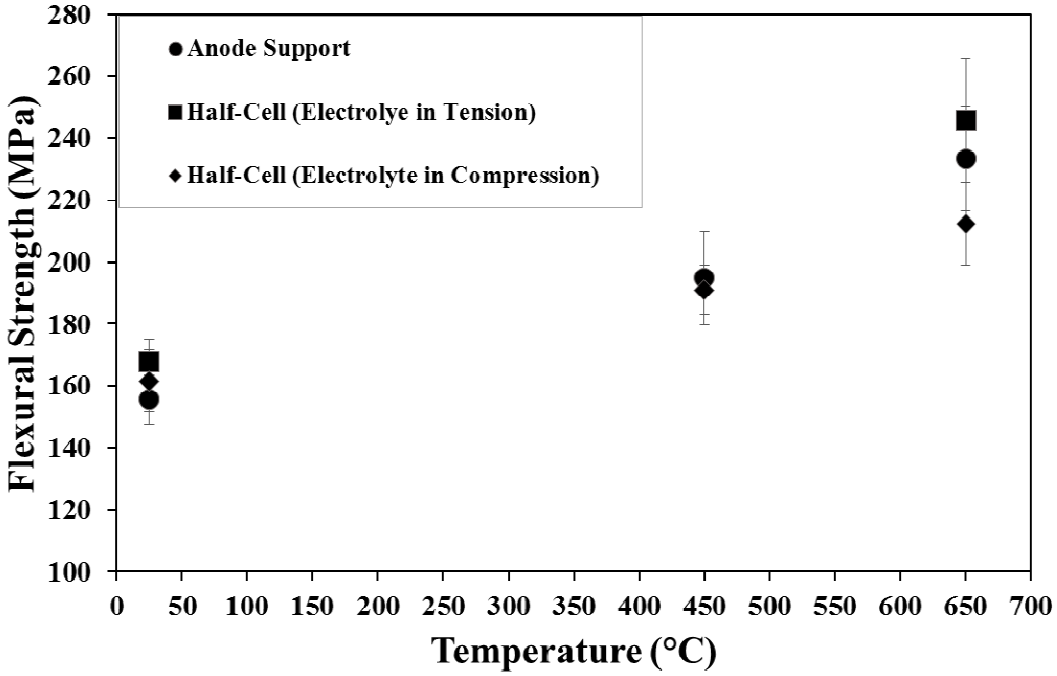

Figure 21: Temperature dependent strength of SOFC ASL and half cells tested at 25°C, 450°C, and 650°C

Based on the strengths shown in Figure 21, there appears to be a slight strengthening effect from orienting the cell such that the electrolyte layer is placed in tension rather than compression. This is more apparent at elevated temperature. However, based on statistical analysis, there is no significant difference in the strength between the three sample types at each temperature.

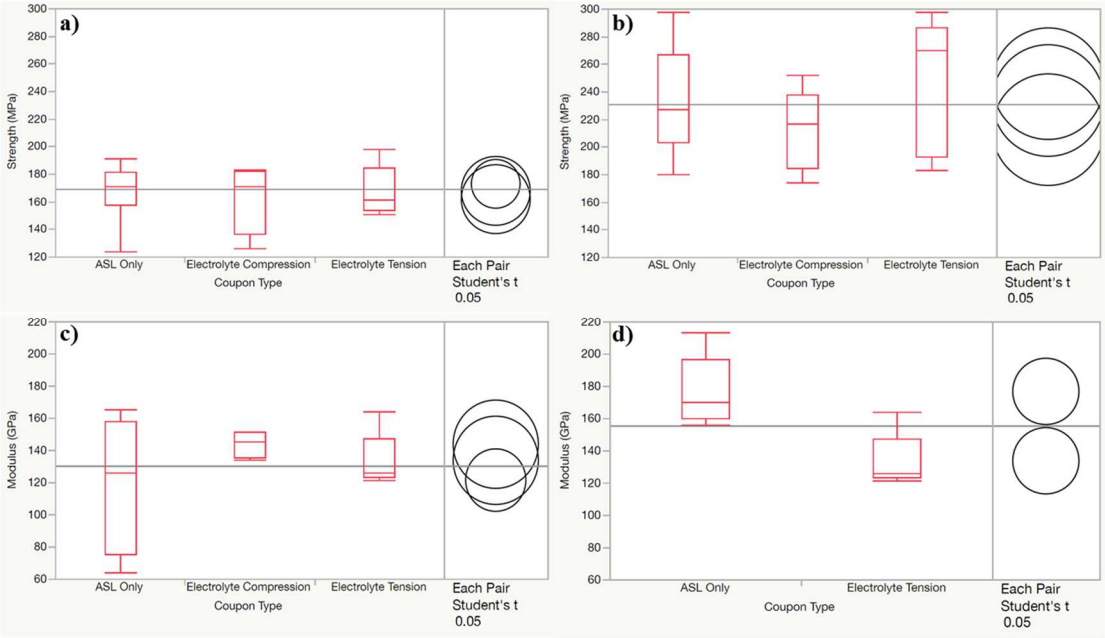

Figure 22: Student's t-test for strength and modulus of sample sets: a) Strength at 25°C b) Strength at 650°C c) Modulus at 25°C d) Modulus at 650°C

The circles in Figure 22 show the degree of similarity between two sample sets. More overlapping circles correspond to more statistically similar data sets. At elevated temperature there was a significant difference between the modulus of ASL samples and samples with the electrolyte placed in tension. This difference was not present at room temperature. As the materials reach elevated temperature, small differences in elasticity will likely become magnified due to different thermal effects on dense and porous layers.

SEM analysis of the fractured half-cells showed very good adhesion between layers. Delamination is a common failure mode in layered ceramics and one that would be particularly damaging to SOFCs due to resulting ionic conductivity loss between layers[50]. Based on this observation, the process of uniaxial pressing followed by sintering creates a sufficiently strong interface between SOFC layers.

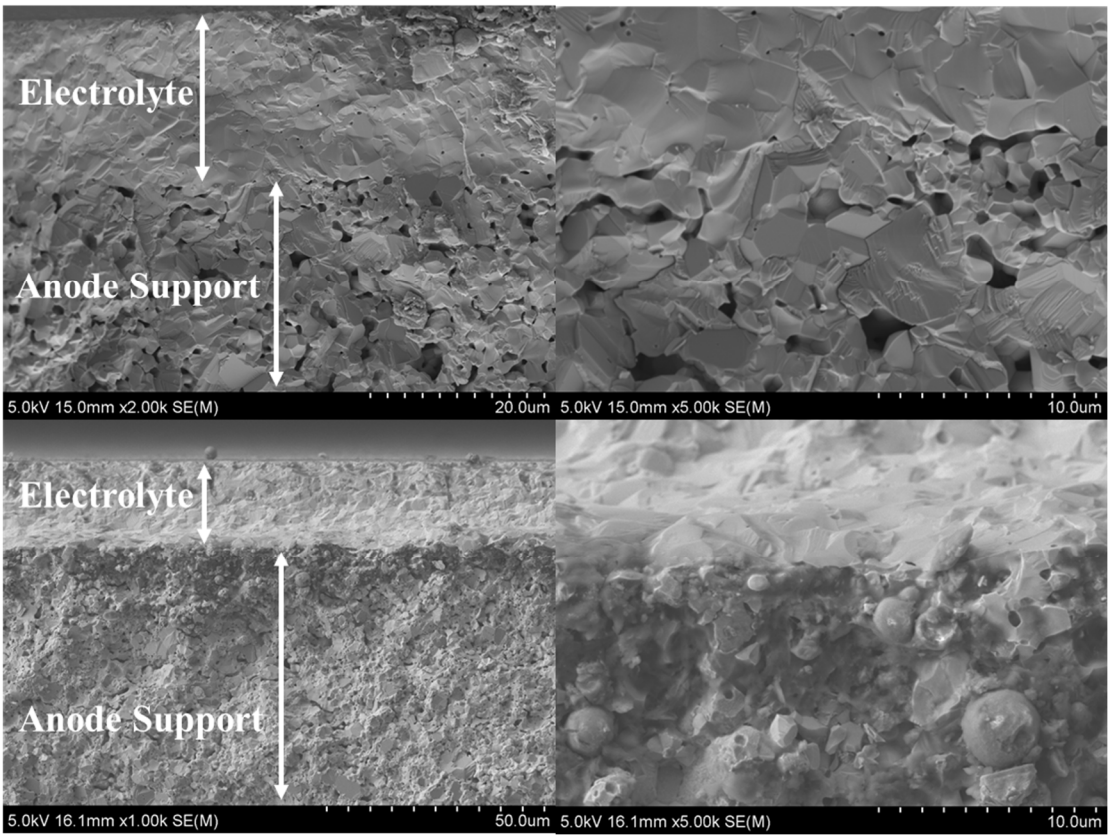

Figure 23: SEM micrographs of unreduced and reduced half-cell fracture surface: tested in air at 25°C (top) and tested in reducing atmosphere at 650°C (bottom), showing good adhesion between anode and electrolyte

In the half-cell coupons, it was clear that the fracture plane contained mixed transgranular and intergranular fracture. Some grains were sheared through while others remained whole. The x5.00k micrographs in Figure 23 (right) show a number of fractured grains with a number of small parallel ridges. This feature indicates the passage of the crack through the grain. Due to the mixed nature of this fracture, further testing of sample with varied grain size is required to isolate the effect of grain structure on the mechanical strength of these devices.

Each of the three types of coupon samples (ASL, half-cell with electrolyte in tension, half-cell with electrolyte in compression) were also tested at 650°C in a reducing gas

environment to approximate the condition of SOFC operation. Figure 24 shows the measured strengths compared to the samples tested in air.

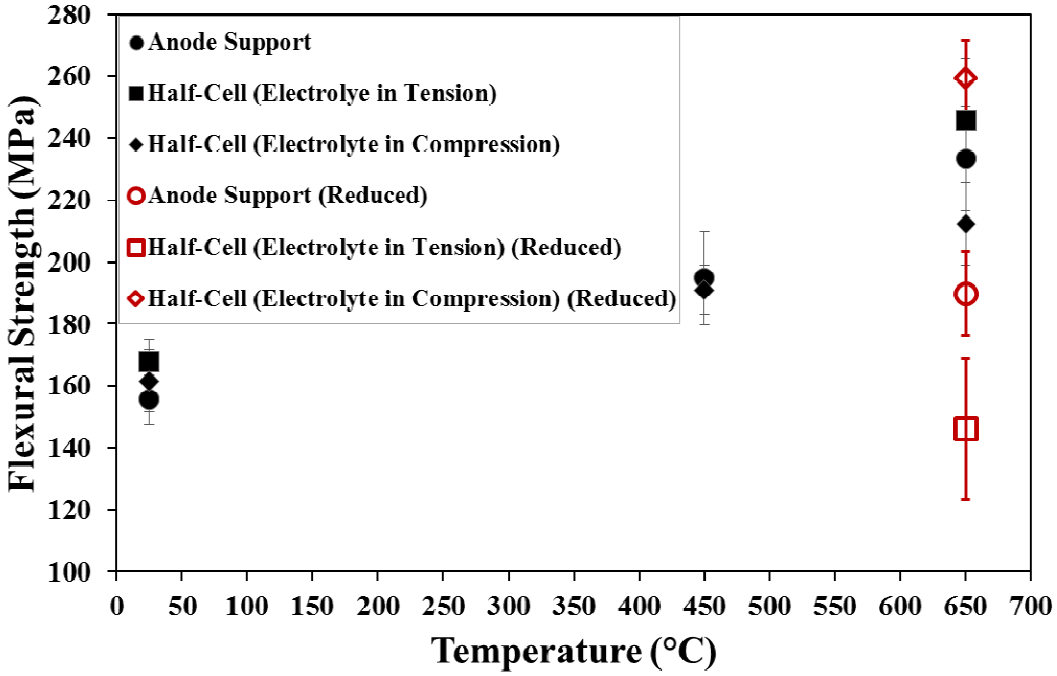

Figure 24: Temperature dependent strength of Ni-GDC anode supports and half-cells in both air(black data points), and reducing atmosphere (3% H2, balance Ar)(red data points), tested in both "electrolyte-up" and "electrolyte-down" orientations resulting in the electrolyte layer experiencing tension and compression, respectively

All unreduced sample types showed increased strength at elevated temperatures with little difference between types at a given temperature. The high-temperature reduced coupons displayed large differences in strength depending on the orientation of the sample. Tests in which the dense electrolyte layer was placed in compression resulted in the highest strength values, while the samples were weakest when the electrolyte was placed in tension. In reduced samples, the anode support layer becomes a ceramic-metal composite and is therefore somewhat elastic while the electrolyte remains a brittle ceramic. The electrolyte-in-compression condition maximizes the

mechanical performance of the coupon by placing the layers in their preferred stress state.

6.6. Conclusions

A temperature and atmosphere controlled alumina three-point bend fixture was designed and built for use in a universal testing machine. The system was verified via comparison to a commercially available steel three-point bend fixture. SOFC coupons and component materials were evaluated for flexural strength at room temperature and IT-SOFC operating temperatures. The effect of stress orientation on the strength of SOFC half-cells at operating temperature and in reducing atmosphere was also investigated. In addition, the effects of porosity percent and pore geometry on flexural strength in gadolinium doped ceria were investigated.

Pore geometry was found to have a significant impact on the flexural strength of GDC10, with spherical pores showing the greatest resistance to fracture. This supports the concept of pores acting as the new crack tip once a crack has advanced to the pore. Additionally, samples at 650°C were stronger than those at room temperature. This is likely due to localized compressive stresses from thermal expansion. This hypothesis is further supported by the results of testing NiO-GDC anode support coupons and half-cells. Coupons tested at 25°C, 450°C, and 650°C displayed a linear strength dependence with temperature. This hypothesis is further supported by the results of testing NiO-GDC anode support coupons and half-cells. Coupons tested at 25°C, 450°C, and 650°C displayed a linear strength dependence

with temperature. There was no statistical difference in strength between anode support layers and half-cells composed of anode support and electrolyte at a given temperature in air. Half-cells in which NiO was reduced to Ni by exposure to H_2 at 650°C displayed significant differences in strength when the electrolyte layer was subjected to compressive stress as opposed to tensile stress. Placing the ceramic electrolyte in compression and the metal-ceramic composite anode in tension resulted in the highest strength.

This work leads to two important conclusions for the mechanical properties of GDC-based SOFCs using Ni anodes. Porous GDC used in anode supported SOFCs should be fabricated such that the pore geometry is spherical as this maximizes energy required to advance a crack through the ceramic. Secondly, care should be taken in stack construction to ensure any out-of-plane cells are placed to compress the electrolyte and place the reduced anode in tension so as to lower the chance of fracture.

The author would like to acknowledge the support of the Maryland NanoCenter and its AIMLab for the use of the SEM used in obtaining micrographs, A&N Corporation for the design and assistance in constructing the atmospheric test chamber, and the support of the Maryland Industrial Partnership (MIPS) Program.

Chapter 7: Improved Sulfur Tolerance of Ceria-Based SOFCs through Anode Surface Modification

7.1. Study Rationale

The fuel flexibility of SOFCs is one of the key advantages these devices have over other fuel cell designs. The ability to easily integrate SOFCs with existing hydrocarbon fuel infrastructure is a strong argument for their viability as a bridge technology. These fuels often have certain amount of impurities (e.g., H_2S), depending on the source and production methods[51]. Fuel contamination is a potentially serious hurdle to the widespread adoption of SOFCs as an energy generation technology[52].

The operating conditions of high temperature Ni-YSZ SOFCs make sulfur a particularly damaging fuel contaminant due to the high affinity for sulfur possessed by nickel and the fact that nickel sulfide formation is favorable at this temperature range[52]–[56]. Both of these realities mean that even trace amounts of sulfur can destroy Ni-YSZ based cells very quickly through both catalytic site occupation and cracking due to the volume change associated with nickel sulfide formation. Therefore, SOFC systems running on natural gas or other hydrocarbon fuels must use sacrificial scrubbers or an additional desulphurization system to remove any sulfur. This adds material and maintenance costs to any system and increases the difficulty of deployment.

Ni-GDC SOFCs operating in the low-to-intermediate temperature range can experience similar performance loss issues to the Ni-YSZ cells when exposed to sulfur but the mechanisms can differ. Physisorption of sulfur atoms to catalytic sites still occurs, but the favorable chemical reactions are different[57]–[59]. Sulfate compounds are more commonly formed and both nickel and cerium can be affected. Sulfur occupying catalytic sites during cell operation leads to oxidation of the nickel instead of oxygen ions reacting with fuel species[52]. The lower number of effective catalytic sites caused by the presence of sulfur will also enhance the damage from other chemical species which are present. This is due to a lower oxygen flux through the cell electrolyte that then prevents the oxidation and removal of species such as carbon. Overall, the level of damage done to Ni-GDC based SOFCs by sulfur is less than for Ni-YSZ cells. One explanation for this difference is the variable oxidation state of the cerium atom. This variability means that the ceria lattice can readily give up some amount of oxygen and prompt gaseous sulfur dioxide formation which lowers the local effective sulfur concentration, thus preventing chemical reactions with the anode structure[59], [60].

This phenomenon can be used to design SOFC anodes with greater tolerance for sulfur poisoning[61]. By increasing the interface area between ceria and the nickel material in the anode, the “shielding” effect of the ceria should increase. However, the porosity of the anode should be preserved as much as possible to ensure no significant loss of catalytic sites. Therefore, any material added to the anode should have very small particle size. By using a surface coating, the added ceria can have a disproportionately large effect relative to its total mass. In addition to shielding

catalytic sites, infiltrated surface coatings can improve the cell performance without needing to modify the original SOFC structure. It has been shown that polarization resistance of SOFC anodes can be improved using infiltrated coatings containing GDC at relatively low weight% loadings[62]–[64].

In this study, Ni-GDC based SOFC button cells are evaluated for resistance to sulfur poisoning by testing electrical performance under constant current operating conditions. Cells constructed using modified anodes with increased ceria loading were compared to unmodified cells and were found to have far more stable polarization resistance and thus more stable ASR. Electrochemical performance of each cell was tested, followed by a suite of post-testing characterization including SEM, TEM, XPS, Raman spectroscopy, and EDS. The purpose of this was to search for any microstructural changes in the cell anodes that could be correlated to the cell performance observed during testing. Additionally, the amount of sulfur present after testing would help illuminate the mechanism of interaction with the catalyst and ion conducting materials respectively.

7.2. Experiment Design

7.2.1. SOFC Fabrication

Ni-GDC/GDC/LSCF-GDC button-sized SOFCs were prepared using the tape casting and cell construction methods detailed in Section 5.1. The anodes of cells used in this study contained PMMA-created porosity in addition to any porosity created from NiO

reduction. The reference SOFCs for this study were not modified in any way following their creation (Section 5.1.). The experimental population of SOFCs was prepared identically to the reference group of cells. Following fabrication, the anodes of the experimental SOFCs were infiltrated with GDC precursor solution as described in Subsection 5.1.3. The infiltration process was carried out until a ~3.62 weight% loading was achieved. This treatment resulted in a very fine coating of GDC throughout the interior volume of the anode layer.

7.2.2. Electrochemical Testing

SOFCs were tested using a standardized procedure based on the long-term degradation test design described in Subsection 5.2.2. The test procedure was composed of cycles lasting slightly longer than one hour. In each test cycle, an EIS measurement, a 0.033A/s galvanodynamic scan, and a one hour 0.1A cm^2 galvanostatic measurement were taken. Once the cell reached the operating temperature of 650°C, a baseline test cycle was completed on humidified hydrogen. Following this cycle, a fuel composition of 50:50 H_2:CH_4 (Airgas, 99.99%) with 3% H_2O was used. The chosen concentration of 20ppm H_2S was then added to the fuel stream using a source tank of 2500ppm H_2S balanced in CO_2 (Airgas, +/-2% H_2S content). A reference cell was also testing under only humidified hydrogen so as to provide a “clean” reference for later characterization. The “snapshot” measurements taken every hour during this long term testing provided a direct comparison of the performance and health of the reference and infiltrated SOFCs. Observing the trends in ASR components, OCV, and electrical power output provides information about the specific effects that the fuel exposure has on the SOFC.

7.2.3. Post-Testing Anode Characterization

Following the long term testing of these cells, the anode surface and cross section were examined using SEM and EDS to search for sulfur and/or carbon deposits and to determine if any significant microstructural changes had occurred during the long term testing. XPS was used to investigate differences in the electronic structure of the species present on the surface of the SOFC anodes after long-term testing. The spectra corresponding to nickel, cerium, oxygen, carbon, and sulfur were collected and compared across the clean reference, reference, and infiltrated cells. Raman spectroscopy was performed as a supplementary characterization technique to XPS. Raman spectra provides particle size information in addition to being able to differentiate carbon structures. All Raman spectra were normalized to the 1030-1280cm^{-1} region, corresponding to the NiO band. X-ray diffraction was also performed to determine if exposure to sulfurized methane fuel caused phase changes in any of the anode constituent materials.

7.2.4. Anode Powder Microscopy

In addition to full cell testing, a number of powder samples were prepared for TEM analysis. Sections of fired anode functional layer tape identical to those used in SOFC fabrication were lightly crushed using a mortar and pestle to create a powder. Four powder samples were exposed to sulfurized fuels. Two samples were coated with GDC solution and two served as unmodified controls. One test-control pair was exposed to humidified H_2 and the other to a humidified 50:50 H_2:CH_4 mixture (Airgas, 99.99%). In each case, the gas flow rate was 125sccm. Both streams contained 40ppm H_2S. Each sample was exposed to the fuel stream for 24 hours at

650°C, then cooled in hydrogen (25sccm flow rate). TEM images were taken from a direction tangential to the surface of the AFL particles to capture any deposits of foreign material that could be present following fuel exposure.

7.3. SOFC Performance Results

Figure 25 (a) and (b) show I-V curves of the reference and the infiltrated cells, respectively, as a function of sulfur exposure time. There was a significant difference in the performance of the cells containing the infiltrated GDC as compared to the reference cell once exposed to sulfur. Figure 25 (c) shows the trends in maximum power density of both cells over time, with points corresponding to the peaks in Figure 25 (a) and (b). Both cells displayed a significant drop in power output within five hours of exposure, caused by reversible sulfur adsorption on the anode triple phase boundary sites[59], [65]–[67]. However, while the power loss continued until failure in the reference cell, the infiltrated cell stabilized and experienced no additional power loss for over 290 hours.

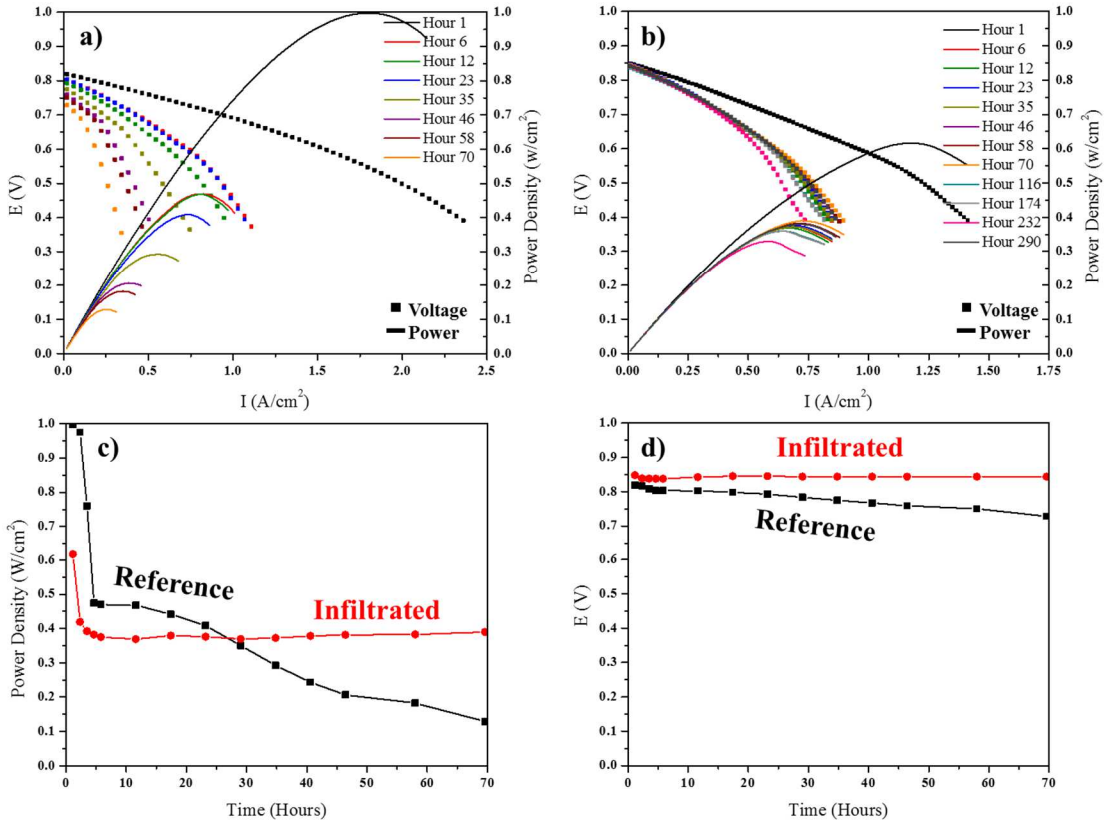

Figure 25: I-V behavior for a) Reference cell b) Infiltrated cell; c) Maximum power trends for reference and infiltrated cell d) Open circuit voltage (OCV) for reference and infiltrated cell

The open circuit voltage of both cells is shown in Figure 25 (d). The reference cell shows a constant decrease in OCV with a slope of 0.1V/100hr. In contrast, the OCV of the infiltrated cell remained very stable throughout the test.

The time dependent changes of impedance spectra of the reference and the infiltrated cell are shown in Figure 26 (a) and (b). A significant increase in the total ASR was observed in all SOFCs within the first three hours of sulfur exposure. The trends in the ohmic and non-ohmic portions of the cell impedance are summarized in Figure 26

(c) and (d). The ohmic portion of ASR was relatively unchanged in both cells for the duration of the testing, as shown in Figure 26 (c).

The growth of the non-ohmic portion of the cell impedance, shown in Figure 26 (d), was largely responsible for the performance loss of the reference cell, which is in agreement with results in the literature[22], [52], [53], [58], [60], and is dominated by the polarization resistance of the anode. The sharp initial increase in the non-ohmic component of the ASR in all cells is likely the result of sulfur occupying catalytic sites and reducing effective TPB length. The longer term degradation observed in the reference cell would then be the result of fouling and chemical degradation of the anode structure from sulfur and carbon.

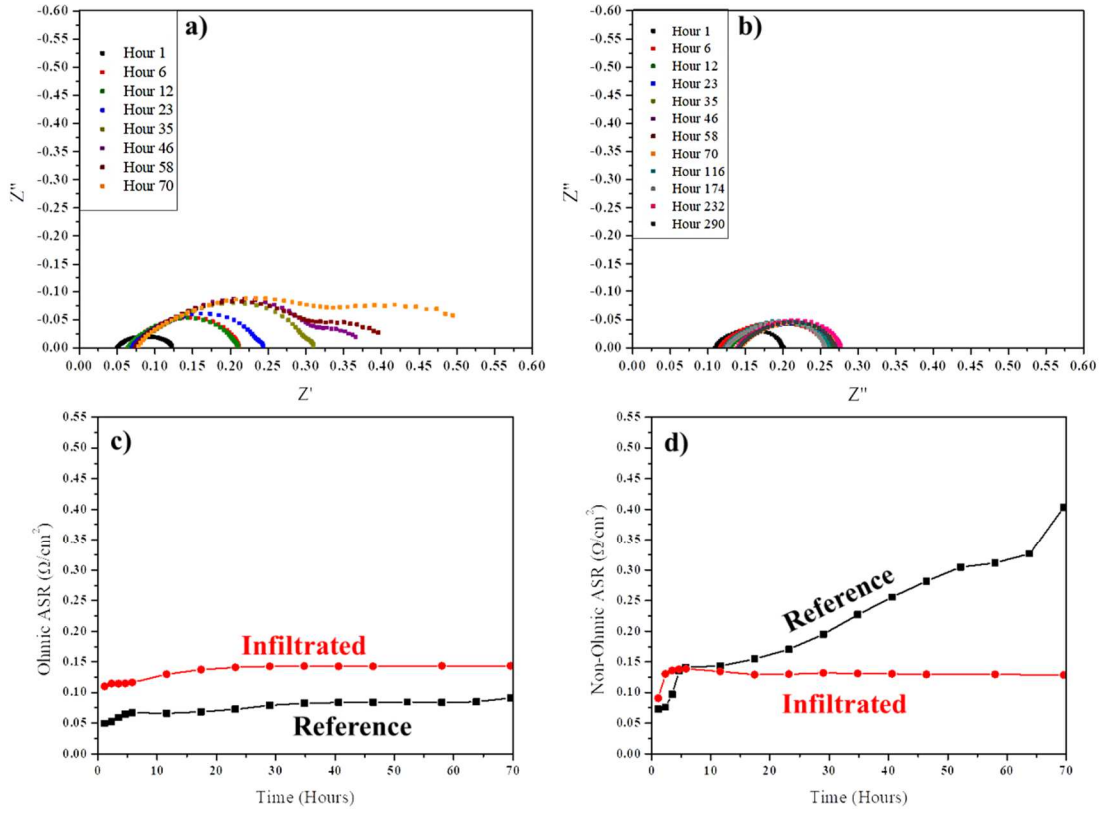

Figure 26: Nyquist plots for a) Reference cell b) Infiltrated cell; c) Ohmic ASR trends for reference and infiltrated cells d) Non-Ohmic ASR trends for reference and infiltrated cells

The degradation effect caused by this structural damage was seen after the first 5 hours in the reference cell and caused an increase of 6.2% hr^{-1} in the non-ohmic ASR. The structure damage degradation phenomenon was not present in the infiltrated cells. The infiltrated cells also displayed an increase in the non-ohmic ASR initially but it then remained virtually unchanged for the duration of the test following this initial change, suggesting that the nanoparticle infiltration strongly inhibits structural damage to the anode from sulfur. This observation supports the hypothesis of increased ceria-nickel contact area helping to remove surface sulfur through SO_2

formation rapidly enough to prevent significant reactions with the anode materials and the resulting ASR increase.

7.4. Degradation Mechanism Investigation

The large divergence measured in long-term performance between the untreated reference cell and the infiltrated cell suggests that significant changes occurred on the anode of the reference cell. A battery of characterization techniques were used to better understand these changes and the positive effects of the infiltration treatment.

7.4.1. SEM and EDS of Tested Anodes

SEM analysis of the anode cross sections showed some notable differences in the microstructure of the various cells, as shown in Figure 27. In the infiltrated anodes, deposited material was observed on the surface of exposed grains seen in Figure 27 (b). These features are GDC deposits from the infiltration and were not present in the reference cell shown in Figure 27 (a).

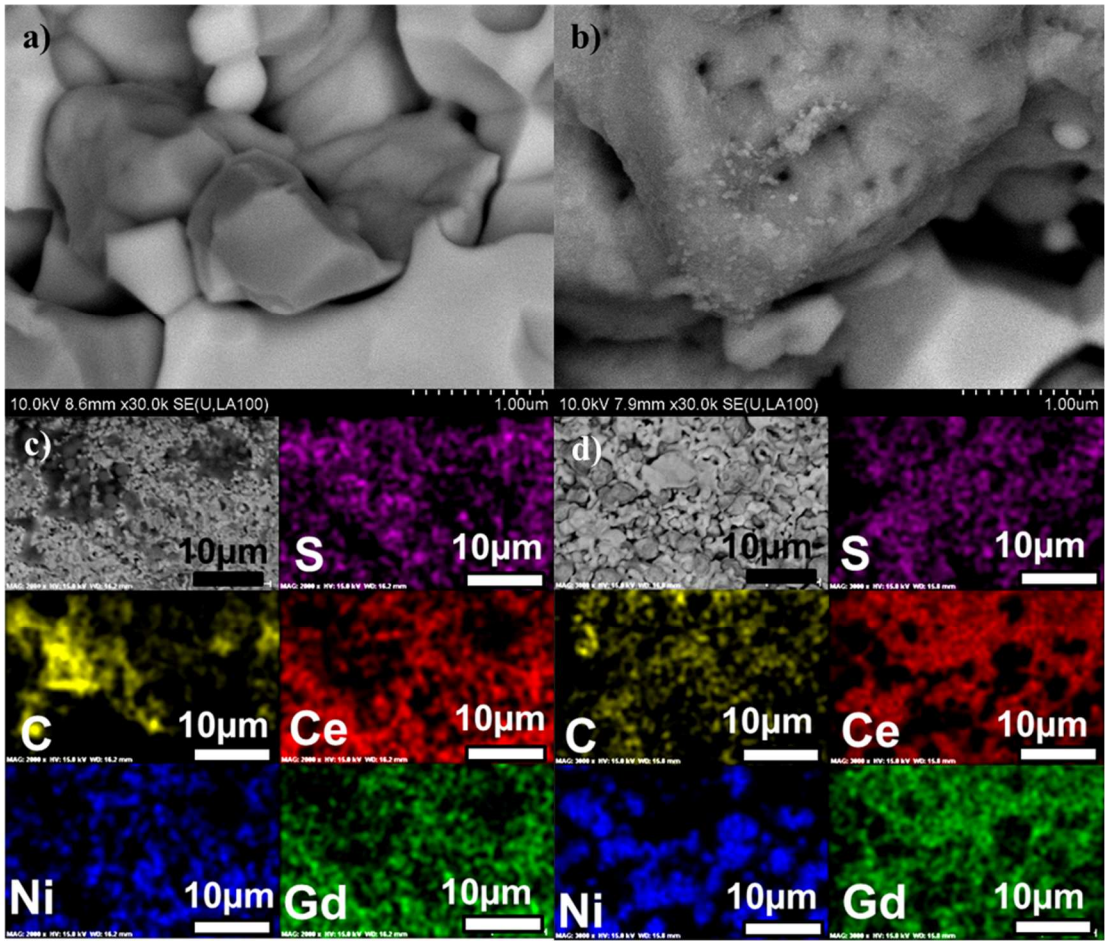

Figure 27: a) Reference cell anode micrograph before testing b) Ceria coating on nickel grain in infiltrated anode c) Micrograph and EDS of reference cell anode after exposure d) Micrograph and EDS of infiltrated anode after exposure

EDS measurements performed on the cross section of the cells after testing, shown in Figure 27 (c) and (d), revealed a large contrast in the amount of carbon present and a small difference in sulfur between the reference and infiltrated cells. This finding indicates that sulfur poisoning of the anode will encourage carbon deposition, whereas the infiltrated anode had very little carbon buildup. The resilience of the

infiltrated anode to carbon deposition is a promising result for the ultimate goal of making IT-SOFCs that are able to operate on commercially available fuels.

7.4.2. Raman Spectra Results

Further investigation into the nature of the contaminant species in the cell anodes was performed using Raman spectroscopy. This technique supplied information concerning the grain size of the anode material at the anode surface and the nature of the carbon deposits present on the degraded reference anode. Figure 28 shows the Raman spectra collected from the infiltrated cell anode, as well as those collected form the two reference cell anodes.

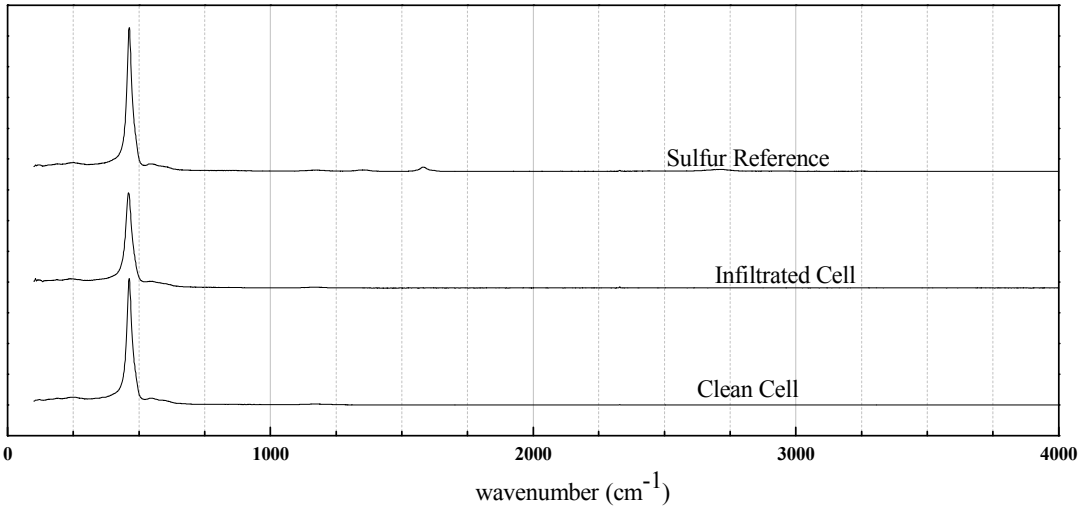

Figure 28: Raman spectra for reference and infiltrated SOFC anodes exposed to sulfur, with spectrum of clean reference cell anode for comparison.

The two wavenumber regions of interest in the spectra from all three samples are 400-550 cm^{-1} and 750-2000 cm^{-1}. No peaks outside of these regions could be resolved out of the background noise. Figure 29 highlights these regions of interest.

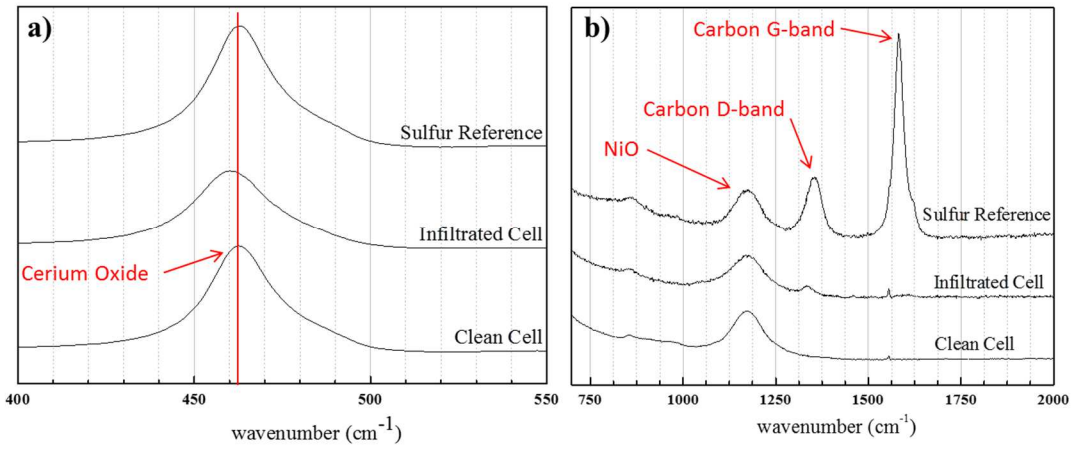

Figure 29: Raman spectra of Reference, Infiltrated and Clean reference cell anodes; a) Shifted ceria peak in infiltrated cell; b) Significant carbon peak growth on unmodified anode

Figure 29 (a) shows the cerium oxide peak of each cell. The slight peak shift and broadening seen in the infiltrated cerium oxide spectra is attributed to the ceria nanoparticles from infiltration[68]. The infiltrated and reference cells showed a stark contrast in the 1250-1750 cm^{-1} wavenumber range, shown in Figure 29 (b). Compared to a clean, unmodified cell exposed only to wet hydrogen, the infiltrated cell and reference cell exposed to sulfurized hydrocarbon fuel gained peaks corresponding to the carbon D-band at 1350 cm^{-1}, and the reference cell exposed to sulfurized fuel gained a large peak corresponding to the carbon G-band at 1580 cm^{-1}[69]. The carbon G-band peak indicates carbon is present in the form of graphite on the anode surface[70], [71]. The carbon D-band seen in the spectra of both the infiltrated and reference cells exposed to sulfurized hydrocarbon fuel is caused by defects and impurities in carbon structures[70]. In addition to these peaks, a small but sharp peak was present in all three samples at 1550 cm^{-1}, though at varying intensity. This peak

is caused by amorphous carbon and is likely partially caused by contamination from handling of the samples.

These findings support the results from EDS measurements showing a significant difference in the carbon present on the anodes of the infiltrated and reference cells. In particular, the high intensity carbon G-band peak (1550 cm^{-1}) in the sulfur-exposed reference cell further confirms that significant solid carbon formation is taking place when the ceria infiltration is not present in the anode.

7.4.3. XPS Results and Analysis

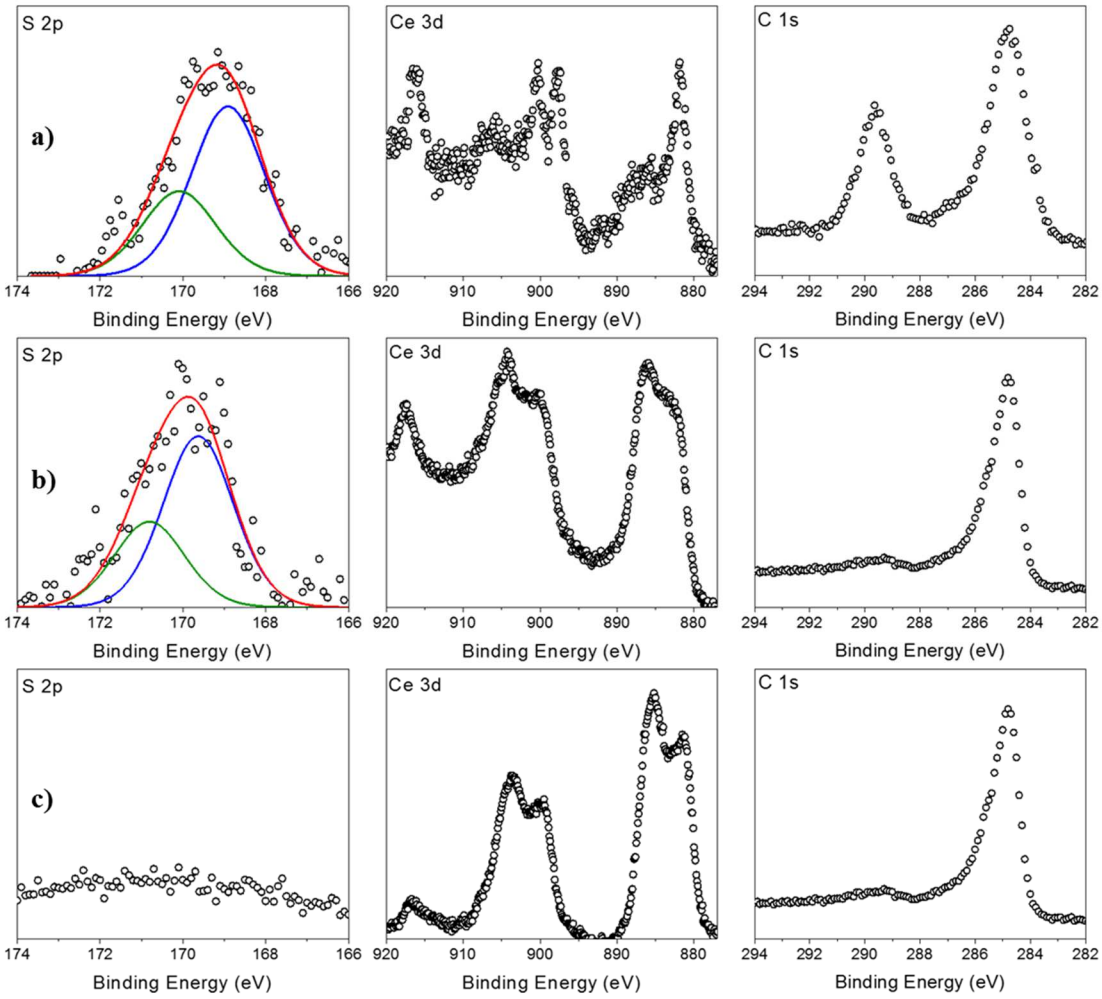

Figure 30: Sulfur, Cerium, and Carbon XPS spectra: a) Reference cell; b) Infiltrated cell; c) Clean Reference Cell

XPS analysis of the same sample set used for Raman spectroscopy provided further insights on the state of the surface of each cell's anode. Figure 30 (a), (b), and (c) show the XPS spectra of S 2p, Ce 3d, and C 1s on the reference, infiltrated, and clean cell, respectively. The clean reference cell contained no sulfur as expected and confirms that any sulfur present in the other cells is not due to sources external to the experiment. In contrast, both sulfur exposed cells with or without surface

modification shows the sulfur signals. Based on the binding energy of that, sulfur is present on the surface in the form of sulfate. Quantitative analysis of sulfur concentration on each cell shows that the sulfur concentration in the infiltrated cell was approximately half of the concentration in the reference.

One of the findings of XPS analysis on the cell anodes was the variation in cerium oxidation state between samples. Cerium 3+ and 4+ have distinct 3d spectra and the prevailing oxidation state of cerium in the sample can be estimated based on the shape of the measured spectra. The cerium in the infiltrated cell was primarily Ce^{3+}, identical to cerium in a cell that had never been exposed to sulfur, as indicated by the peak at binding energy ~886 eV. In contrast, the reference cell that was exposed to sulfur contained more Ce^{4+}, indicated by the strong peak a binding energy ~884 eV[72]. These results suggest that the addition of the ceria coating is preventing the lasting oxidation of the cerium present in the anode surface and is the key for the increase of anode sulfur tolerance.

Another key difference between the XPS measurements of the reference and infiltrated cells was seen in the C 1s spectra. All three samples showed a peak at ~285 eV, but only the reference cell possessed a second peak at ~290 eV. The absence of the carbon 1s peak at binding energy ~290eV on the surface of the infiltrated cell reinforces the Raman spectroscopy and EDS findings that without the nanoparticle coating, sulfur poisoning makes the cell very vulnerable to carbon deposition.

7.4.4. Anode Powder TEM

TEM performed on untreated anode powder exposed to sulfurized methane showed a significant carbon presence on nickel grains, shown in Figure 31 (a).

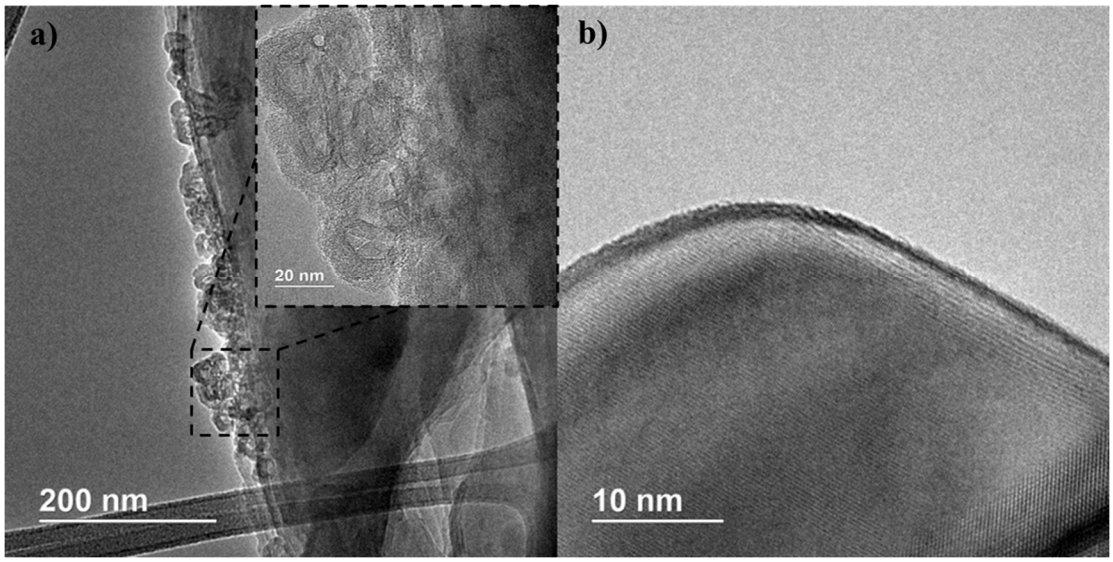

Figure 31: TEM images of a) Carbon growths on nickel grain in untreated anode powder b) Pristine surface of infiltration solution-treated anode powder

The build-up of carbon further supports the findings from XPS and Raman spectroscopy that carbon formation is a major contributor to cell degradation under these conditions. Furthermore, the apparent amorphous nature of the carbon seen in the inset of Figure 31 (a) supports the Raman spectroscopy finding of significant disordered carbon present on the surface of standard cells exposed to sulfurized methane. Anode powder treated with the ceria solution was seen to be carbon free after an identical gas exposure, as shown in Figure 31 (b).

7.4.5. X-Ray Diffraction

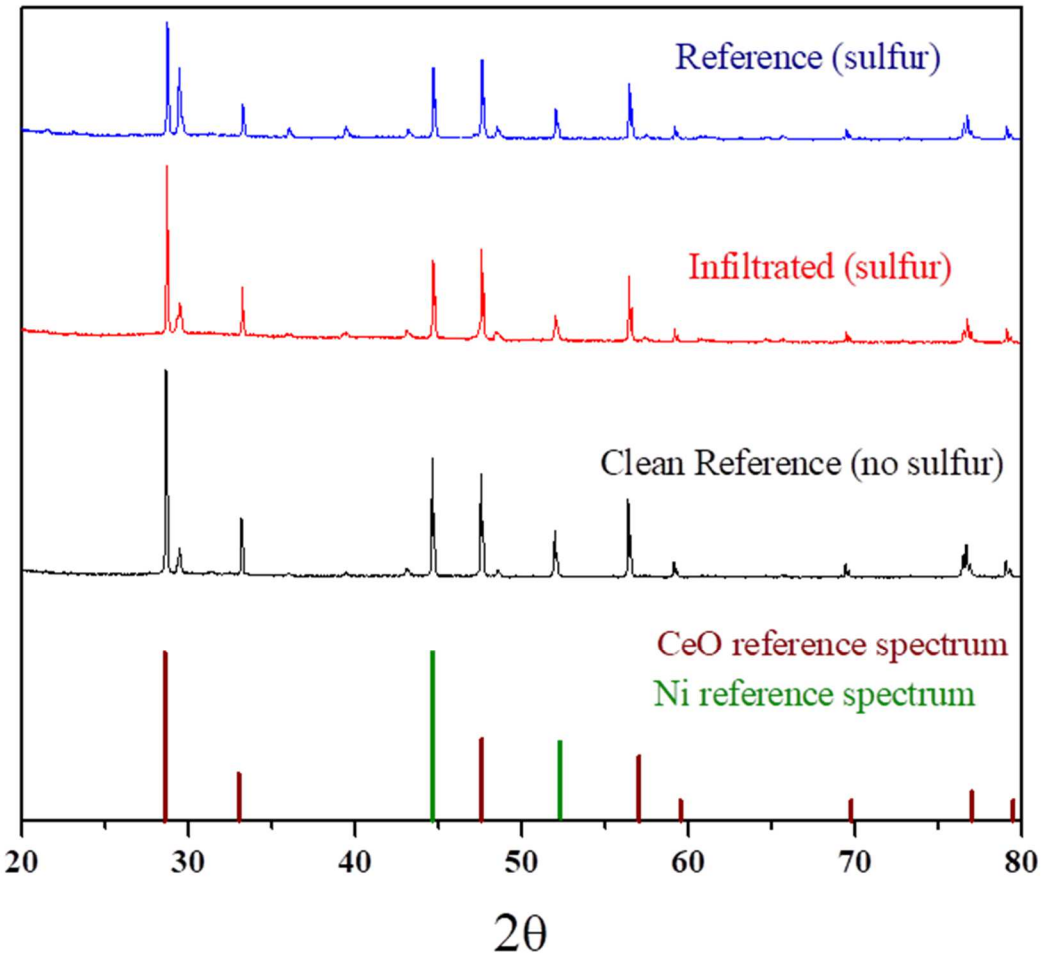

Figure 32: X-ray diffraction patterns for Reference, Infiltrated, and Clean Reference cells with cerium oxide and nickel reference spectra

The X-ray diffraction patterns (Figure 32) of the cells showed very little difference between the various anodes. All but one of the main peaks matches either the cerium oxide or nickel reference spectra. The unaccounted-for peak at $2\theta = 29$ was unchanged between the clean reference and the infiltrated samples, and grew significantly for the sulfur-exposed reference sample. Base on XPS results, this peak can likely be attributed to carbonates. There was also a number of small changes in

relative intensity of some of the nickel and cerium oxide peaks, but no evidence of the formation of a significant secondary phase in any of the samples appeared.

7.4.6. Proposed Mechanism for Improved Sulfur Tolerance

Based on the experimental evidence on the aged cells, the presence of nano-infiltrants, in this case, GDC, plays an important role of surface protection. Figure 33 shows the conceptual schemes for the sulfur protection mechanism proposed.

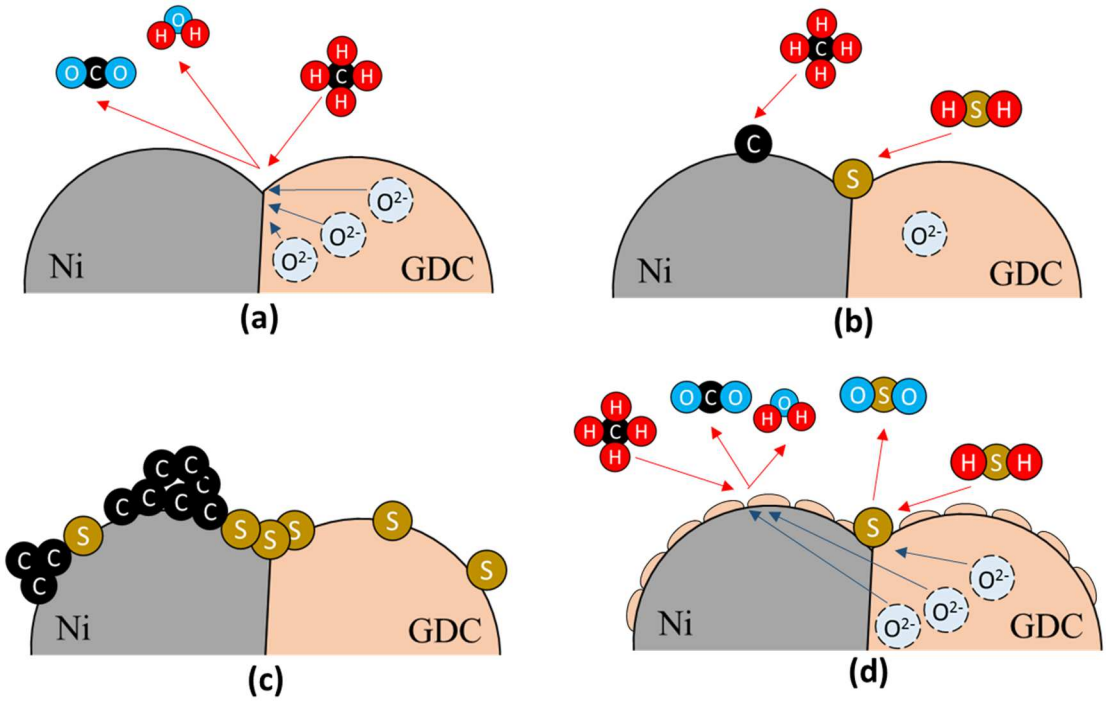

Figure 33: Sulfur protection mechanism concept: a) Normal fuel oxidation reactions at TPB; b) Adsorbed sulfur blocks TPB site, carbon deposition begins; c) Fully deactivated anode with adsorbed sulfur and carbon growths; d) High density of TPB sites and improved oxygen transport from nanoparticles prevents sulfur poisoning effects

The infiltrated GDC increases the density of reaction sites in the anode, mitigating the impact of sulfur adsorption. The high ionic conductivity of nanoparticle GDC allows

a continuous pathway for oxygen to transport to the TPB sites, providing sufficient oxygen to oxidize the surface sulfur intermediates into gaseous SO_2. This constant oxygen flux, pumped from cathode to anode while SOFC operating, is essential for preventing the permanent degradation in anode, caused by carbon growth and damage to the anode structure.

7.5. Conclusions

Infiltrating a small weight% of GDC into porous, Ni-GDC SOFC anodes significantly lessened the degradation caused by sulfur exposure. When exposed to a hydrogen/methane mixture containing 20ppm of hydrogen sulfide, an unmodified SOFC became nonfunctional after 70 hours while the infiltrated SOFC operated stably for over 290 hours. The sulfur-induced increase in polarization resistance associated with anode poisoning was far smaller and did not grow over time in the infiltrated cell. The negative impact of sulfur exposure manifested as two distinct degradation methods. These were identified as adsorption of sulfur on triple phase boundaries, and carbon buildup on the anode surfaces. The infiltration prevented carbon buildup by providing improved oxygen ion transport to the surface which promoted the removal of sulfur and carbon via SO2 and CO2 formation so that the concentration of surface contaminants remained low. This method for increasing the resistance of ceria based SOFCs to damaging fuels is promising for creating more robust devices.

The author would like to acknowledge the support of the Maryland NanoCenter and its AIMLab for the use of the SEM and TEM used in this study. The author would like to additionally acknowledge Dr. Karen Gaskell in the Surface Analysis Center of the UMD Department of Chemistry and Biochemistry for assistance in obtaining XPS and Raman spectroscopy data. Funding for this work was provided by the National Energy Technology Laboratory (contract #4319920).

Chapter 8: Small Scale SOFC Thermal Measurement and Tri-generation of Heat, Power, and Potable Water from Waste

8.1. Study Rationale

There are many areas in the developing world where traditional approaches to utility infrastructure are not feasible due to cost, political instability, or lack of local technical expertise. Contaminated water sources are one of the largest contributing factors to the spread of disease in these countries. Despite efforts from both governments and NGOs, much of the African population does not have access to uncontaminated water[73], [74]. With these conditions, unconventional strategies for providing basic utility access are needed.

A design philosophy based on modular technology is attractive for this application. Decentralized energy production is attracting interest in industrialized nations due to the greater flexibility and security it offers[75], [76]. The same advantages are present in the case of developing nations with the added benefit of rapid deployment and low requirements for capital. Modular technologies can be sized to the demands of the community while still reaping the benefits of standardized components and designs[77], [78]. The risk of large-scale utility outages is also drastically lowered.

Solid oxide fuel cells are a good candidate technology for this application. SOFCs are capable of much higher efficiencies compared to combustion generators and have the advantage of being solid state devices. Multiple significant improvements to SOFCs have been made in the last few years. Most importantly, lower operating

temperatures, higher power densities, and superior chemical durability have been realized[54], [79]–[81]. In a combined heat and power configuration SOFCs can achieve an overall fuel conversion efficiency as high as ~90%[82]. Their efficiency, durability, and fuel flexibility make distributed SOFC systems an attractive choice for deployment in place of traditional centralized power.

This work was undertaken with the purpose of designing a SOFC based system capable of producing electricity and clean water in areas without access to modern utilities. Additionally, the system should use locally produced fuels and be a size such that delivery and installation are not difficult.

In order to create a serviceable model, the performance metrics of representative GDC based SOFCs were determined. The anodes of these cells are more tolerant of hydrocarbon fuels than yttrium stabilized zirconium based SOFCs, allowing for thermal cycling and long term operation with less fuel contaminant induced degradation[53]. The metrics of interest include cell stability and performance under biogas fuel, and the heat production of an operating SOFC.

A method for measuring the heat output of a button-sized SOFC was developed and employed. A number of studies have been carried out in which the thermal behavior of large-scale planar SOFC or SOFC stacks is measured[83]–[85]. In comparison, little to no literature exists concerning thermal energy production of button or “coin” sized SOFCs. The measurement technique developed in this study compensated for difficulties arising from signal-to-noise ratios by creating a system that would slowly

cool over many hours, therefore magnifying the effects of small amounts of heat energy being created by SOFCs.

Using the measured performance of these cells, larger scale SOFC stacks were modeled and used to inform design choices for the proposed multipurpose system. Additionally, quantitative information on the performance of water filtration technology suitable for pairing with the SOFC was collected from literature sources[86]–[89].

While producing electricity, SOFCs produce heat from the exothermic reactions taking place, and water is formed on the anode side of the cell from the fuel oxidation. The waste heat from this process can be captured through a heat exchanger and used to drive membrane distillation of water. Direct contact membrane distillation (DCMD) was chosen for this system due to its robust nature and simplicity. In this method, a hot stream of feed water is passed over a microporous membrane with a cool distillate stream on the opposite side. The differential vapor pressure causes the feed water in the pores to evaporate and condense into the cool stream, leaving contaminants behind.

8.2. Experimental Design

8.2.1. SOFC Electrochemical Evaluation

Button-sized (1in. diameter) Ni-GDC/GDC/LSCF-GDC SOFCs were fabricated using standard tape casting techniques. The cells were operated on hydrogen, methane, and simulated anaerobic digestion (ADG) biogas composed of CH4, CO2, and H2O.

Button cells were heated to 650°C and the anodes exposed to hydrogen for 2 hours to reduce the nickel oxide. Following anode reduction, the cell temperature was lowered to 600°C and the gas stream was switched to the operating fuel; hydrogen (Airgas, 99.99%), methane (99.99%, Airgas), or simulated biogas mix composed of 70% methane 30% carbon dioxide. The hydrogen and methane streams were bubbled through water at room temperature to add 3% hydration to the stream. To closely simulate ADG biogas, the methane-CO_2 mixture was bubbled through water at 45°C to give a moisture content of ~7.5%. The final simulated biogas composition was 64.75% CH_4, 27.75% CO_2, 7.5% H_2O. Electrochemical impedance spectroscopy and galvanodynamic scans were used to characterize the performance of the SOFCs. Area specific resistance, open circuit voltage, and the current dependence of electrical power generation were the metrics of interest.

8.2.2. SOFC Thermal Measurement

The heat production of the operating SOFC button cells was measured by comparing the cooling curves and equilibrium temperatures of the testing furnace over a 10 hours span. To accomplish this, a cell was brought to an initial operating temperature,

and then allowed to cool while the furnace output power was fixed such that cooling would be slow and the cell would not leave an acceptable operating temperature window. The temperature at the SOFC was recorded at 5 second intervals using a K-type thermocouple to create the cooling curve. A reference cooling curve was created with the cell remaining at open circuit conditions which was then compared to the cooling curves measured while the cell was operating at a fixed current. The cell anode was exposed to wet (3% H_2O) hydrogen (Airgas, 99.99%). The cooling data was fitted using Newton's law of cooling.

$$\boldsymbol{T(t) = T_{equilibrium} + \left(T_0 - T_{equilibrium}\right)e^{-kt}} \qquad \textbf{(10)}$$

The resulting functions were integrated to find the area under the curves which is directly proportional to the heat produced by the cell. The curves measured for a number of current values were used to establish a relationship between SOFC current and heat production. This experiment was repeated using both methane (3% H_2O) and the simulated biogas mixture. In order to calculate the quantitative amount of heat produced by cells, two more reference cooling curves were measured with first a 0.092 Watt, then a 0.052 Watt heating coil taking the place of the SOFC. These power values were chosen for their proximity to the expected heat production from the button-sized SOFCs. The cooling behavior of the heating coil experimental runs was used to correlate cooling trends with thermal power generated at the cell location.

Following test on smaller cells, the heat production of a large format (8cm x 8cm active area) planar cell was measured to further inform system calculations. These cells were sourced and operated by Redox Power Systems, LLC. The large-format

cells were operated on lab air and pure hydrogen. An in-line sensor was used to monitor the output power of the testing furnace at a fixed temperature. Integrating the measured power over the measurement window yielded the cumulative power consumption. By comparing the total power required to maintain temperature while the cell was at open circuit to the total power during cell operation at $2Acm^{-2}$, the heat production of the cell was calculated. The power required while operating at $2Acm^{-2}$ was compared to the predicted value from the model. Origin data analysis software was used for integration and fitting of measured data.

The results of the SOFC heat production experiments were used to model the outputs of a larger scale SOFC system. The electrochemical performance and heat production at different operating currents were calculated and used to create operating profiles showing the electrical power, thermal power, and water outputs of the proposed system.

8.2.3. System Model Development

The results of the SOFC heat production experiments were used to model the outputs of a larger scale SOFC system. The electrical power output and heat production at different operating currents were calculated and used to create a series of operating profiles showing the expected fuel consumption, electrical power, and thermal energy. The calculated SOFC system heat and water outputs were combined with a direct contact membrane distillation (DCMD) unit of a chosen size to determine the amount of clean water that could be distilled using the SOFC heat.

8.3. SOFC Electrical and Thermal Power Measurement

8.3.1. SOFC Button Cell Performance

SOFC button cells fueled on hydrogen, methane, and methane-carbon dioxide mixtures showed reasonable electrochemical performance in terms of area specific resistance and current-voltage behavior.

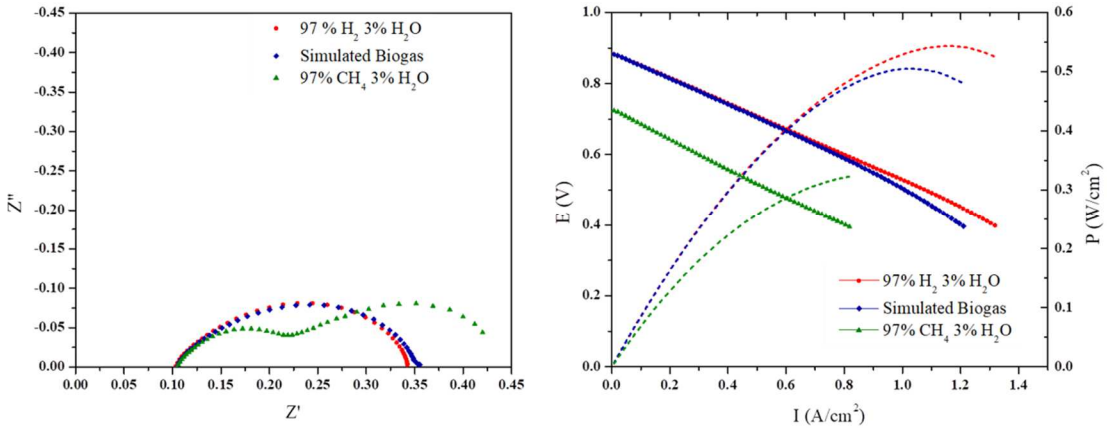

Figure 34: a) Nyquist plots and b) current-voltage behavior of SOFCs using H2, simulated biogas, and methane (T=600C)

Figure 34(a) shows the EIS spectra for a SOFC button cell with different fuels. The ohmic ASR of the cell remains unchanged across the different fuel conditions. However, there are significant effects on the non-ohmic portions of the spectra. The hydrogen and simulated biogas conditions show very little difference, with only a small increase in the low frequency region corresponding to anode polarization resistance for the biogas. The methane fuel with low water content displayed significant difference from the other cases. A second distinct arc is observed whereas this was not the case for the other fuel cases. The total impedance was also 24.6% greater compared to the hydrogen case. The higher ASR and distinct arc shape for

low-moisture methane is caused by coking of the anode that occurs when there is insufficient moisture for steam reforming to occur at the cell. The effects of the higher ASR are seen in the I-V behavior of the cell seen in Figure 34(b). In addition to the lower initial slope of the power curve (dashed line) for the low-moisture methane, a significantly lower open circuit voltage was measured.

These deleterious effects were not observed in the simulated biogas case. OCV was not negatively impacted by the carbon containing fuel species and the slope of the power curve was unaffected at lower current densities. The very slight increase in ASR resulted in marginally lower maximum power. The more than two-fold increase in moisture content of ADG biogas compared to the 3% moisture in the other two fuel streams promotes internal steam reforming and thus prevents any significant coking of the anode. This suggests that the natural water content of ADG biogas may be sufficient for acceptable SOFC operation without the injection of steam to the fuel stream. The almost identical OCV and ASR between hydrogen and simulated biogas further supports that water gas shift reactions are occurring in the simulated biogas at the cell, thereby creating a hydrogen rich environment.

8.3.2. SOFC Button Cell Heat Production

The heating coils placed in the cell testing furnace to provide reference cooling curves behaved as expected. The higher power heating coil caused the test furnace to plateau at a measurably higher temperature then the less powerful coil. Figure 35 shows the two cooling curves with heat inputs of 0.092W and 0.052W respectively.

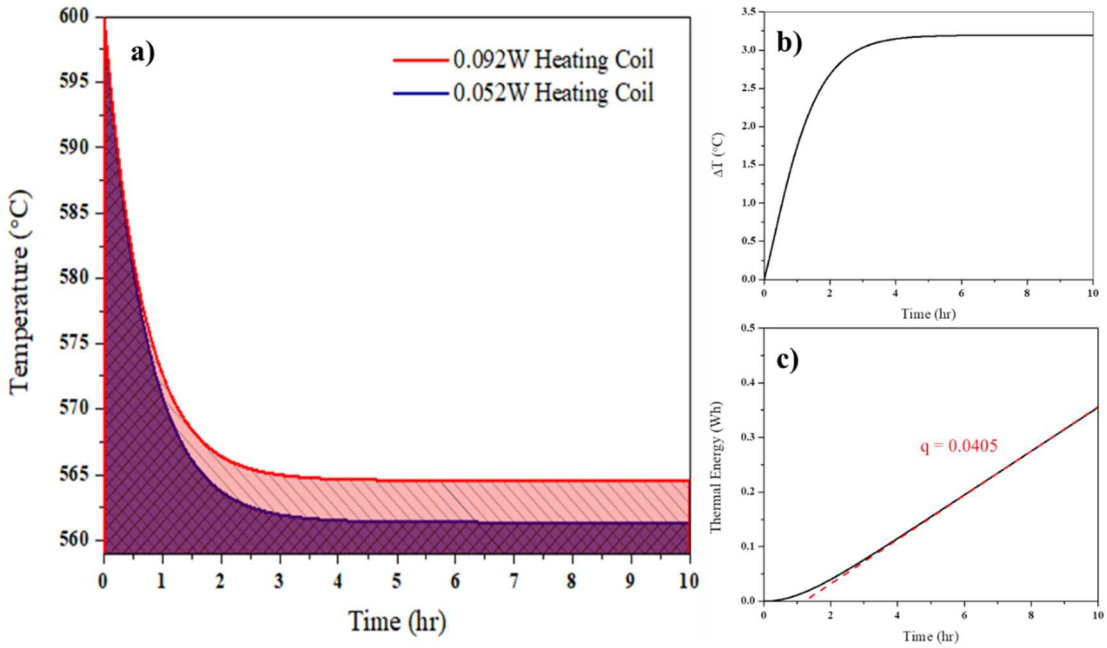

Figure 35: a) Fixed heat-input cooling reference curves for SOFC test system; b) ΔT for 0.092W - 0.052W cooling curves; c) Integrated ΔT with fitted thermal power

Figure 35(b) shows the magnitude of the difference between the two curves in (a). Integrating the two curves yields the area between them in the units of °C·h. By dividing the difference in heat energy (W·h) by the area between curves, a relationship between heat power and measured temperature was determined and

corresponds to the slope in Figure 35(c). This effective heat capacity of the system was used to calculate the heat produced from small-scale SOFC operation.

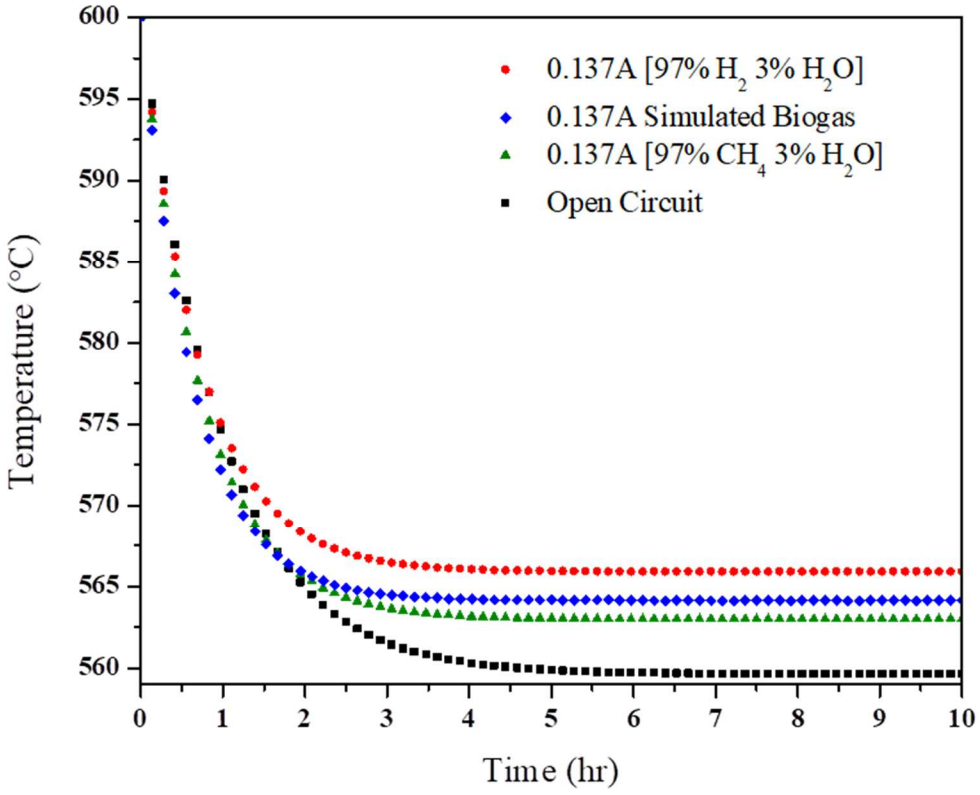

Figure 36: Measured cooling curves for SOFC test system with different fuel compositions

Figure 36 shows the difference in cooling curves between SOFCs operating on hydrogen, methane, or simulated biogas. The cell cooled most slowly while operating on hydrogen, followed by simulated biogas, with low-moisture methane operation leading to the most cooling before equilibrium was reached. This is in line with the expected heat of reaction for the various reactions in each case. The Δh_{rxn} of water formation is $-246.89\ kJ\ mol^{-1}$ at 600°C while the net Δh_{rxn} for the steam reforming of methane and oxidation of the resulting CO and H_2 is $-200.01\ kJ\ mol^{-1}$. These values

are calculated from the molar ratios of the water gas shift reaction and the reaction enthalpies of the subsequent oxidation of carbon monoxide and hydrogen[90].

$$CH_4 + H_2O \rightarrow CO + 3H_2 \quad \Delta h_{rxn} = 192.22 + 0.0541T - (2.06 * 10^{-5}T^2) \quad \textbf{(11)}$$

$$CO + \frac{1}{2}O_2 \rightarrow CO_2 \quad \Delta h_{rxn} = -238.838 - 0.00137T + (2.50 * 10^{-6}T^2) \quad \textbf{(12)}$$

$$\boldsymbol{H_2 + \frac{1}{2}O_2 \rightarrow H_2O \quad \Delta h_{rxn} = -238.376 - 0.0124T + (3.04 * 10^{-6}T^2)} \quad \textbf{(13)}$$

The sum of these reaction energies, with the appropriate molar ratios, yields the overall heat of reaction. If some portion of the methane undergoes dry reforming due to a lack of steam, the exothermicity of the overall reaction will decrease as more energy is required to reform the methane.

Heat measurements were taken at a higher current for a cell fueled by simulated biogas to provide more information on the thermal energy production capabilities of biogas-fueled SOFC systems. Figure 4 shows the measured cooling curves of the test system while utilizing simulated biogas at different SOFC currents.

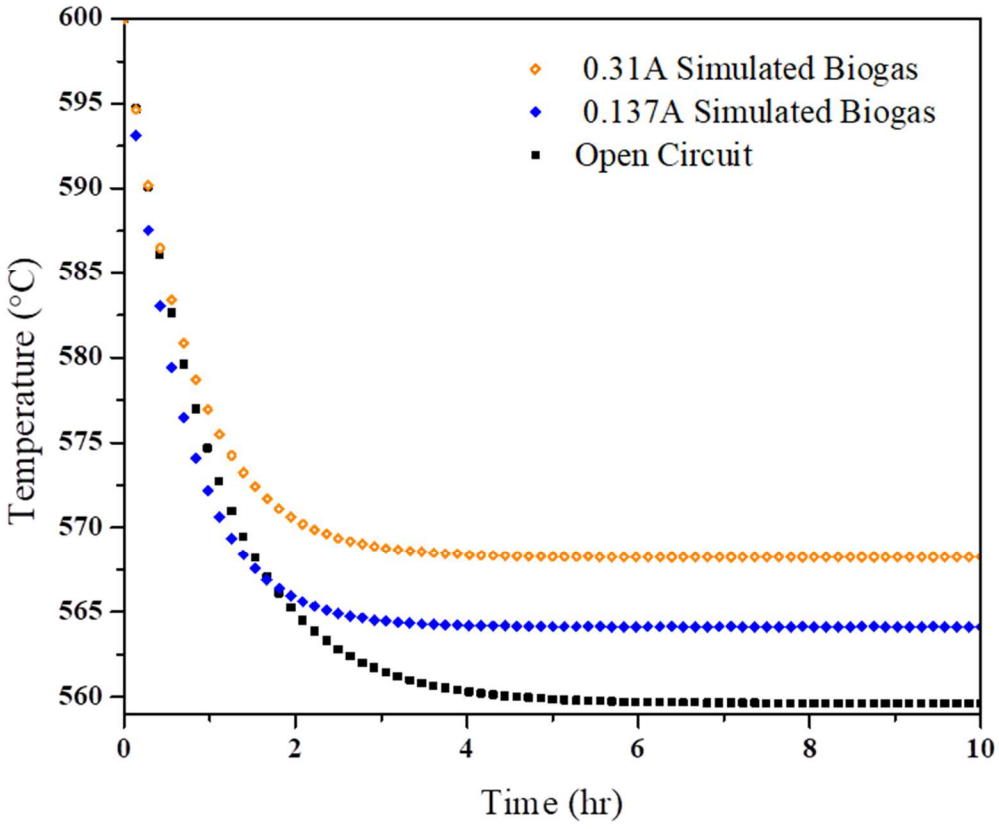

Figure 37: SOFC test system cooling behavior utilizing simulated biogas fuel at different OCV, 0.137A, and 0.31A

The 0.31A used for the higher current test corresponds to 1 Acm^2 current density. The measured cooling behavior shows increased current leading to an increased equilibrium temperature when the same fuel is used. Figure 38 shows the divergence

form the reference OCV curve by each of the test conditions shown in Figure 36 & Figure 37.

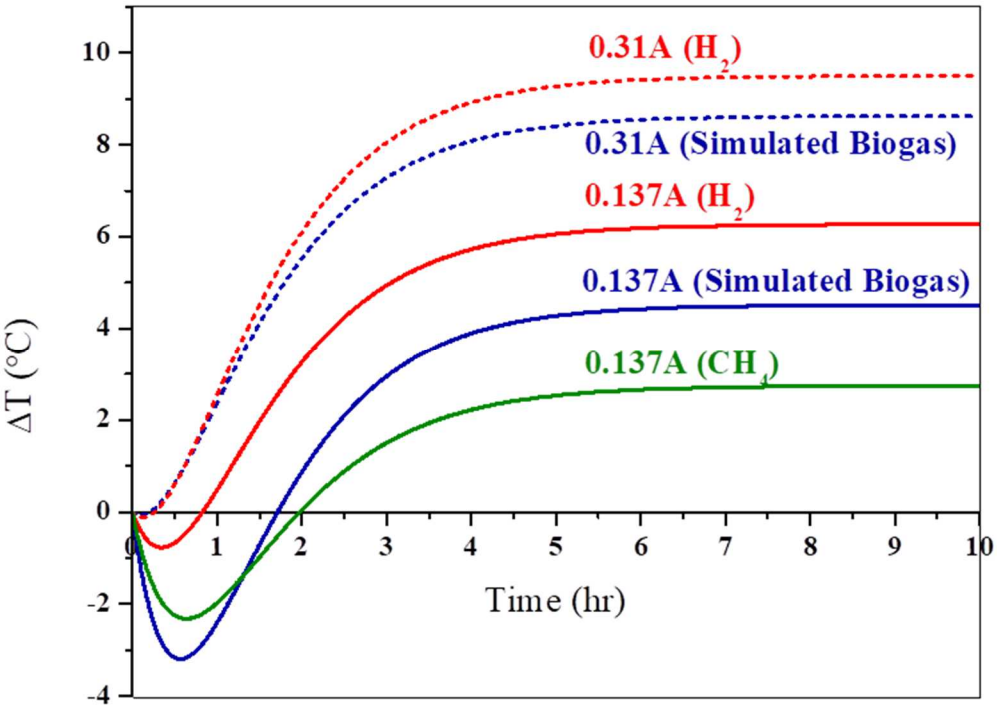

Figure 38: Temperature divergence from OCV cooling over time using H_2, CH_4, and Simulated Biogas at multiple currents

In each case, the operating cells cooled more quickly than the OCV reference for a short period at the beginning of the test. This effect is tiny for both measurements at the higher cell current (0.31A), but was quite apparent for the lower current (0.137A) tests. In the lower current tests, the length of time before the ΔT became positive correlates to the relative exothermicity of the fuel reaction. This suggests an endothermic process is occurring for a short time when the cell first begins to operate, but stops relatively quickly. This effect may be caused by oxidation of reduced CeO_{2-}

$_{\delta}$ in the SOFC anode that occurs when oxygen ions begin to pass through the device once the circuit is closed.

Using the results from the reference experiments shown in Figure 35, the heat production of the button-sized SOFCs was calculated from the cooling behavior under the various fuel and operating current conditions. These results are summarized in Figure 39.

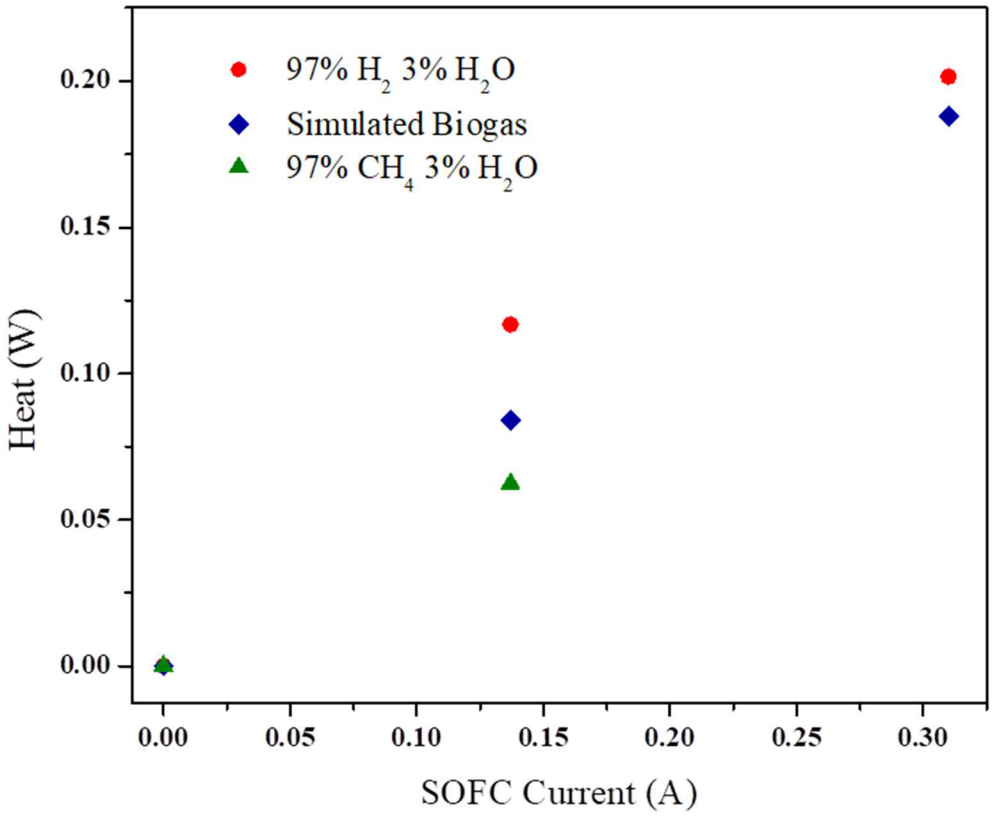

Figure 39: Summarized SOFC button cell heat generation across multiple fuels and operating currents

The trend of greater heat production at higher operating current bore out for both the hydrogen and simulated biogas fuels. The simulated biogas showed an almost

perfectly linear increase in heat with current, which is in agreement with results found in literature[83].

Cells tested at 0.31A in the 97% CH_4 3% H_2O fuel composition did not exhibit sufficiently stable electrochemical performance for the time required for the cooling measurement, so heat production data could not be gathered. This instability was likely due to solid carbon deposition on the anode (coking) caused by insufficient water content for internal reforming.

This technique for measuring the heat produced by small-scale SOFCs is a less complex method for testing the capability of these devices to generate thermal power in addition to electrical power, compared to the testing of large-scale cells or multi-cell stacks. Button-sized SOFCs are relatively simple to test and require many fewer resources in the form of electrical testing equipment and gas transport infrastructure in comparison to larger cells. This allows for many different test conditions to be explored and more informed choices can be made for which fuel compositions are worth testing in larger-scale systems.

8.3.3. Full-Scale SOFC Heat Production Measurement

The power used to maintain the SOFC operating temperature of 650°C in a furnace containing a full-scale planar cell is shown in Figure 40.

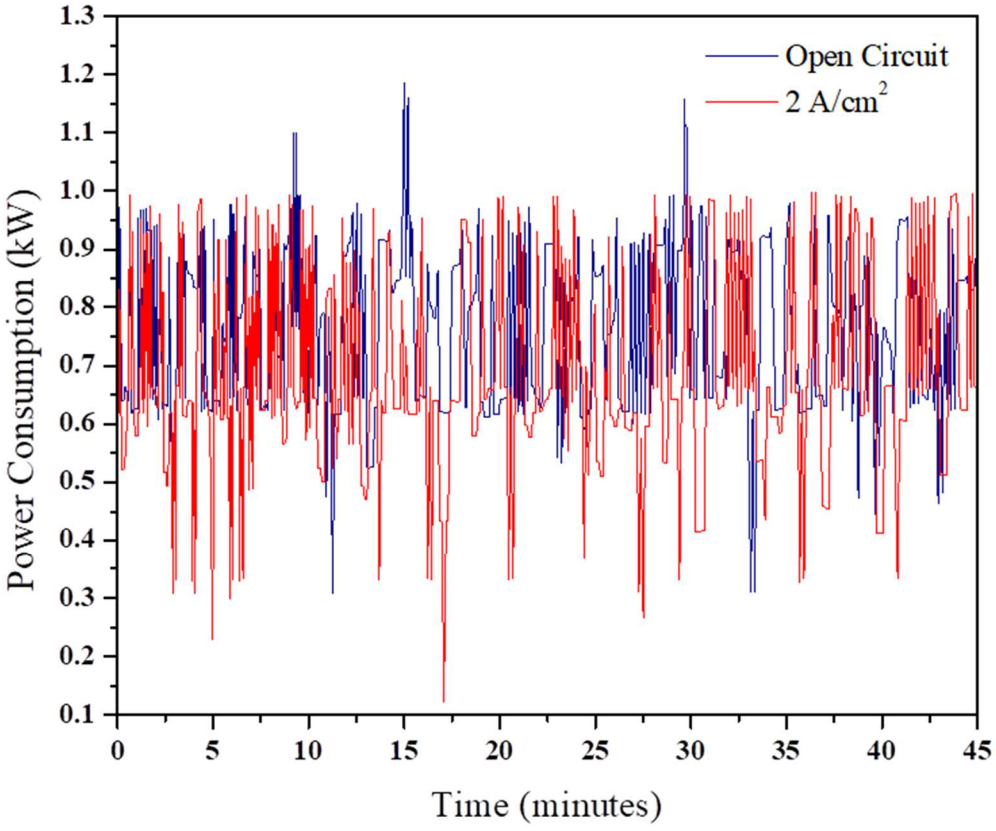

Figure 40: Full-scale SOFC test furnace power consumption at cell OCV and 2 Acm^{-2}

The fluctuation in Figure 40 is due to the duty cycle of the furnace and the sampling interval of the power meter. However, by integrating the measured power with respect to measurement time, the total power was extracted and is shown in Figure 41.

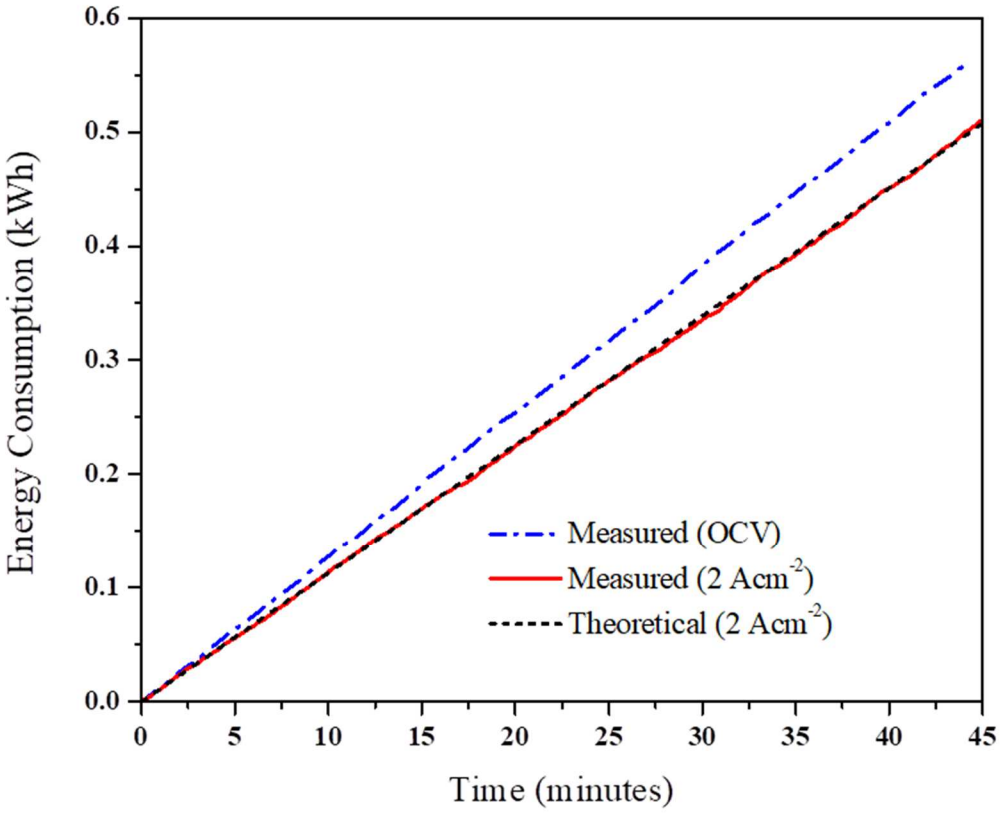

Figure 41: Total furnace energy consumption over time for cell at OCV and 2 Acm^{-2} with 2 Acm^{-2} theoretical prediction

The predicted total power usage for operation at 2 Acm^{-2}, calculated from the hydrogen oxidation reaction enthalpy and resistive heating, is shown as the black dashed line in Figure 41 and is in very close agreement with the measured data for that current density. The high accuracy of the predicted heat production of a full-scale SOFC, combined with the results from the button cell results shows that scaling this calculation to a multi-stack system with appropriate insulation should yield useful information.

8.4. Tri-Generation System Design

Using the experimental findings and results from button cells and full scale SOFC measurements, a SOFC based system suitable for deployment in regions lacking good access to utilities was designed. The design approach chosen was to look at each product of an operating SOFC stack and attempt to leverage it for the production of electricity, clean water, or some other useful resource.

8.4.1. System Components

Methane produced from small-scale anaerobic digesters was chosen as a fuel source. These digesters are low-cost and constructed using easily available materials such as high density polyethylene bags or barrels, and steel piping. Small scale digesters can produce up to 500 liters of fuel per cubic meter of digester volume[91].

Taking in fuel from connected digesters, the SOFC stacks generate heat and electricity. Much of the heat is captured in exhaust gasses or a secondary medium and carried into a heat exchanger. This heat is used to warm a stream of feed water from a local water source such as a river or well. The hot feed water is passed over the DCMD membrane while colder, clean water is flowing on the opposite side. The temperature gradient drives evaporation and condensation through the pores, increasing the volume of clean water. The excess clean water can be siphoned off and combined with the exhaust water from the SOFC system to fill a cistern. The overall process flow diagram is shown in Figure 42. Using this design, an intitial charge of clean water must be placed in the distillate side of the DCMD unit. This design requires air, ADG biogas, and a supply of feed water. Using these inputs, the system

yields electricity, exhaust gasses (primarily CO_2), heated waste water, and clean distilled water.

8.4.2. Process Flow Diagram

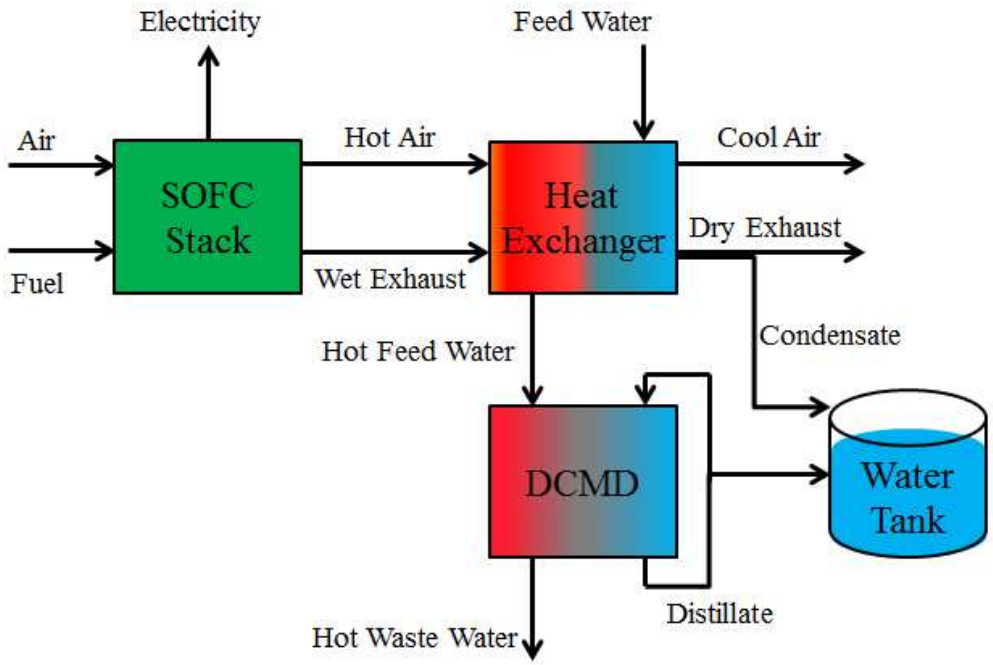

Figure 42: Process flow diagram for proposed SOFC tri-generation system

8.4.3. System Model Results

To model the operation of this system, the performance of cells tested on simulated biogas was combined with calculations for water production, heat production results, and DCMD operating parameters from literature. The modeled system was comprised of 10 stacks of 10 cells each, for a total of 100 cells, with each cell having a 64 cm^2 active area, corresponding to a nominal 10 kW SOFC system. This number of cells was chosen as a system size that could be transported without heavy machinery. At a

given electrical current, the electrical power was calculated from the current density-voltage behavior in Figure 34 (b). Reserving 1 kW of thermal power as the energy required to keep the SOFC stacks in the desired operating temperature window, the measured heat produced by SOFC operation on biogas was used to determine usable thermal power output. The key equations used for calculating system outputs are as follows:

SOFC Stack:

$$q_{SOFC} = q_{rxn} + q_{Joule} - \left(C_{fuel} m_{fuel} (T_{SOFC} - T_{ADG})\right) - \left(C_{air} m_{air} (T_{SOFC} - T_{ambient})\right) - 1000W \quad (14)$$

$$Water_{SOFC} = \left(\frac{I}{2}\right)\left(\frac{6.28 \cdot 10^{18}}{6.023 \cdot 10^{23}}\right)\left(1 - \chi_{C_{fuel}}\right) (18) \quad (15)$$

Heat Exchanger:

$$q_{heat\ exchanger} = q_{SOFC} + \left((C_{exhaust})(m_{exhaust})(T_{SOFC} - T_{outlet})\right) + \left((C_{air})(m_{air})(T_{SOFC} - T_{outlet})\right) - \left((C_{water})(m_{water})(T_{outlet} - T_{ambient})\right) \quad (16)$$

$$m_{water} = \frac{(\eta_{heat\ exchanger})(q_{heat\ exchanger})}{C_{water}} \quad (17)$$

DCMD:

$$Distilled\ water\ mass = (\eta_{DCMD})(m_{water}) \quad (18)$$

The operating current in the model was varied, and the resulting electrical power and thermal power are shown in Figure 43.

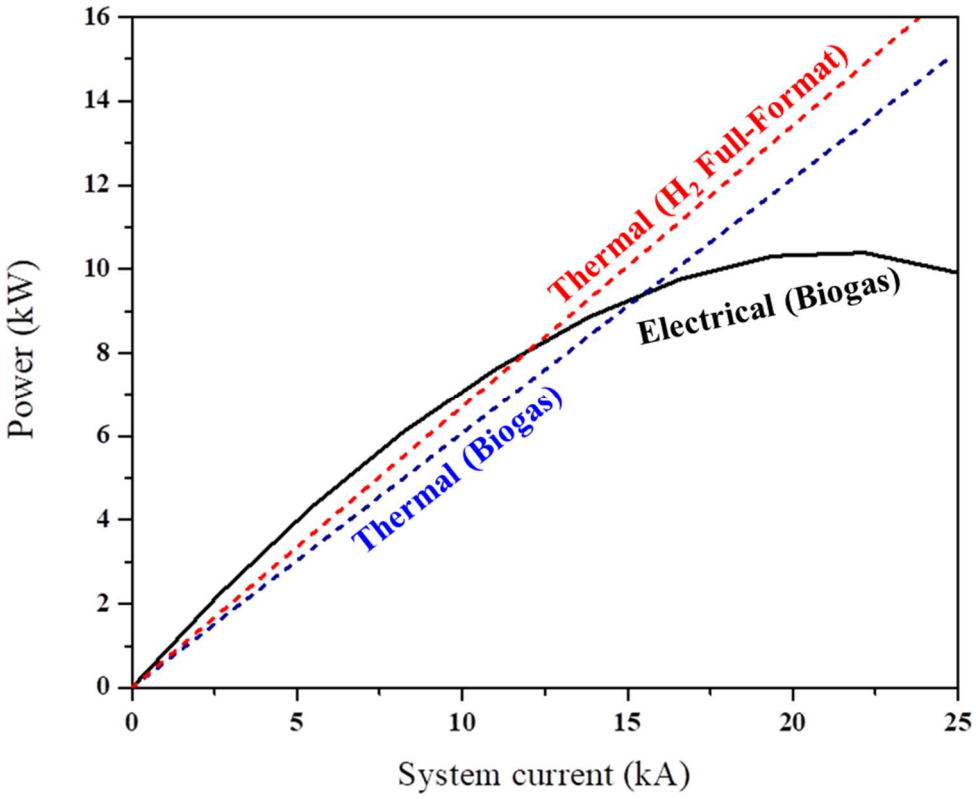

Figure 43: Proposed tri-generation SOFC system electrical and thermal power profiles using measured SOFC thermal measurements for hydrogen and simulated biogas

At lower system currents, the ratio of electrical to thermal power is much greater and less fuel is consumed. This is the preferred operation region for efficient electrical generation. However, at high currents the electrical efficiency decreases and more thermal power is produced along with greater fuel consumption.

The fuel for this system can be provided by on site anaerobic digesters. The fuel consumption of the system scales directly with operating current. This volume of fuel can be provided by digesters with a total volume of 56 cubic meters[91].

With the system electric and thermal power data we then determined the system water production as a function of current using the process flow diagram in Figure 42. Figure 44 shows the relationship between electricity production and clean water production assuming 100% of usable heat output goes to distillation.

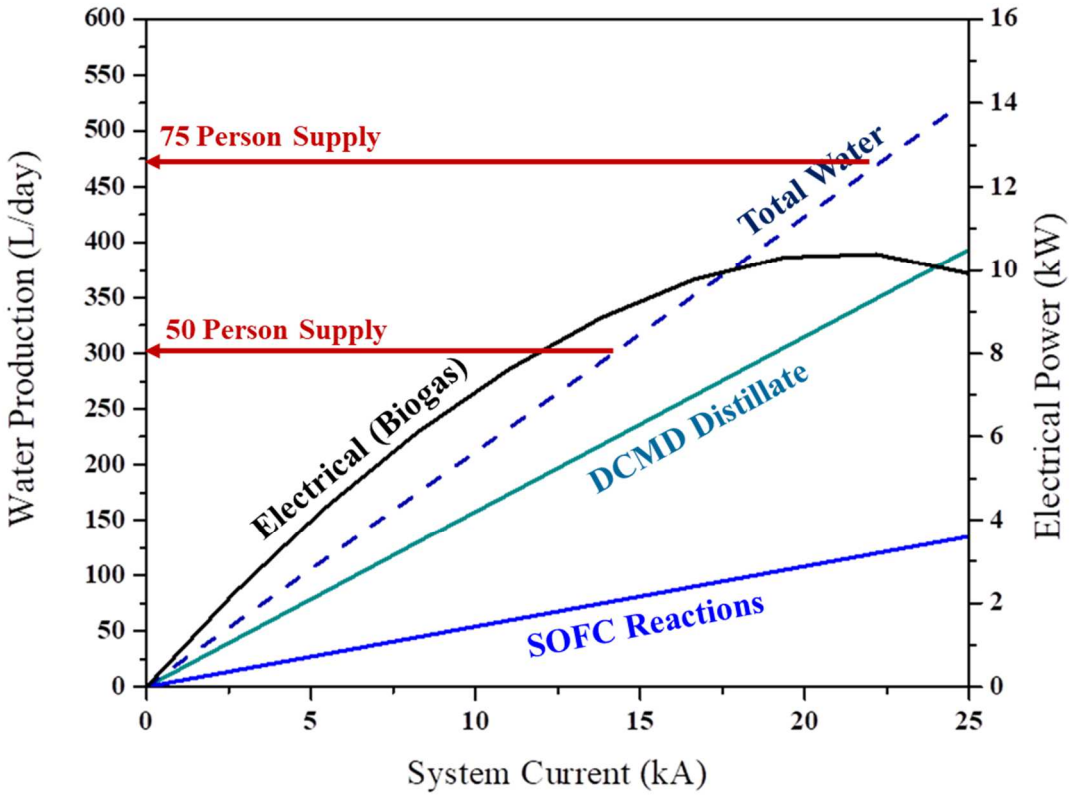

Figure 44: Clean water production totals for the SOFC stack, DCMD unit, and full system, with electrical power generation profile. Water usage benchmarks for 50 and 75 person communities in developing nations are indicated

The water production of the system has two components: the water produced in the anode exhaust by direct SOFC fuel conversion; and the water produced by the DCMD unit using the SOFC-produced thermal power. The water produced directly from hydrogen oxidation in the SOFC unit is linearly dependent on the electrical current as one oxygen ion arrives at the anode for every two electrons in the external

circuit. The SOFC system produces 5.41 L/day per kA of current. The production of clean water from the DCMD unit in this design is dependent on the amount of heat available to create the temperature gradient across the membrane. The unit produces no water at very low system currents because some amount of heat energy must be used to maintain the temperature of the SOFC unit. For these calculations, 1 kW was used for maintaining this core temperature of 600°C. The water produced from a DCMD system depends on membrane area, temperature gradient, and conversion efficiency[86]. Table 1 lists the metrics used for the design of the proposed unit. Once sufficient excess heat is produced to activate the distillation unit, it produces 29.73 L/day per kA of current in the SOFC unit.

Table 1: Proposed DCMD unit specifications

Membrane Area (m^2)	ΔT Across Membrane (°C)	Conversion Efficiency (%)
2.19	**65**	**9**

This proposed system could provide daily drinking water for a 50 person community while operating at less than 50% of its maximum current. By increasing current to 15 kA, the same population can be provided with water for drinking and cooking. While producing water, the system can supply enough electricity for over 100 people based on per capita use in some Sub-Saharan nations[92].

The size of this modeled system was chosen for ease of transport, but there are no strict limits on the size of such a system. Direct contact membrane distillation is also a very scalable technology due to its dependence on membrane area and available

heat. If the deployment area can support a sufficient number of anaerobic digesters, any number of SOFC stacks can be added to increase water and electricity production.

8.5. Conclusions

In addition to electricity production, SOFCs generate heat and water. A method for measuring the heat produced by small-scale SOFCs was developed and used to evaluate the performance of SOFCs operating on a simulated biogas fuel composition. SOFC performance metrics were used to propose a modular system for the on-site production of utilities by integrating anaerobic digesters, SOFC stacks, and direct contact membrane distillation units. A system centered on a 10 kW SOFC generator would be capable of being transported without heavy machinery and could produce clean water and electricity for more than 50 individuals. This system could operate well in areas in the developing world where clean water access and electricity are difficult to obtain but agricultural waste is plentiful. By focusing utility development on local, distributed generation many of the vulnerabilities and drawbacks of a centralized utility provider. Solid oxide fuel cells are particularly well suited to this role.

The author wishes to thank The Electrochemical Society for funding this study and Redox Power Systems for assistance with large-scale SOFC heat production measurements.

Chapter 9: Summary

In this work, efforts were made to determine device characteristics that have a significant effect on the deployment of anode-supported, gadolinium doped ceria (GDC)-based solid oxide fuel cells (SOFCs) as a practical technology. These efforts involved the design and construction of a system capable of testing the mechanical strength of technical ceramics at elevated temperatures and in variable atmospheric composition, the long-term evaluation of SOFC electrochemical stability and performance while operating on sulfur-contaminated fuels, and the development of a technique for measuring the thermal power production of small-scale SOFCs that is less resource intensive than previous SOFC thermal measurement methods. The primary goal of these investigations was to better understand the mechanical strength, chemical resilience, and heat generation capabilities of these devices, and to then intelligently improve or leverage these attributes in order to advance SOFC technology toward commercial use.

To accurately characterize the mechanical strength of SOFC materials and the mechanical properties of the devices themselves, simply testing the materials at ambient conditions is insufficient. Mechanical properties of materials change depending on both the temperature and chemical makeup of the surrounding medium. SOFCs operate at elevated temperatures and in contact with reducing gas environments, therefore these conditions must be applied to mechanical tests to fully investigate SOFC mechanical properties. An alumina three-point bend test fixture

was machined and integrated with a purpose-built atmosphere chamber and temperature control system. Variable temperature mechanical testing of porous ceria bars showed a strong dependence between pore geometry and strength, with spherical porosity leading to higher strength. Both SOFC coupons and pressed ceria bars displayed greater strength at higher temperatures. There was no statistical difference in strength between anode support layers and half-cells composed of anode support and electrolyte at a given temperature in air. Half-cells in which NiO was reduced to Ni by exposure to H_2 at 650°C displayed significant differences in strength when the electrolyte layer was subjected to compressive stress as opposed to tensile stress. Placing the ceramic electrolyte in compression and the metal-ceramic composite anode in tension resulted in the highest strength.

Poisoning of SOFC anodes is a persistent problem stemming from the use of inexpensive nickel catalyst in cells, in combination with the sulfur content in most commercially available hydrocarbon fuels. Increasing SOFC tolerance to sulfur is a more practical solution than completely scrubbing sulfur from all fuel streams. Standard GDC-based SOFCs were operated on mixtures of methane and hydrogen containing 20ppm of hydrogen sulfide to determine the rate and nature of damage caused by the sulfur concentration found in some natural gas sources. Other SOFCs were modified by infiltrating small amounts of GDC in to the anode, creating a fine GDC coating throughout the interior of the layer. These cells operated stably for hundreds of hours, in contrast to the deactivation experienced by unmodified cells within 70 hours. Post-testing analysis of unmodified and infiltrated anodes using SEM, EDS, XPS, XRD, and Raman spectroscopy revealed that the initial catalytic

deactivation caused by sulfur in the unmodified anode lead to a significant secondary coking effect. This was not observed in the infiltrated anode, due to the large increase in reaction site density created by the GDC infiltration.

Due to their modularity and fuel flexibility, SOFCs have applications outside of being used as a replacement for centralized fossil fuel electricity generation. The products of SOFC operation besides electricity are heat and water. Properly leveraged, these byproducts could allow SOFCs to act as a source of distributed, renewable utilities for communities, especially in developing nations. A method for measuring the thermal energy released by lab-scale SOFCs was developed and used to measure the effect of different fuel compositions and operating currents on heat production. These data were combined with thermal energy production measurements from the operation of a production-scale SOFC to calculate the thermal and electrical performance of a multi-stack SOFC system. The proposed system, centered on a nominal 10 kW SOFC generator, fueled by biogas supplied by anaerobic digesters, and incorporating a direct contact membrane distillation unit, would provide clean water and electricity to over 50 individuals. Recycling of plant, animal, and human waste into useful electricity, heat, and clean water on the local level would significantly raise living standards in many parts of the developing world.

The key accomplishments of this work are: the determination of ideal anode pore geometry and SOFC orientation for maximum mechanical strength; the development and characterization of a simple anode surface treatment for GDC based SOFCs which results in significantly improved resilience to sulfur poisoning of anodes; and

the development and application of a simple technique for measuring thermal power output of SOFCs, allowing for the design of a modular system capable of generating electricity, heat, and clean water.

The knowledge gained from these studies extends the limits of SOFC application as a part of the solution to ever increasing demand for energy, and comprises another step toward the maturity of intermediate-temperature solid oxide fuel cell technology.

Appendices

Appendix A: SEM Fractography of SOFC Coupon Samples

25°C, Air:

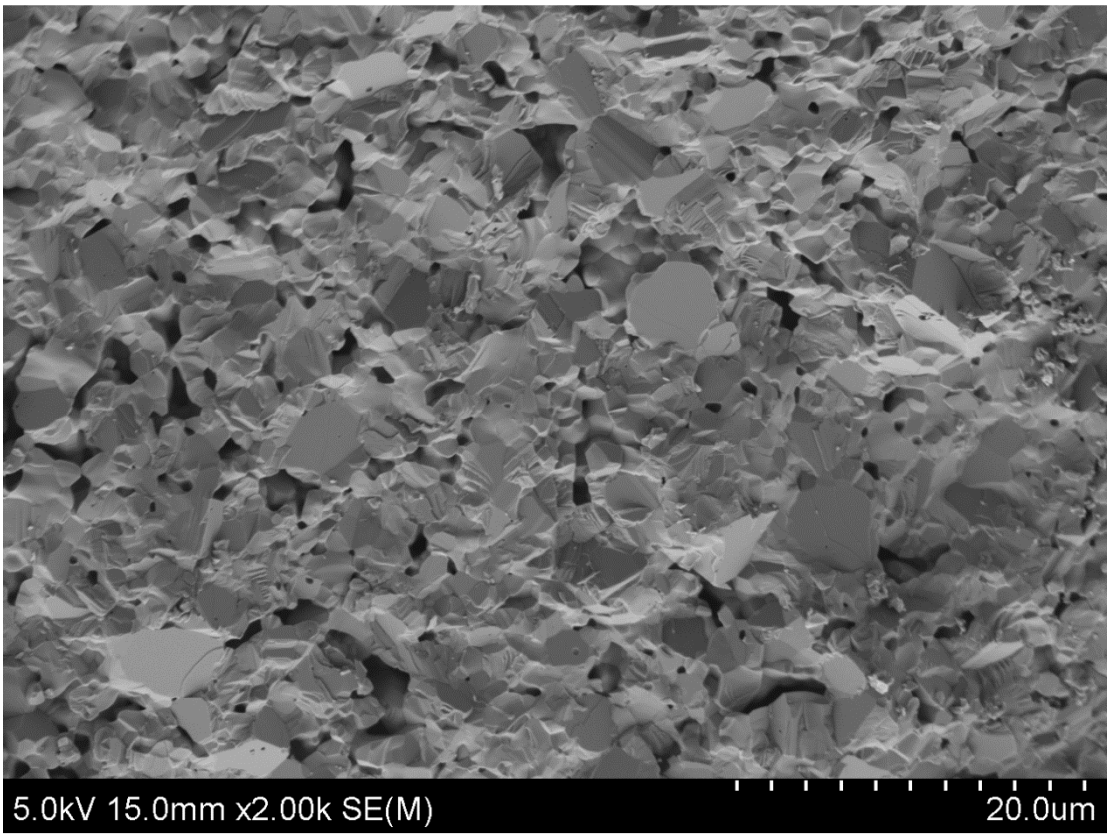

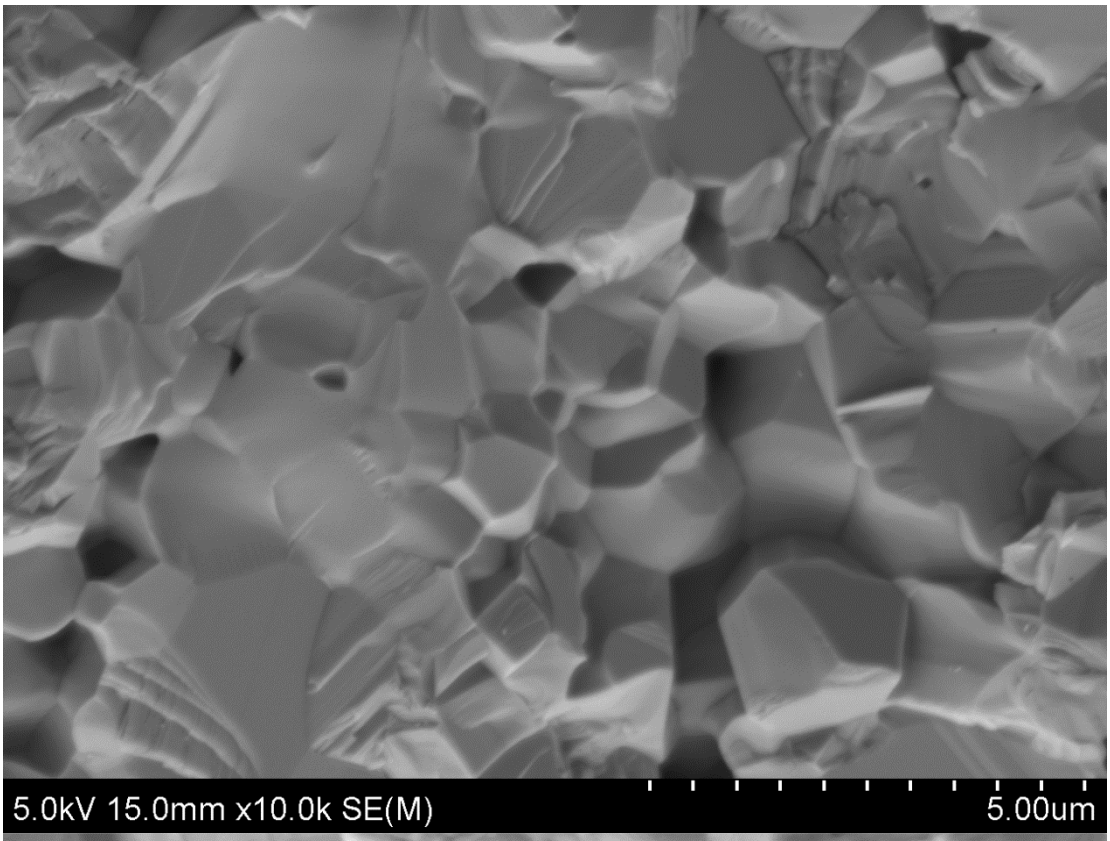
5.0kV 15.0mm x10.0k SE(M)
5.00um

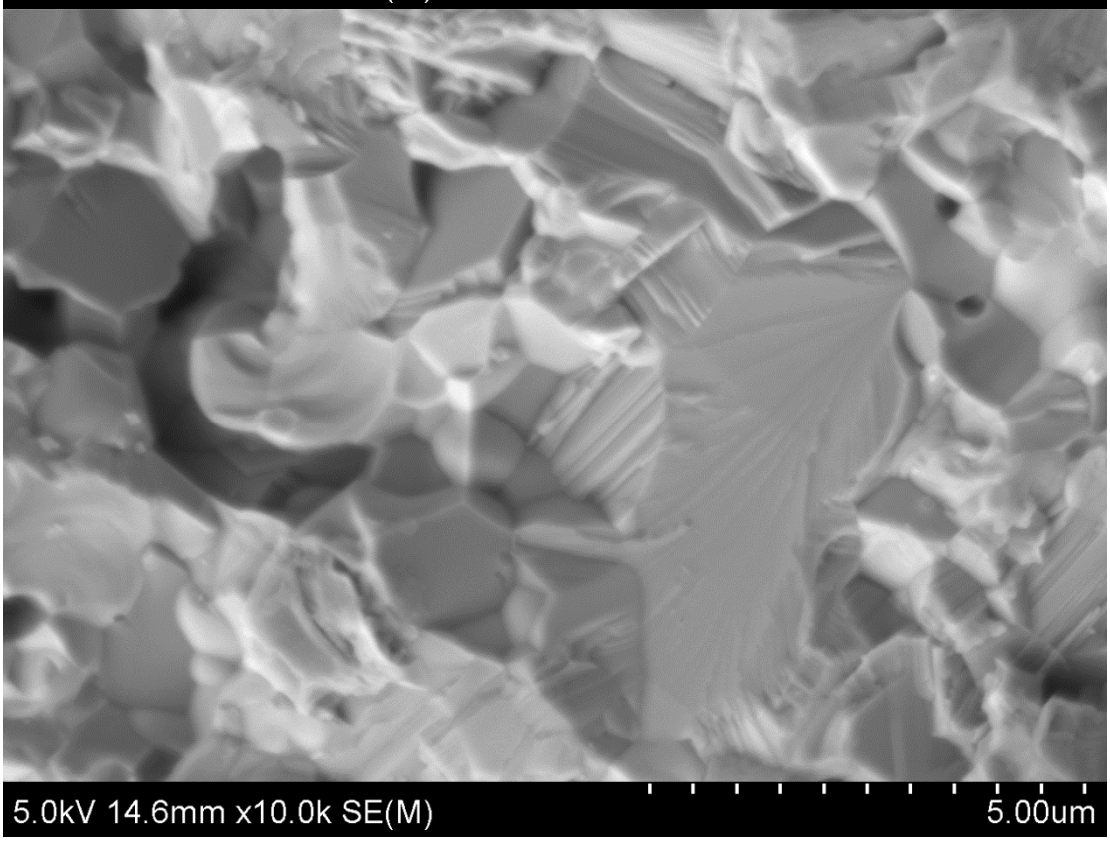
5.0kV 14.6mm x10.0k SE(M)
5.00um

650°C, Air:

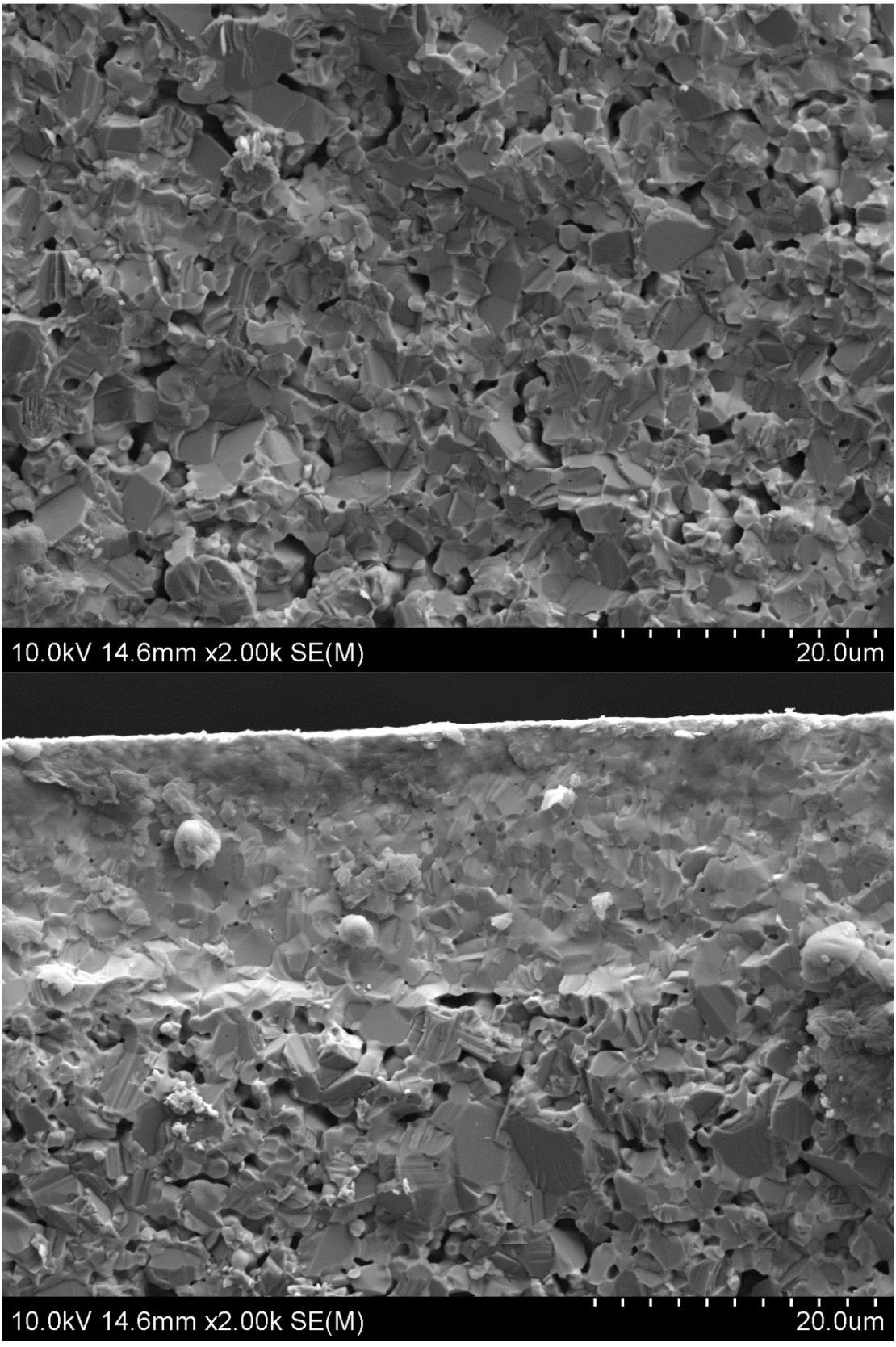

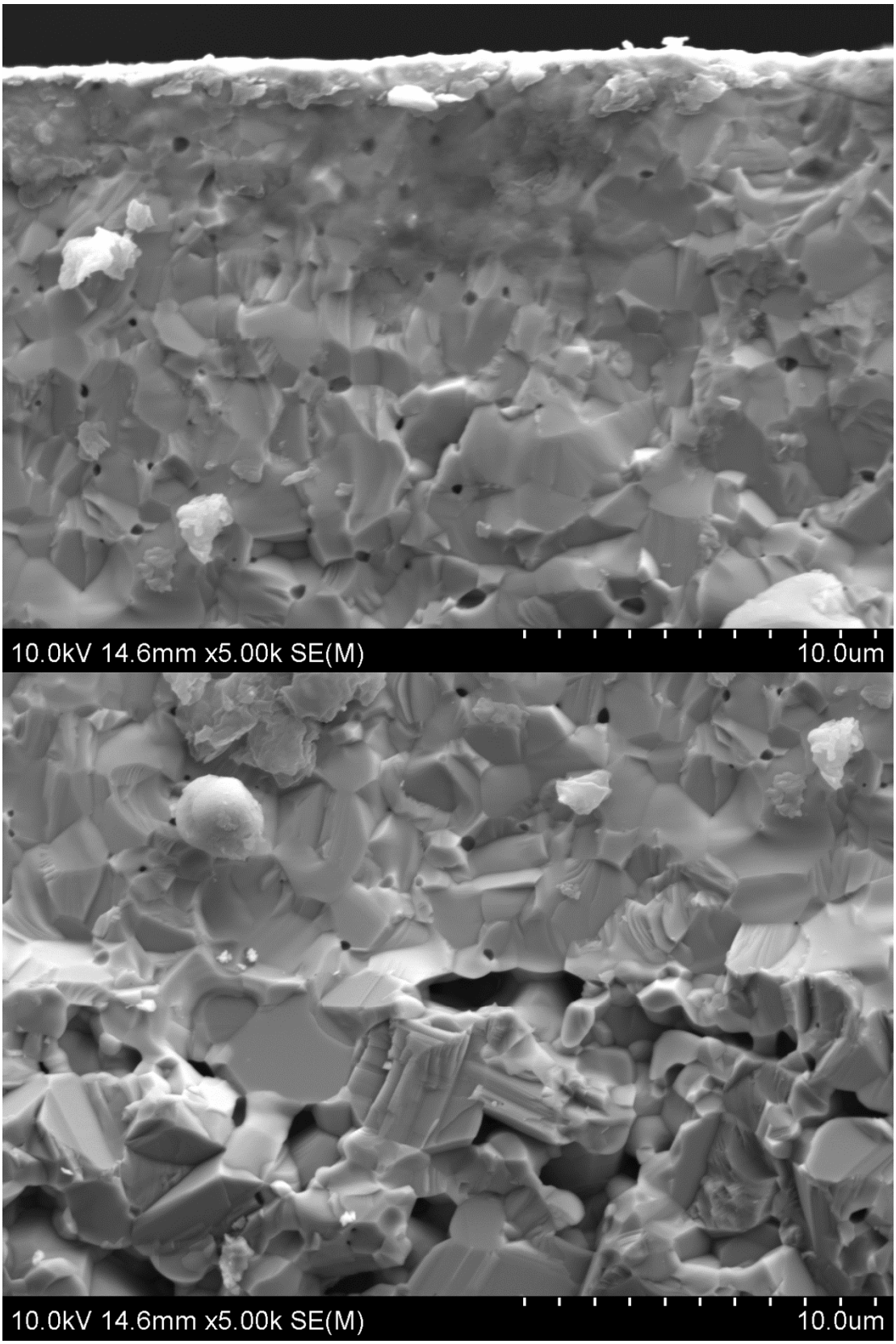
10.0kV 14.6mm x5.00k SE(M)
10.0um
10.0kV 14.6mm x5.00k SE(M)
10.0um

650°C, 5% H_2 95% Ar:

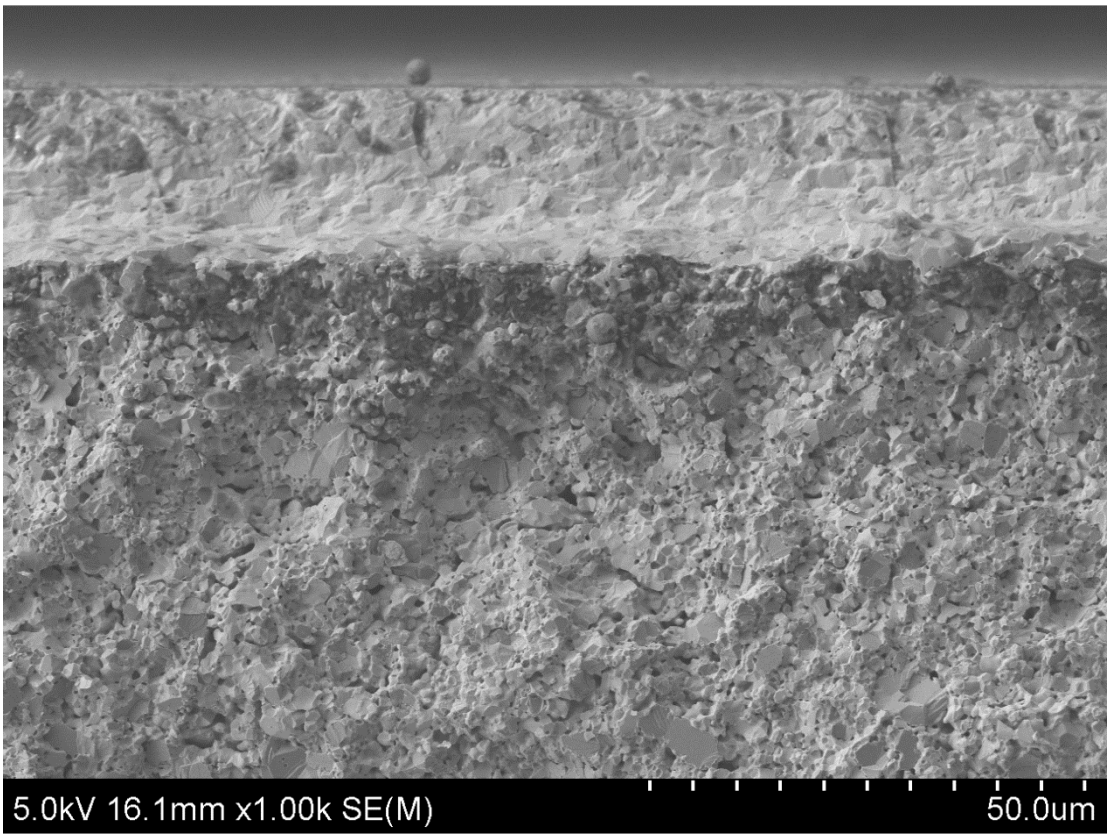

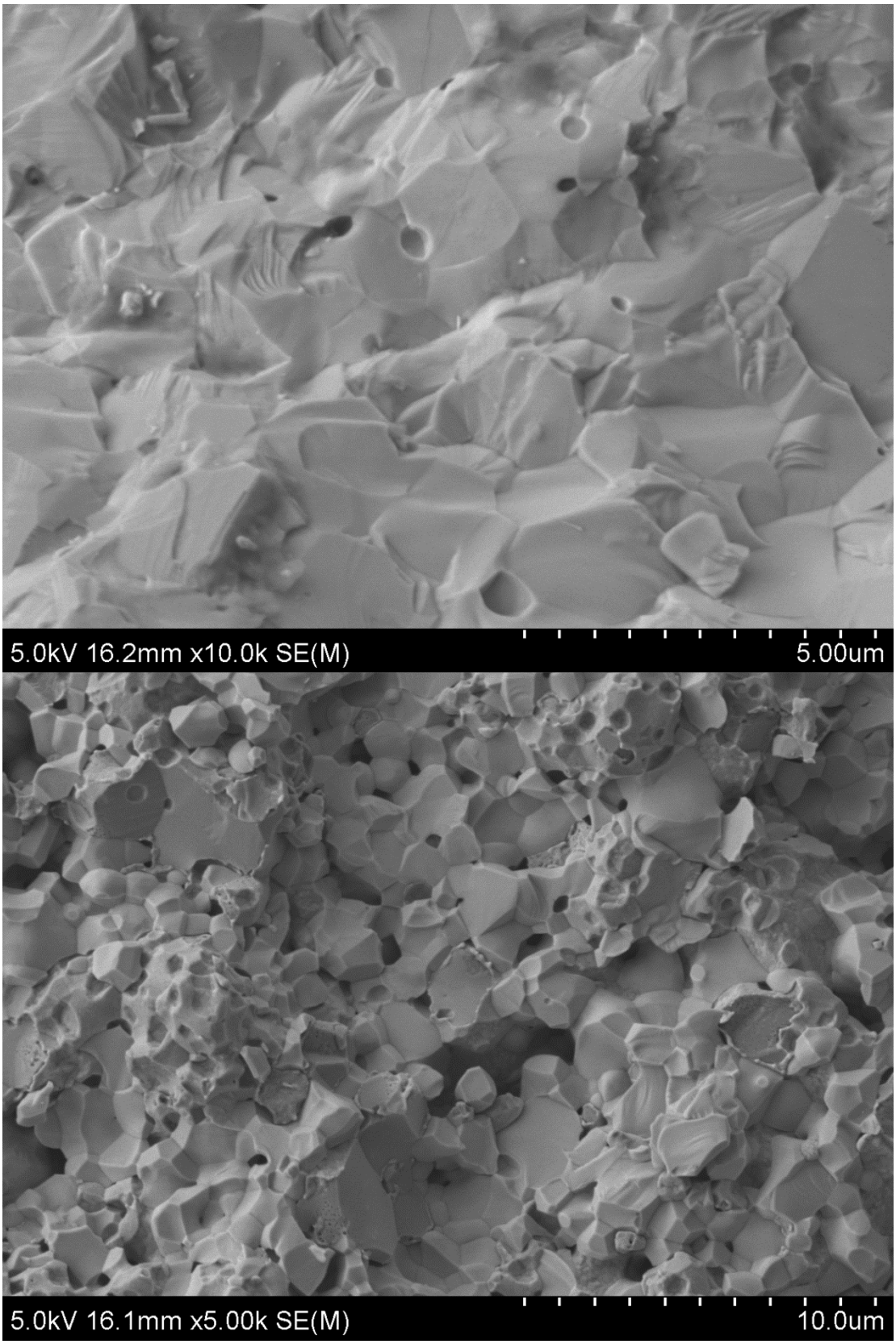
5.0kV 16.2mm x10.0k SE(M)
5.00um
5.0kV 16.1mm x5.00k SE(M)
10.0um

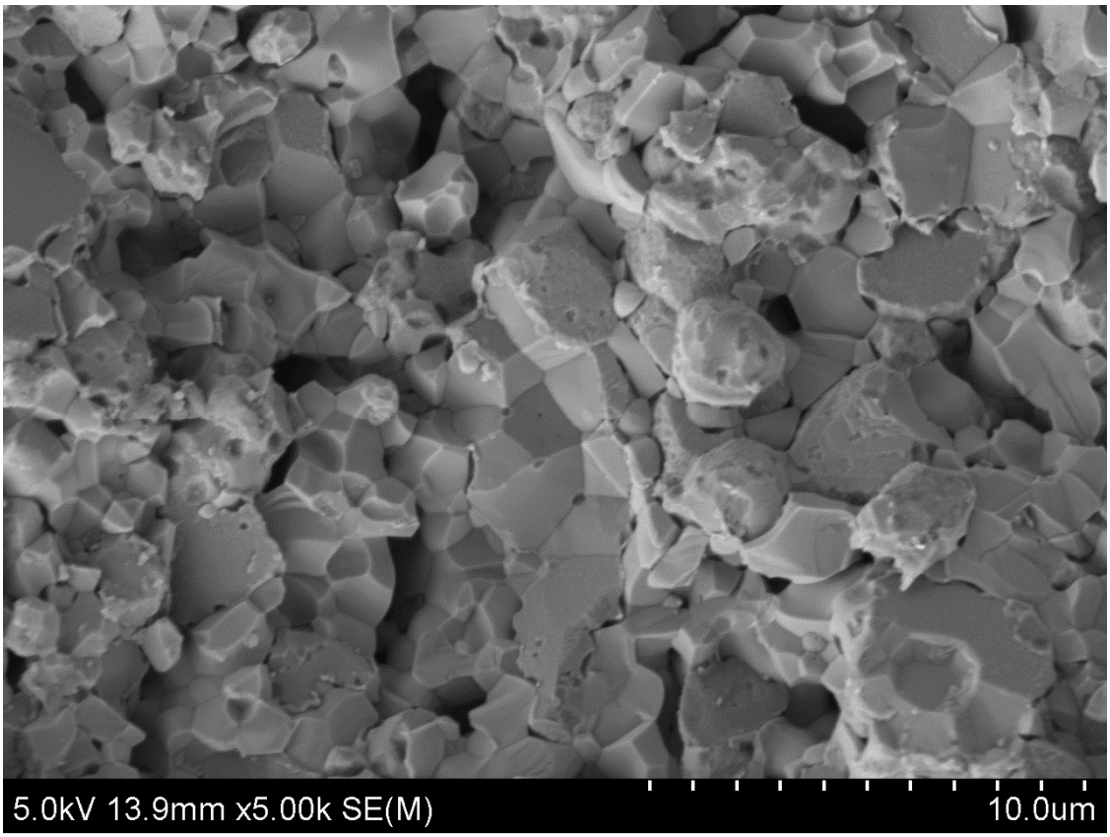
5.0kV 13.9mm x5.00k SE(M)
10.0um

Bibliography

[1] J. A. Kilner and R. J. Brook, “A study of oxygen ion conductivity in doped non-stoichiometric oxides,” *Solid State Ionics*, vol. 6, no. 3, pp. 237–252, 1982.

[2] A. ISENBERG, “Energy conversion via solid oxide electrolyte electrochemical cells at high temperatures,” *Solid State Ionics*, vol. 3–4, pp. 431–437, 1981.

[3] H. S. Isaacs, L. J. Olmer, E. J. L. Schouler, and C. Y. Yang, “Electrode Reactions at Solid Oxide Electrolytes,” *Solid State Ionics*, vol. 3, no. 4, pp. 503–507, 1981.

[4] Y. Ohno, S. Nagata, and H. Sato, “Properties of oxides for high temperature solid electrolyte fuel cell,” *Solid State Ionics*, vol. 9–10, no. PART 2, pp. 1001–1007, 1983.

[5] V. Butler, C. R. A. Catlow, B. E. F. Fender, and J. H. Harding, “Dopant ion radius and ionic conductivity in cerium dioxide,” *Solid State Ionics*, vol. 8, no. 2, pp. 109–113, 1983.

[6] R. Gerhardt-Anderson and A. S. Nowick, “Ionic conductivity of CeO2 with trivalent dopants of different ionic radii,” *Solid State Ionics*, vol. 5, no. C, pp. 547–550, 1981.

[7] I. EG&G Technical Services, “Fuel Cell Handbook,” *Fuel Cell*, vol. 7 Edition, no. November, pp. 1–352, 2004.

[8] M. W. Breiter, “Processes in Fuel Cells with Solid Electrolytes,” in *Electrochemical Processes in Fuel Cells*, 1st ed., no. 1, Springer-Verlag Berlin Heidelberg, 1969, pp. 230–237.

[9] E. M. Brodnikovskii, “Solid Oxide Fuel Cell Anode Materials,” *Powder*

Metall. Met. Ceram., vol. 54, no. 502, pp. 166–174, 2015.

[10] A. Zarkov, A. Stanulis, J. Sakaliuniene, S. Butkute, B. Abakeviciene, T. Salkus, S. Tautkus, A. F. Orliukas, S. Tamulevicius, and A. Kareiva, "On the synthesis of yttria-stabilized zirconia: a comparative study," *J. Sol-Gel Sci. Technol.*, vol. 76, no. 2, pp. 309–319, 2015.

[11] S. Primdahl and M. Mogensen, "Oxidation of Hydrogen on Ni/Yttria-Stabilized Zirconia Cermet Anodes," *J. Electrochem. Soc.*, vol. 144, no. 10, pp. 3409–3419, 1997.

[12] T. H. Etsell and S. N. Flengas, "Electrical properties of solid oxide electrolytes," *Chem. Rev.*, vol. 70, no. 3, pp. 339–376, 1970.

[13] N. Droushiotis, A. Torabi, M. H. D. Othman, T. H. Etsell, and G. H. Kelsall, "Effects of lanthanum strontium cobalt ferrite (LSCF) cathode properties on hollow fibre micro-tubular SOFC performances," *J. Appl. Electrochem.*, vol. 42, no. 7, pp. 517–526, 2012.

[14] M. Liu, D. Ding, K. Blinn, X. Li, L. Nie, and M. Liu, "Enhanced performance of LSCF cathode through surface modification," *Int. J. Hydrogen Energy*, vol. 37, no. 10, pp. 8613–8620, 2012.

[15] N. Jiang and E. D. Wachsman, "Structural Stability and Conductivity of Phase-Stabilized Cubic Bismuth Oxides," *J. Am. Ceram. Soc.*, vol. 82, no. 11, pp. 3057–3064, 1999.

[16] A. L. Ruth, "Solid Oxide Ionic Materials For Electrochemical Energy Conversion And Storage," University of Maryland College Park, 2015.

[17] A. G. Jolley and E. D. Wachsman, "A New Double Doped Bismuth Oxide with

Stable Ionic Conductivity at Intermediate Temperatures," vol. 78, no. 1, pp. 355–360, 2017.

[18] J. Ki and D. Kim, "Computational model to predict thermal dynamics of planar solid oxide fuel cell stack during start-up process," *J. Power Sources*, vol. 195, no. 10, pp. 3186–3200, 2010.

[19] E. Barsoukov and J. R. Macdonald, *Impedance Spectroscopy*, 2nd ed. Hoboken: John Wiley & Sons, Inc., 2005.

[20] O. Wing, "Properties in the Frequency Domain," in *Classical Circuit Theory*, 1st ed., Springer US, 2008, pp. 59–88.

[21] O. Wing, "The Impedance Function," in *Classical Circuit Theory*, 1st ed., Springer US, 2008, pp. 89–98.

[22] Q. A. Huang, R. Hui, B. Wang, and J. Zhang, "A review of AC impedance modeling and validation in SOFC diagnosis," *Electrochim. Acta*, vol. 52, no. 28, pp. 8144–8164, 2007.

[23] S. O. Kasap, "Electrical and Thermal Conduction in Solids," in *Principles of Electronic Materials and Devices*, 3rd ed., New York: McGraw-Hill, 2006, pp. 113–180.

[24] E. D. Wachsman, S. Boyapati, M. J. Kaufman, and N. Jiang, "Modeling of Ordered Structures of Phase-Stabilized Cubic Bismuth Oxides," *J. Am. Ceram. Soc.*, vol. 83, no. 8, pp. 1964–1968, 2000.

[25] H. Schichlein, H. Schichlein, E. Ivers-tiffe, E. Ivers-tiffe, M. Voigts, A. Kru, H. Schichlein, A. C. Mu, A. Müller, and M. Voigts, "Deconvolution of electrochemical impedance spectra for the identification of electrode reaction

mechanisms in solid oxide fuel cells," *J. Appl. ...*, vol. 32, no. 8, pp. 875–882, 2002.

[26] T. Tsai and S. A. Barnett, "Effect of Mixed-Conducting Interfacial Layers on Solid Oxide Fuel Cell Anode Performance," *J. Electrochem. Soc.*, vol. 145, no. 5, pp. 1696–1701, 1998.

[27] N. Wagner, W. Schnurnberger, B. Müller, and M. Lang, "Electrochemical impedance spectra of solid-oxide fuel cells and polymer membrane fuel cells," *Electrochim. Acta*, vol. 43, no. 24, pp. 3785–3793, 1998.

[28] T. H. Courtney, "Fracture Mechanics," in *Mechanical Behavior of Materials*, 2nd ed., Long Grove: Waveland Press, Inc., 2005, pp. 404–448.

[29] D. Taylor, "5. Ceramics: Brittle Fracture in Engineering Ceramics , Building Materials , Geological Materials and Nanomaterials," in *The Theory of Critical Distances A New Perspective in Fracture Mechanics*, Elsevier, 2007, pp. 63–91.

[30] A. A. Griffith, "VI. The Phenomena of Rupture and Flow in Solids," *Philos. Trans. R. Soc. London*, vol. 221, no. 582–593, pp. 163–198, 1921.

[31] Y. Yamade, Y. Kawaguchi, N. Takeda, and T. Kishi, "Effects of defects and grain size on strengthof mullite ceramics," in *Fracture Mechanics of Ceramics*, vol. 10, New York: Springer Science+Business Media New York, 1992, pp. 291–306.

[32] S. E. Gass, M. L. Sandoval, M. H. Talou, A. G. Martinez Tomba, M. A. Camerucci, E. Gregorová, and W. Pabst, "High Temperature Mechanical Behavior of Porous Cordierite-based Ceramic Materials Evaluated Using 3-

point Bending," *Procedia Mater. Sci.*, vol. 9, pp. 254–261, 2015.

[33] R. E. Mistler, "The principles of tape casting and tape casting applications," in *Ceramic Porcessing, edited by R.A. Terpstra*\, 1st ed., Springer-Science+Busniness Media, B.V., 1995, pp. 147–173.

[34] P. S. Turner, "Electron Microscope Techniques for Surface Characterization," in *Surface Analysis Methods in Materials Science*, J. O'Connor, B. Sexton, and R. Smart, Eds. Springer Berlin Heidelberg, 1992, pp. 79–96.

[35] N. Colthup, "1.30 The Raman Effect," in *Introduction to Infrared and Raman Spectroscopy*, 2nd ed., Elsevier Science, 1975, pp. 57–68.

[36] K. Siegbahn, "Photoelectron Spectroscopy : Retrospects and Prospects," *Philos. Trans. R. Soc. London*, vol. 318, no. 1541, pp. 3–36, 1986.

[37] J. J. Roa, M. A. Laguna-Bercero, A. Larrea, V. M. Orera, and M. Segarra, "Mechanical properties of highly textured porous Ni-YSZ and Co-YSZ cermets produced from directionally solidified eutectics," *Ceram. Int.*, vol. 37, no. 8, pp. 3123–3131, 2011.

[38] J. H. Yu, G. W. Park, S. Lee, and S. K. Woo, "Microstructural effects on the electrical and mechanical properties of Ni-YSZ cermet for SOFC anode," *J. Power Sources*, vol. 163, no. 2, pp. 926–932, 2007.

[39] A. Nakajo, J. Kuebler, A. Faes, U. F. Vogt, H. J. Schindler, L. K. Chiang, S. Modena, J. Van Herle, and T. Hocker, "Compilation of mechanical properties for the structural analysis of solid oxide fuel cell stacks. Constitutive materials of anode-supported cells," *Ceram. Int.*, vol. 38, no. 5, pp. 3907–3927, 2012.

[40] Z. Y. Deng, J. She, Y. Inagaki, J. F. Yang, T. Ohji, and Y. Tanaka,

"Reinforcement by crack-tip blunting in porous ceramics," *J. Eur. Ceram. Soc.*, vol. 24, no. 7, pp. 2055–2059, 2004.

[41] M. Ambrozic and T. Kosmac, "Optimization of the bend strength of flat-layered alumina-zirconia composites," *J. Am. Ceram. Soc.*, vol. 90, no. 5, pp. 1545–1550, 2007.

[42] A. Yonezu and X. Chen, "Micro-scale damage characterization in porous ceramics by an acoustic emission technique," *Ceram. Int.*, vol. 40, no. 7 PART A, pp. 9859–9866, 2014.

[43] S. Meille, M. Lombardi, J. Chevalier, and L. Montanaro, "Mechanical properties of porous ceramics in compression: On the transition between elastic, brittle, and cellular behavior," *J. Eur. Ceram. Soc.*, vol. 32, no. 15, pp. 3959–3967, 2012.

[44] P. Nie, H. Lv, T. Zhou, X. Cai, and P. K. Chu, "Interfacial adhesion measurement of a ceramic coating on metal substrate," *J. Coatings Technol. Res.*, vol. 7, no. 3, pp. 391–398, 2010.

[45] C. Olagnon, "Determination of the fracture mechanical parameters of porous ceramics from microstructure parameters measured by quantitative image analysis," *J. Mater. Sci.*, vol. 4, no. 1, pp. 4081–4088, 1999.

[46] B. F. Sorensen and A. Horsewell, "Crack Growth along Interfaces in Porous Ceramic Layers," *J. Am. Ceram. Soc.*, vol. 84, no. 9, pp. 2051–59, 2001.

[47] S. M. Barinov, V. F. Ponomarev, and V. Y. Shevchenko, "Effect of Hot Isostatic Pressing on the Mechanical Properties of Aluminum Oxide Ceramics," pp. 9–12, 1997.

[48] K. Yasuda, K. Uemura, and T. Shiota, “Sintering and mechanical properties of gadolinium-doped ceria ceramics,” *J. Phys. Conf. Ser.*, vol. 339, no. 1, p. 12006, 2012.

[49] R. W. Rice, *Porosity of Ceramics: Properties and Applications*, Illustrate. New York: Marcel Dekker. Inc., 1998.

[50] O. Ševeček, M. Kotoul, D. Leguillon, E. Martin, and R. Bermejo, “Assessment of crack-related problems in layered ceramics using the finite fracture mechanics and coupled stress-energy criterion,” *Procedia Struct. Integr.*, vol. 2, pp. 2014–2021, 2016.

[51] M. F. Fellah, “Adsorption of hydrogen sulfide as initial step of H2S removal: A DFT study on metal exchanged ZSM-12 clusters,” *Fuel Process. Technol.*, vol. 144, pp. 191–196, 2016.

[52] K. Sasaki, K. Susuki, a. Iyoshi, M. Uchimura, N. Imamura, H. Kusaba, Y. Teraoka, H. Fuchino, K. Tsujimoto, Y. Uchida, and N. Jingo, “H[sub 2]S Poisoning of Solid Oxide Fuel Cells,” *J. Electrochem. Soc.*, vol. 153, no. 11, p. A2023, 2006.

[53] A. Weber, S. Dierickx, N. Russner, and E. Ivers-tiffée, “Sulfur Poisoning of Ni-Based SOFC-Anodes – Short and Long Term Behavior,” *ECS Trans.*, vol. 77, no. 10, pp. 141–147, 2017.

[54] G. J. Offer, J. Mermelstein, E. Brightman, and N. P. Brandon, “Thermodynamics and kinetics of the interaction of carbon and sulfur with solid oxide fuel cell anodes,” *J. Am. Ceram. Soc.*, vol. 92, no. 4, pp. 763–780, 2009.

[55] Z. Cheng, S. Zha, and M. Liu, “Influence of cell voltage and current on sulfur poisoning behavior of solid oxide fuel cells,” *J. Power Sources*, vol. 172, no. 2, pp. 688–693, Oct. 2007.

[56] E. Brightman, D. G. Ivey, D. J. L. Brett, and N. P. Brandon, “The effect of current density on H2S-poisoning of nickel-based solid oxide fuel cell anodes,” *J. Power Sources*, vol. 196, no. 17, pp. 7182–7187, Sep. 2011.

[57] L. L. Zheng, X. Wang, L. Zhang, J.-Y. Wang, and S. P. Jiang, “Effect of Pd-impregnation on performance, sulfur poisoning and tolerance of Ni/GDC anode of solid oxide fuel cells,” *Int. J. Hydrogen Energy*, vol. 37, no. 13, pp. 10299–10310, Jul. 2012.

[58] L. Zhang, S. P. Jiang, H. Q. He, X. Chen, J. Ma, and X. C. Song, “A comparative study of H2S poisoning on electrode behavior of Ni/YSZ and Ni/GDC anodes of solid oxide fuel cells,” *Int. J. Hydrogen Energy*, vol. 35, no. 22, pp. 12359–12368, Nov. 2010.

[59] M. Gong, X. Liu, J. Trembly, and C. Johnson, “Sulfur-tolerant anode materials for solid oxide fuel cell application,” *J. Power Sources*, vol. 168, no. 2, pp. 289–298, Jun. 2007.

[60] E. C. S. Transactions and T. E. Society, “Assessment of Sulfur Poisoning of Ni/CGO-Based SOFC Anodes,” vol. 77, no. 10, pp. 149–156, 2017.

[61] J. W. Yun, S. P. Yoon, J. Han, S. Park, H. S. Kim, and S. W. Nam, “Ceria Coatings Effect on H[sub 2]S Poisoning of Ni/YSZ Anodes for Solid Oxide Fuel Cells,” *J. Electrochem. Soc.*, vol. 157, no. 12, p. B1825, 2010.

[62] A. Mohammed Hussain, J. V. T. Høgh, T. Jacobsen, and N. Bonanos, “Nickel-

ceria infiltrated Nb-doped SrTiO3 for low temperature SOFC anodes and analysis on gas diffusion impedance," *Int. J. Hydrogen Energy*, vol. 37, no. 5, pp. 4309–4318, 2012.

[63] A. M. Hussain, J. V. T. Hogh, W. Zhang, and N. Bonanos, "Efficient ceramic anodes infiltrated with binary and ternary electrocatalysts for SOFCs operating at low temperatures," *J. Power Sources*, vol. 216, pp. 308–313, 2012.

[64] A. M. Hussain, J. V. T. Høgh, W. Zhang, P. Blennow, N. Bonanos, and B. A. Boukamp, "Effective improvement of interface modified strontium titanate based solid oxide fuel cell anodes by infiltration with nano-sized palladium and gadolinium-doped cerium oxide," *Electrochim. Acta*, vol. 113, pp. 635–643, 2013.

[65] C. H. Bartholomew, "Mechanisms of catalyst deactivation," *Appl. Catal. A Gen.*, vol. 212, no. 1–2, pp. 17–60, Apr. 2001.

[66] B. Mirfakhraei, S. Paulson, V. Thangadurai, and V. Birss, "Enhanced hydrogen oxidation activity and H2S tolerance of Ni-infiltrated ceria solid oxide fuel cell anodes," *J. Power Sources*, vol. 243, pp. 95–101, 2013.

[67] H. Yokokawa, H. Tu, B. Iwanschitz, and A. Mai, "Fundamental mechanisms limiting solid oxide fuel cell durability," *J. Power Sources*, vol. 182, no. 2, pp. 400–412, 2008.

[68] H. C. Choi, Y. M. Jung, and S. Bin Kim, "Size effects in the Raman spectra of TiO2 nanoparticles," *Vib. Spectrosc.*, vol. 37, no. 1, pp. 33–38, 2005.

[69] X. Li, M. Liu, J. Lee, D. Ding, L. A. Bottomley, S. Park, and M. Liu, "An operando surface enhanced Raman spectroscopy (SERS) study of carbon

deposition on SOFC anodes.," *Phys. Chem. Chem. Phys.*, vol. 17, no. 33, pp. 21112–9, 2015.

[70] J. Hodkiewicz and T. F. Scientific, "Characterizing Carbon Materials with Raman Spectroscopy," *Prog. Mater. Sci.*, vol. 50, pp. 929–961, 2005.

[71] S. M. Bose, S. Gayen, and S. N. Behera, "Theory of the tangential G-band feature in the Raman spectra of metallic carbon nanotubes," *Phys. Rev. B - Condens. Matter Mater. Phys.*, vol. 72, no. 15, 2005.

[72] L. Truffault, M. T. Ta, T. Devers, K. Konstantinov, V. Harel, C. Simmonard, C. Andreazza, I. P. Nevirkovets, A. Pineau, O. Veron, and J. P. Blondeau, "Application of nanostructured Ca doped CeO2 for ultraviolet filtration," *Mater. Res. Bull.*, vol. 45, no. 5, pp. 527–535, 2010.

[73] UNICEF and WHO, "A Snapshot of Drinking Water and Sanitation in Africa: A regional perspective based on new data from the WHO/UNICEF Joint Monitoring Programme for Water Supply and Sanitation ," *Prep. AMCOM as a Contrib. to 11th Summit Heads State Gov. African Union With Spec. theme Meet. Millenn. Dev. Goal Water Sanit. 30 June to 1 July, 2008*, 2008.

[74] UN-Water, "Water for a sustainable world," 2015.

[75] J. A. Fonseca and A. Schlueter, "Novel approach for decentralized energy supply and energy storage of tall buildings in Latin America based on renewable energy sources: Case study - Informal vertical community Torre David, Caracas - Venezuela," *Energy*, vol. 53, pp. 93–105, 2013.

[76] N. M. Katsoulakos and D. C. Kaliampakos, "Mountainous areas and decentralized energy planning: Insights from Greece," *Energy Policy*, vol. 91,

pp. 174–188, 2016.

[77] P. Alstone, D. Gershenson, and D. M. Kammen, “Decentralized energy systems for clean electricity access,” *Nat. Clim. Chang.*, vol. 5, no. 2002, pp. 305–314, 2015.

[78] D. Silva Herran and T. Nakata, “Design of decentralized energy systems for rural electrification in developing countries considering regional disparity,” *Appl. Energy*, vol. 91, no. 1, pp. 130–145, 2012.

[79] K. T. Lee and E. D. Wachsman, “Role of nanostructures on SOFC performance at reduced temperatures,” *MRS Bull.*, vol. 39, no. 9, pp. 783–791, 2014.

[80] M. Liu, M. E. Lynch, K. Blinn, F. M. Alamgir, and Y. Choi, “Rational SOFC material design: New advances and tools,” *Mater. Today*, vol. 14, no. 11, pp. 534–546, 2011.

[81] J. M. Beér, “High efficiency electric power generation: The environmental role,” *Prog. Energy Combust. Sci.*, vol. 33, no. 2, pp. 107–134, 2007.

[82] C. Spieker, C. Spitta, M. Noponen, P. Hallanoro, and T. Ruetten, “High Efficient Combined Heat and Power SOFC System for Residential Power Applications: Lifetime-Efficiency-Simulations Using AspenPlusTM,” *ECS Trans.* , vol. 68, no. 1, pp. 3115–3132, 2015.

[83] W. B. Guan, H. J. Zhai, L. Jin, C. Xu, and W. G. Wang, “Temperature measurement and distribution inside planar SOFC stacks,” *Fuel Cells*, vol. 12, no. 1, pp. 24–31, 2012.

[84] S. Celik, B. Timurkutluk, and M. D. Mat, “Measurement of the temperature

distribution in a large solid oxide fuel cell short stack," *Int. J. Hydrogen Energy*, vol. 38, no. 25, pp. 10534–10541, 2013.

[85] O. Razbani, I. Wærnhus, and M. Assadi, "Experimental investigation of temperature distribution over a planar solid oxide fuel cell," *Appl. Energy*, vol. 105, pp. 155–160, 2013.

[86] A. Boubakri, A. Hafiane, and S. A. T. Bouguecha, "Direct contact membrane distillation: Capability to desalt raw water," *Arab. J. Chem.*, 2014.

[87] F. He, J. Gilron, and K. K. Sirkar, "High water recovery in direct contact membrane distillation using a series of cascades," *Desalination*, vol. 323, pp. 48–54, 2013.

[88] Z. Li, Y. Peng, Y. Dong, H. Fan, P. Chen, L. Qiu, and Q. Jiang, "Effects of thermal efficiency in DCMD and the preparation of membranes with low thermal conductivity," *Appl. Surf. Sci.*, vol. 317, pp. 338–349, 2014.

[89] D. Singh and K. K. Sirkar, "Desalination of brine and produced water by direct contact membrane distillation at high temperatures and pressures," *J. Memb. Sci.*, vol. 389, pp. 380–388, 2012.

[90] Q. Wang, L. Li, and C. Wang, "Numerical study of thermoelectric characteristics of a planar solid oxide fuel cell with direct internal reforming of methane," *J. Power Sources*, vol. 186, no. 2, pp. 399–407, 2009.

[91] D. Spuhler, "Anaerobic Digestion (Small-scale)," 2016. [Online]. Available: http://www.sswm.info/content/anaerobic-digestion-small-scale. [Accessed: 11-Jan-2016].

[92] IEA, "Africa Energy Outlook: A Focus on Prospects in Sub-Saharan Africa,"

pp. 1–242, 2014.